Fakultät für Physik der Technischen Universität München
Lehrstuhl E15, Univ.-Prof. Dr. F. von Feilitzsch
Institut für Astro-Teilchen-Physik

Development of a Liquid Scintillator and of Data Analysis Methods for BOREXINO

Marianne Göger-Neff

Vollständiger Abdruck der von der Fakultät für Physik der Technischen Universität München zur Erlangung des akademischen Grades eines

Doktors der Naturwissenschaften

genehmigten Dissertation.

Vorsitzender :		Univ.-Prof. Dr. M. Lindner
Prüfer der Dissertation :	1.	Univ.-Prof. Dr. F. von Feilitzsch
	2.	Apl. Prof. Dr. V. Schönfelder
	3.	Univ.-Prof. Dr. H.-J. Körner (schriftliche Beurteilung)

Die Dissertation wurde am 20. August 2001 bei der Technischen Universität München eingereicht und durch die Fakultät für Physik am 23. Oktober 2001 angenommen.

Abstract

The solar neutrino problem has been one of the most intriguing questions in astrophysics and particle physics over the last 30 years. The first motivation for a solar neutrino experiment was the possibility to use the neutrinos "to see into the interior of a star and thus verify directly the hypothesis of nuclear energy generation in stars" [Bah64]. The evidence for solar neutrinos in the first detector, the Homestake experiment, showed that the sun indeed produces a large fraction of its energy by nuclear fusion reactions. However, the first generation of solar neutrino experiments (Homestake, Kamiokande, GALLEX, SAGE) all measured a substantially lower neutrino flux than predicted by the standard solar model. Even more puzzling, the suppression factors in the four detectors are different and not explainable by modifications of the theoretical solar models, like nuclear reaction rates or the equation of state. The standard solar model, on the other hand, has been confirmed by helioseismological measurements. Thus, the success of the neutrino experiments in confirming stellar evolution theory by the detection of neutrinos became a challenge for physicists to explain the discrepancy between the measured and predicted neutrino flux.

The only convincing solution to the solar neutrino problem is flavour transitions between the different lepton families (e, μ, τ), which can occur only if the neutrinos have a non-zero rest mass, and the eigenstates of the weak interaction are not equal to the mass eigenstates. This would imply that the standard model of electroweak interactions has to be modified as, in this theory, the neutrinos are assumed to be massless a priori. The first evidence for neutrino oscillations ($\nu_\mu \leftrightarrow \nu_\tau$), and thus for physics beyond the standard model, was announced in 1998 by the Super-Kamiokande experiment measuring atmospheric neutrinos [Fuk98].

The main focus of the second generation solar neutrino experiments (Super-Kamiokande, GNO, SNO, BOREXINO) is now to confirm the evidence for neutrino oscillations and to pinpoint the mass and mixing parameters down to one of the currently allowed oscillation scenarios. BOREXINO can play an important role in increasing our understanding of the solar neutrino problem because of its ability to measure the low energy solar ^{7}Be neutrinos in real-time at a high rate. The measurement of the total flux and the time variability of the ^{7}Be signal will allow one to distinguish between all of the currently allowed oscillation scenarios. The direct detection of the ^{7}Be neutrinos is therefore considered as the missing clue for the solution of the solar neutrino problem.

The work described in this thesis was performed in the context of the BOREXINO experiment. The main emphasis was on the development of new methods for the position reconstruction of scintillation events and for particle identification, which are important for an effective background reduction, and on the characterization of a new scintillator mixture based on phenyl-o-xyxlylethane (PXE) that, due to its optical properties and its radiopurity, could be employed in BOREXINO as well as in other large-volume, low-background scintillation detectors.

The first chapter contains a short overview of the theory of solar neutrinos, their production inside the sun and their detection with present and future experiments. The implications of the discrepancy between the predicted and the measured count rates that all experiments to date have seen is discussed, followed by a presentation of the different possible solutions to the solar neutrino problem. The most likely solution, neutrino oscillations, will be discussed in detail.

The second chapter introduces the physics goals of the BOREXINO experiment. The design of the detector and its ancillary systems are described. The different types of background are discussed and the importance of their effective suppression is underlined. In chapter 3 the design and results from the first data taking period of the Counting Test Facility (CTF) are presented, and the main design improvements of the upgraded CTF2 are shortly discussed.

In chapter 4 a newly developed reconstruction method for scintillation events for both BOREXINO and the CTF is presented. This method is based on a comparison of each real event with simulated events from known positions, and includes a model that describes the generation and propagation of the scintillation photons in the detector. Promising results are obtained with Monte Carlo simulations and confirmed by the analysis of real data from the CTF.

Chapter 5 discusses the scintillation processes which allow particle identification, and the application of neural networks to this problem. Results obtained with Monte Carlo simulations and CTF data show the capabilities of this method.

Chapter 6 is devoted to the development of an alternative liquid scintillator for the BOREXINO experiment, namely PXE. This scintillator offers the advantage of a higher density (and therefore higher target mass) compared to the solution chosen for BOREXINO (pseudocumene based scintillator). The results of several tests and measurements in laboratory and in the CTF are presented. The optical properties (light yield, fluorescence time, absorption and reemission), which are essential for position reconstruction and α/β-discrimination, are comparable to those of pseudocumene. The radiopurity level obtained with a newly adopted purification method using a silica gel column was for ^{238}U and ^{232}Th below the sensitivity limit of the neutron activation analysis. Due to background problems, however, it was not possible to confirm these results by the measurements in the CTF.

The last chapter describes the calibration measurements in the CTF2 that I performed. With these measurements the position- and energy-dependent detector response could be tested. The spatial and energy resolution were determined as a function of position and energy, and systematic effects due to the position reconstruction could be excluded.

Übersicht

Das solare Neutrinoproblem ist seit mehr als 30 Jahren eine der faszinierendsten Fragen der Astro- und der Elementarteilchenphysik. Die erste Motivation für ein solares Neutrino-Experiment war die Möglichkeit, Neutrinos dazu zu benutzen, um “in das Innere eines Sterns zu schauen und auf diesem Weg die Hypothese der Energieerzeugung durch Kernfusion in Sternen zu verifizieren” [Bah64]. Der Nachweis solarer Neutrinos mit dem ersten Detektor, dem Homestake-Experiment, zeigte, dass die Sonne tatsächlich einen großen Teil ihrer Energie aus Fusionsreaktionen gewinnt. Allerdings ergaben die Messungen der Experimente der ersten Generation (Homestake, Kamiokande, GALLEX, SAGE) einen deutlich geringeren Neutrinofluss als vom Standardsonnenmodell vorhergesagt wurde. Noch verblüffender ist die Tatsache, dass die Unterdrückungsfaktoren für die verschiedenen Experimente unterschiedlich sind und nicht durch Änderungen der theoretischen Sonnenmodelle, z. B. der Fusionswirkungsquerschnitte oder der Zustandsgleichung, erklärt werden können, zumal andererseits das Standardsonnenmodell in den letzten Jahren durch helioseismologische Messungen hervorragend bestätigt wurde. Auf diese Weise wurde aus dem erfolgreichen Nachweis solarer Neutrinos, um die Theorie der Sternentwicklung zu bestätigen, eine Herausforderung für die Physiker, die Diskrepanz zwischen vorhergesagten und gemessenen Neutrinoflüssen zu erklären.

Die einzige überzeugende Lösung des solaren Neutrinoproblems stellen Übergänge zwischen Neutrinos der verschiedenen Leptonfamilien dar (e, μ, τ), die allerdings nur dann auftreten können, wenn die Neutrinos eine von Null verschiedene Ruhemasse besitzen und die Eigenzustände der schwachen Wechselwirkung nicht identisch mit den Masseeigenzuständen sind. Dies würde bedeuten, dass das Standardmodell der elektroschwachen Wechselwirkung modifiziert werden muss, da in diesem Modell die Neutrinos a priori als masselos angenommen werden. Eine erste Evidenz für Neutrinooszillationen ($\nu_\mu \leftrightarrow \nu_\tau$), und damit Physik jenseits des Standardmodells, ist 1998 von dem Super-Kamiokande-Experiment bei atmosphärischen Neutrinos beobachtet worden [Fuk98].

Das Ziel der zweiten Generation solarer Neutrinoexperimente (Super-Kamiokande, GNO, SNO, BOREXINO) ist es, diese Evidenz für Neutrinooszillationen zu bestätigen und die Massen- und Mischungsparameter auf eine der derzeit erlaubten Kombinationen einzugrenzen. BOREXINO kann dabei eine wichtige Rolle spielen, da es in der Lage sein wird, die niederenergetischen ^{7}Be Neutrinos in Echtzeit und mit hoher Statistik nachzuweisen. Die Messung des gesamten ^{7}Be Neutrinoflusses und seiner Zeitabhängigkeit wird eine Unterscheidung zwischen allen derzeit erlaubten Oszillationslösungen erlauben. Der direkte Nachweis der ^{7}Be Neutrinos wird daher als der fehlende Schlüssel zur Lösung des solaren Neutrinoproblems angesehen.

Die vorliegende Arbeit wurde im Rahmen des BOREXINO-Experiments durchgeführt. Der Schwerpunkt lag dabei in der Entwickung neuer Methoden für die Ortsrekonstruktion von Szintillationsereignissen und für die Teilchenidentifikation, die für eine wirkungsvolle Untergrundsunterdrückung von Bedeutung sind, sowie in der Charakterisierung eines neuen Flüssigszintillators, PXE, der aufgrund seiner optischen Eigenschaften und seiner Reinheit

an Radionukliden in BOREXINO sowie in anderen großvolumigen untergrundarmen Szintillationsdetektoren eingesetzt werden könnte.

Kapitel 1 enthält einen kurzen Überblick über die Theorie der solaren Neutrinos, ihre Erzeugung im Inneren der Sonne und ihren Nachweis mit bestehenden und zukünftigen Experimenten. Die Folgerungen, die sich aus der Diskrepanz zwischen vorhergesagten und gemessenen Ereignisraten ergeben, werden diskutiert und verschiedene Lösungsmöglichkeiten vorgestellt. Neutrinooszillationen als die wahrscheinlicheste Lösung werden im Detail behandelt.

Im zweiten Kapitel wird die physikalische Zielsetzung des BOREXINO-Experiments vorgestellt und das Nachweisprinzip sowie der Aufbau des Detektors beschrieben. Die verschiedenen Klassen von Untergrundereignissen werden diskutiert und Möglichkeiten zu ihrer effektiven Unterdrückung aufgezeigt. Im dritten Kapitel werden der Aufbau und Resultate der ersten Messperiode des Prototypdetektors CTF vorgestellt, und die wichtigsten Änderungen der verbesserten Version CTF2 beschrieben.

In Kapitel 4 wird eine völlig neu entwickelte Methode zur Ortsrekonstruktion von Szintillationsereignissen in BOREXINO und der CTF beschrieben. Diese Methode basiert auf dem Vergleich von gemessenen Ereignissen mit simulierten Ereignissen, die an bekannten Positionen stattfanden. Als wichtiger Bestandteil wurde ein Modell entwickelt, das die Erzeugung und Ausbreitung des Szintillationslichts im Detektor beschreibt. Mit Monte-Carlo-Simulationen wurden mit dieser neuen Methode vielversprechende Ergebnisse erzielt, die bei der Analyse von in der CTF gemessenen Daten bestätigt werden konnten.

Kapitel 5 erläutert im Detail die Prozesse bei der Entstehung des Szintillationslichts, die für die Teilchenidentifikation ausgenützt werden können, sowie die Anwendung künstlicher neuronaler Netze auf dieses Problem. Ergebnisse, die mit Monte-Carlo-Simulationen sowie CTF-Daten erzielt wurden, zeigen das Potential dieser Methode.

Kapitel 6 ist der Entwicklung eines neuen Flüssigszintillators für BOREXINO, PXE, gewidmet. Dieser Szintillator hätte gegenüber dem für BOREXINO gewählten PC den Vorteil einer höheren Dichte (und daher größeren Nachweiseffizienz). Die Ergebnisse verschiedener Messungen, die im Labor oder in der CTF durchgeführt wurden, werden vorgestellt. Die optischen Eigenschaften von PXE (Lichtausbeute, Fluoreszenz-Zeit, Absorption und Reemission), die für die Ortrekonstruktion und α/β Diskrimination von Bedeutung sind, sind mit jenen von PC vergleichbar. Für die Reinigung des Szintillators wurde eine neue Methode getestet, die Säulenreinigung mit Silicagel. Die damit erzielten Reinheitsgrade lagen für ^{238}U und ^{232}Th unter der Nachweisgrenze der in Garching entwickelten Neutronenaktivierungsanalyse. Aufgrund von Untergrundproblemen bestand allerdings keine Möglichkeit, diese Ergebnisse in den CTF-Messungen zu bestätigen.

Das letzte Kapitel beschäftigt sich mit den Eichmessungen, die ich in der CTF2 durchgeführt habe. Mit diesen Messungen wurde die Orts- und Energieabhängigkeit des Detektors getestet. Die Energie- und Ortsauflösung des Rekonstruktionsprogramms konnten in Abhängigkeit von Ort und Energie bestimmt und somit systematische Effekte der Ortsrekonstruktion ausgeschlossen werden.

Contents

1 Solar Neutrinos **1**

1.1 The Standard Solar Model 1

1.2 Detection of Solar Neutrinos 4

1.2.1 Detection Techniques 4

1.2.2 Results from Solar Neutrino Experiments 5

1.2.3 Future Experiments 8

1.3 The Solar Neutrino Puzzle 9

1.3.1 Implications from the Experimental Results 9

1.3.2 Astrophysical Solutions 10

1.3.3 Nuclear Physics Solutions 11

1.3.4 Neutrino Oscillations 11

2 The Borexino Experiment **17**

2.1 Physics Goals 17

2.2 The Detection Principle 22

2.3 Detector Design 24

2.3.1 The Main Detector 24

2.3.2 Ancillary Systems 26

2.4 Background 30

2.4.1 Internal Background 30

2.4.2 External Background 32

2.4.3 Background from Cosmic Ray Events 34

3 The Counting Test Facility (CTF) of Borexino 36

3.1 Motivation . . . 36
3.2 Detector Design . . . 37
3.3 Results from the CTF1 . . . 39
3.4 The upgraded Counting Test Facility: CTF2 . . . 41
3.4.1 Motivation . . . 41
3.4.2 Design Improvements . . . 41

4 Position Reconstruction of Scintillation Events 46

4.1 Basic Idea . . . 46
4.2 The Tracking of the Scintillation Photons . . . 47
4.3 The Reconstruction Program . . . 54
4.4 Results Obtained with Simulated Data . . . 58

5 Particle Identification with a Neural Network 61

5.1 Pulse Shape Discrimination in Liquid Scintillator . . . 61
5.1.1 The Scintillation Process . . . 61
5.1.2 Response to Different Radiations . . . 62
5.1.3 Pulse-Shape-Discrimination . . . 64
5.1.4 The Flash-ADC . . . 64
5.2 Artificial Neural Networks . . . 66
5.3 Results . . . 68
5.3.1 Simulated Data . . . 68
5.3.2 Data from CTF2 . . . 72

6 Test of a PXE based scintillator for Borexino 76

6.1 Motivation for an alternative scintillator . . . 76
6.2 Laboratory Measurements with PXE . . . 77
6.2.1 Basic properties of PXE . . . 77
6.2.2 Optical Properties . . . 79
6.2.3 Radiopurity . . . 80

6.3 The PXE Tests in the CTF 82
6.3.1 The liquid handling system Module-0 and the column plant 82
6.3.2 PXE Test in the CTF1 1996 - 1997 84
6.3.3 The PXE Test in the CTF2 2000 85
6.3.4 Results concerning the Radiopurity 87
6.3.5 Optical Properties 93

7 The Source Runs in CTF2 97
7.1 Motivation 97
7.2 Production of the Sources 97
7.3 The Source Runs 100
7.4 Analysis of the Source Runs 104
7.4.1 Event Selection 104
7.4.2 Reconstructed Source Positions 106
7.4.3 Energy Dependence of the Spatial Resolution 108
7.4.4 Energy Resolution 109
7.4.5 Homogeneity of the Detector Response 110
7.4.6 Time Response 111

Summary and Outlook 113

Bibliography 116

Abbreviations 123

1 Solar Neutrinos

Neutrinos are produced in the solar core when hydrogen is fused to form helium. As neutrinos are subject only to the weak interaction, they leave the solar core virtually unhindered, distinct from photons or any other radiation. They travel through about 700 000 km of solar matter and 1.5×10^8 km of interplanetary space in less than 10 minutes before they reach the earth, whereas photons need about 10^5 years just to reach the solar surface. Therefore the neutrinos, if detected, give information about the present state of the solar interior, while the electromagnetic radiation we receive comes only from the most superficial layers of the sun. By comparing the measured neutrino fluxes and spectra with theoretical predictions, the Standard Solar Model and, more generally, the theory of stellar structure and evolution can be tested.

From the particle physics point of view, the sun is a very intense low-energy electron neutrino source at a very large distance. It therefore provides important opportunities to investigate non-standard neutrino properties, such as non-zero rest mass, mixing between different flavours or a non-zero magnetic moment, on a level that is not accessible with 'man-made' neutrino sources (e.g. reactors, accelerators). In order to test neutrino properties by the detection of solar neutrinos, the neutrino fluxes and spectra generated by the source must be precisely known.

1.1 The Standard Solar Model

The sun is a main-sequence star at a stage of stable hydrogen burning. The Standard Solar Model (SSM, e.g. [Bah89, Bah01a]) gives a quantitative description of the sun. It is based on a set of plausible assumptions taking into account results of solar observations and laboratory measurements:

(1) Solar energy generation is due to thermonuclear fusion of hydrogen to helium

$$4\,\mathrm{p} \;+\; 2\,\mathrm{e}^- \;\rightarrow\; {}^4\mathrm{He} \;+\; 2\,\nu_\mathrm{e} \;+\; 26.73\,\mathrm{MeV} \;\; [\text{Bet39}].$$

On average, the electron neutrinos carry away 2 - 3 % of the energy (about 0.6 MeV). The detailed chain of fusion reactions is called pp-cycle and is shown in fig. 1.1. The CNO-cycle, which uses ^{12}C and ^{14}N as catalysts for the fusion reaction, becomes dominant only in stars with higher core temperatures and plays only a minor role in the sun (about 1.5 % of the energy production).

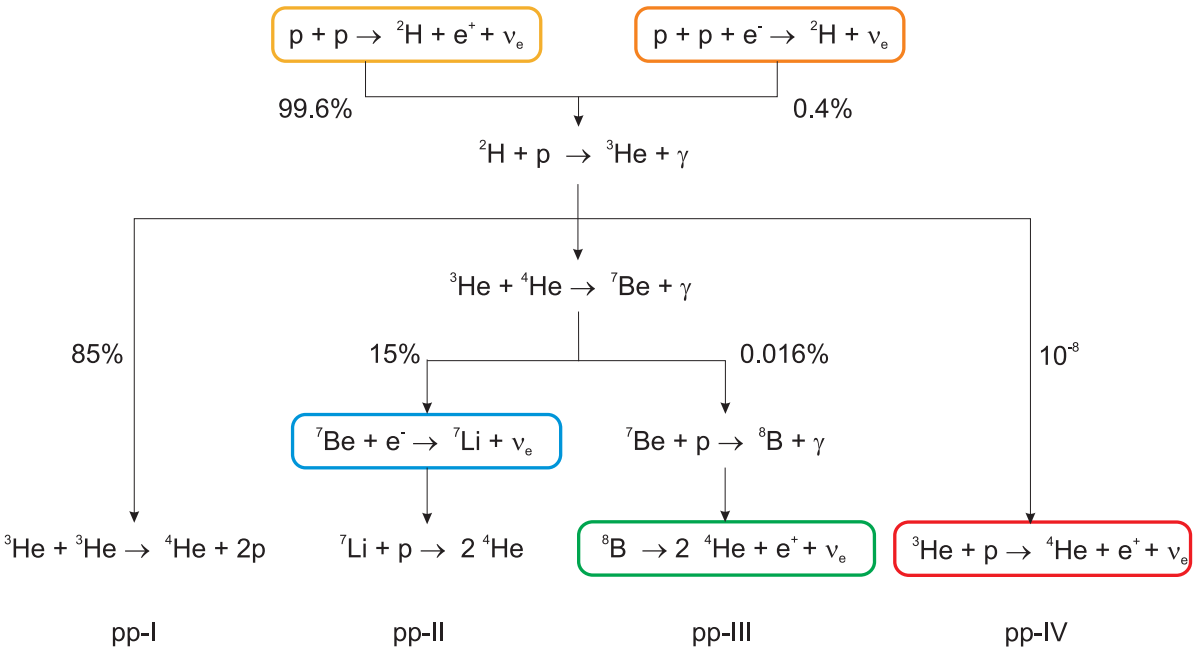

Figure 1.1: The pp-cycle is the dominant energy generation mechanism in the sun. It is subdivided into four chains: pp-I 85 %, pp-II 14 %, pp-III 0.016 %, pp-IV $\sim 10^{-8}$. The reactions, in which neutrinos are emitted, are framed.

(2) The sun is in hydrostatic and thermal equilibrium. This means that the hydrostatic pressure resulting from thermonuclear fusion counterbalances the gravity, and that the energy produced by nuclear reactions balances the total energy loss, which is the sum of the radiative energy flux (luminosity) and the energy carried away by neutrinos.

(3) Energy transport from the solar center, where nuclear fusion takes place ($r < 0.2\,R_\odot$), outwards to the surface occurs, apart from neutrinos, primarily by electromagnetic radiation and, for $r > 0.7\,R_\odot$, additionally by convection.

(4) Initially, the chemical composition of the sun was homogeneous. The local abundances of individual isotopes in the solar interior have slowly changed with time due to nuclear fusion, while in the surface layers the initial elemental abundances are preserved.

The boundary conditions for the model are the sun's known characteristics: the solar radius, mass, surface temperature, luminosity and age. Other measured input data are nuclear reaction cross sections, radiative opacities and isotopic abundances.

The system of differential equations for the solar structure and evolution is solved numerically. It yields, among other things, predictions for the solar core temperature T_c, the temperature and density profile inside the sun, and the rates at which the various nuclear fusion reactions contribute to the ^{4}He generation, hence the solar neutrino spectrum and flux. The solar neutrino spectrum according to the SSM [Bah98] is shown in fig. 1.2 and the expected neutrino fluxes on earth for the individual neutrino branches are listed in table 1.1.

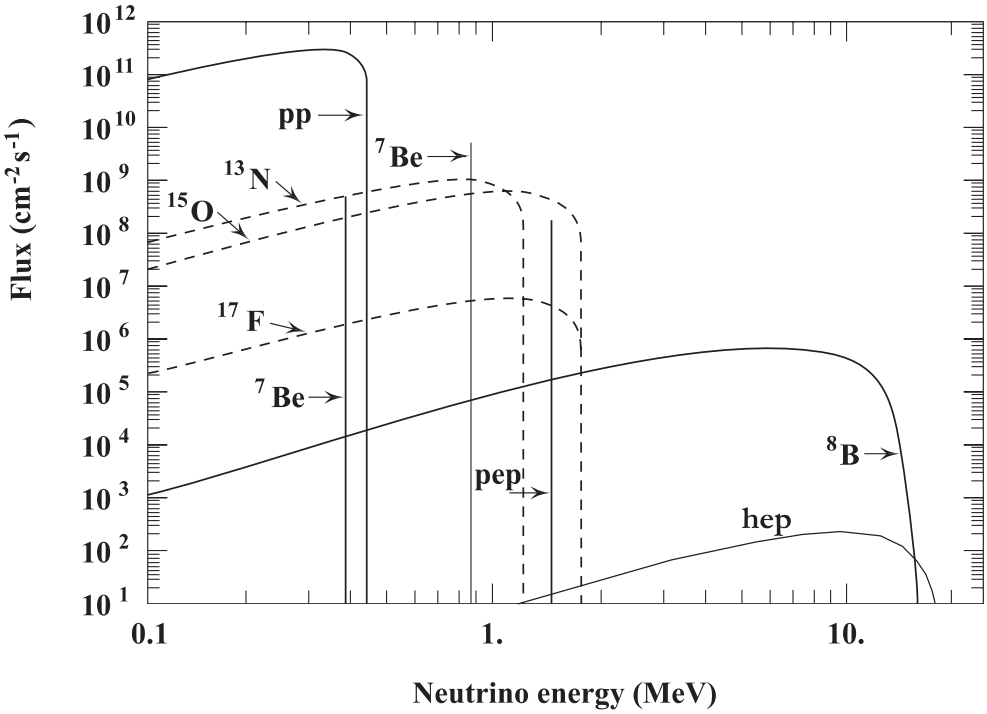

Figure 1.2: The solar neutrino spectrum predicted by the Standard Solar Model [Bah98]. Solid lines correspond to neutrinos from the pp-cycle, dotted lines to the CNO-cycle which plays only a minor role in the sun. Fluxes are given in units of $\mathrm{MeV}^{-1}\mathrm{cm}^{-2}\mathrm{s}^{-1}$ for continuous spectra and $\mathrm{cm}^{-2}\mathrm{s}^{-1}$ for lines at a distance of 1 Astronomical Unit.

neutrino branch	neutrino flux Φ_ν ($\mathrm{cm}^{-2}\mathrm{s}^{-1}$)	average energy $<E_\nu>$ (MeV)	maximum energy (MeV)
pp	$(5.95 \pm 0.06) \times 10^{10}$	0.2668	0.423
^{7}Be	$(4.77 \pm 0.48) \times 10^{9}$	0.863 (0.386)	0.863 (0.386)
^{8}B	$(5.05^{+1.01}_{-0.81}) \times 10^{6}$	6.735 ± 0.036	~ 15
pep	$(1.40 \pm 0.02) \times 10^{8}$	1.445	1.445
hep	9.3×10^{3}	9.628	18.778
^{13}N	$(5.48^{+1.15}_{-0.93}) \times 10^{8}$	0.7063	1.1982 ± 0.0003
^{15}O	$(4.80^{+1.20}_{-0.91}) \times 10^{8}$	0.9964	1.7317 ± 0.0005
^{17}F	$(5.63 \pm 1.41) \times 10^{6}$	0.9977	1.7364 ± 0.0003

Table 1.1: Energies and fluxes of the individual solar neutrino branches according to the SSM [Bah01a].

1.2 Detection of Solar Neutrinos

1.2.1 Detection Techniques

Neutrinos, as neutral and leptonic particles, are subject only to the weak interaction. This interaction may be mediated by either the charged $W^{\pm}$- or the neutral Z^0-bosons, referred to as charged current (CC) or neutral current (NC) interaction. Experimentally, solar neutrino detection is difficult due to the very low reaction cross sections for neutrino interaction with matter. Large target size, high detector sensitivity and effective background suppression are therefore characteristic features for solar neutrino experiments. The detectors are located deep underground to shield them from cosmic rays, and made from high radiopurity materials to minimize the internal background. Two major types of solar neutrino detectors are distinguished: radiochemical detectors (based on inverse beta-decay) and real-time experiments (Cerenkov or scintillation detectors).

Radiochemical Detectors

Radiochemical detectors use inverse beta decay to detect electron neutrinos via

$$\nu_{\mathrm{e}} + {}^{\mathrm{A}}_{\mathrm{Z}}\mathrm{X} \rightarrow \mathrm{e}^- + {}^{\mathrm{A}}_{\mathrm{Z+1}}\mathrm{Y},$$

where the nuclei X and Y have equal atomic number A, but different electric charge. The threshold energy for the neutrinos is defined by the Q-value of the reaction ($\mathrm{Q} = \mathrm{m_Y} + \mathrm{m_e} - \mathrm{m_X}$). The detection of other neutrino flavours than ν_e is not possible for solar neutrinos ($\mathrm{E}_{\nu,\mathrm{max}} \approx 15\,\mathrm{MeV}$), as the masses of the corresponding charged leptons, $\mathrm{m}_\mu = 106.95\,\mathrm{MeV}$ and $\mathrm{m}_\tau = 1777\,\mathrm{MeV}$, exceed $\mathrm{E}_{\nu,\mathrm{max}}$ by far. The product nucleus Y decays back to X with a short half life. The nuclei produced by neutrino interaction are extracted from the target after a sufficiently long exposure time (until equilibrium between production and decay is reached), and their back decay is measured. Radiochemical detectors integrate over all neutrino branches (with energies above the threshold), making the interpretation of their results more difficult.

Real-time Experiments

In contrast to the radiochemical detectors, real-time detectors yield the event time and energy. One reaction, that has been successfully applied to solar neutrino detection, is neutrino-electron scattering. This process is possible for neutrinos of all flavours

$$\nu_{\mathrm{x}} + \mathrm{e}^- \rightarrow \nu_{\mathrm{x}} + \mathrm{e}^- \quad (\mathrm{x} = \mathrm{e}, \mu, \tau)\,.$$

The scattered electron can be detected in a Cerenkov detector or a scintillation detector. The scattering of ν_e is possible due to both CC and NC, whereas $\nu_{\mu,\tau}$ scatter only via NC. The corresponding Feynman-diagrams are shown in fig. 1.3. Hence, if the flavour of solar neutrinos is converted from ν_e to ν_μ or ν_τ when arriving at earth, the count rate in such an experiment would be reduced significantly, but still be measurable. Neutrino-electron scattering is possible for neutrinos of all energies; the energy threshold of the individual experiments is set mainly due to background considerations.

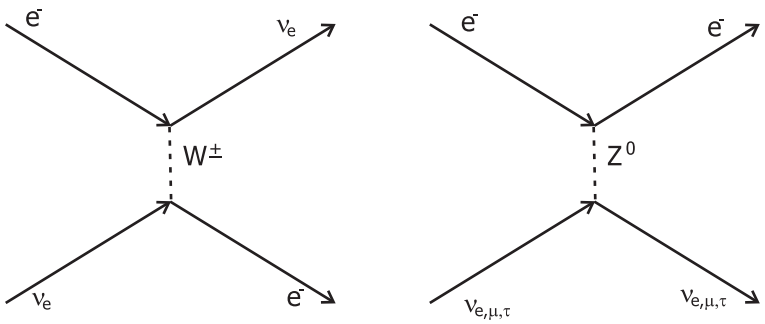

Figure 1.3: Feynman diagrams of neutrino electron scattering. Electron neutrinos scatter due to CC- and NC-interaction, the other flavours only due to NC-interaction.

1.2.2 Results from Solar Neutrino Experiments

The Homestake Chlorine Experiment

The Chlorine Experiment of R. Davis and collaborators started in 1968 [Dav68]. It is located in the Homestake mine in South Dakota (USA) at a depth of 4100 meters water equivalent (mwe). For the detection of the solar neutrinos the reaction

$$^{37}\mathrm{Cl} + \nu_\mathrm{e} \rightarrow {}^{37}\mathrm{Ar} + \mathrm{e}^-$$

with a threshold of 814 keV is used. The detector is therefore sensitive to electron neutrinos from all major neutrino branches except the pp neutrinos, mainly the ^{7}Be and ^{8}B neutrinos. The target consists of 615 tons of perchloroethylene ($\mathrm{C_2Cl_4}$). The ^{37}Ar atoms produced by solar neutrinos decay back to ^{37}Cl with a half life of 35 days. They are extracted every 60 - 70 days from the target, and their decay is measured in miniaturized proportional counters. The measured rate, averaged over 25 years of data taking (1970 - 1995)

$$\mathrm{R_{exp}} = (2.56 \pm 0.16\,(\mathrm{stat.}) \pm 0.16\,(\mathrm{sys.}))\,\mathrm{SNU}^1\ [\mathrm{Dav98}],$$

is roughly one third of the predicted rate

$$\mathrm{R_{SSM}} = (7.6\,^{+1.3}_{-1.1})\,\mathrm{SNU}\ [\mathrm{Bah01a}].$$

Kamiokande and Super-Kamiokande

The Kamiokande detector was originally built to look for proton decay (Kamioka nucleon decay experiment). It is located in the Kamioka mine (Japan) in a depth of 2700 mwe. It is a large water Cerenkov detector, and therefore able to measure neutrinos of all flavours via neutrino scattering on electrons

$$\nu_\mathrm{x} + \mathrm{e}^- \rightarrow \nu_\mathrm{x} + \mathrm{e}^- \quad (\mathrm{x} = \mathrm{e}, \mu, \tau)\,.$$

[1] 1 Solar Neutrino Unit = 1 neutrino interaction per 10^{36} target atoms per second

With this detection technique it is possible to measure the time of the event and the energy and direction of the recoil electron. Kamiokande began observing solar neutrinos in 1986 (almost two decades after the Chlorine experiment) with 680 tons of water, 1000 PMTs and a detection threshold of 7.5 MeV (limited due to background from natural radioactivity). The upgraded version, Super-Kamiokande, started data taking in 1996. With 50 000 tons of water (22 500 tons fiducial volume) and 12 000 PMTs, and thanks to the higher purity components and better shielding, Super-Kamiokande is able to measure down to a threshold of 5.5 MeV. The measured rate after 1117 days is

$$\mathrm{R_{exp}} = (2.40 \pm 0.03\,(\mathrm{stat.})\,^{+0.08}_{-0.07}\,(\mathrm{sys.})) \times 10^{6}\mathrm{cm}^{-2}\mathrm{s}^{-1}\ [\mathrm{Suz01}].$$

The comparison with the theoretical prediction [Bah98] leads to a ratio of

$$\mathrm{R_{exp}/R_{SSM}} = 0.465 \pm 0.005\,(\mathrm{stat.})\,^{+0.015}_{-0.013}\,(\mathrm{sys.})\,.$$

The shape of the measured ^{8}B neutrino spectrum is consistent with no distortion. As a real-time detector, Super-Kamiokande is able to measure the day flux and night flux separately. The ratio obtained is

$$\frac{\mathrm{N-D}}{(\mathrm{N+D})/2} = 0.034 \pm 0.022\,(\mathrm{stat.})\,^{+0.013}_{-0.012}\,(\mathrm{sys.})\,.$$

The Gallium Experiments: GALLEX, GNO and SAGE

To observe the low energy pp neutrinos, which have a maximum energy of 422 keV, V. Kuzmin proposed in 1966 [Kuz66] a radiochemical experiment based on the inverse beta decay

$$^{71}\mathrm{Ga} + \nu_{\mathrm{e}} \rightarrow {}^{71}\mathrm{Ge} + \mathrm{e}^{-}$$

with a threshold of 233 keV. There are two experiments using this reaction: GALLEX (renamed GNO in 1998) in the INFN Gran Sasso underground laboratory (Italy) at a depth of 3600 mwe, and SAGE in the INR Baksan valley neutrino laboratory in the Caucasus mountains (Russia) at a depth of 4700 mwe. The target consists of 30 tons gallium in an aqueous gallium chloride solution for GNO, and of 60 tons of metallic gallium for SAGE. The germanium nuclides produced by solar neutrinos are extracted from the target every 4 - 5 weeks, and their back decay ($t_{1/2} = 11.4$ d) is measured in low background proportional counters. The prediction for the gallium experiments is

$$\mathrm{R_{SSM}} = (129\,^{+8}_{-9})\ \mathrm{SNU}\ [\mathrm{Bah98}].$$

GALLEX measured after 7 years a signal of

$$\mathrm{R_{exp}} = (77.5 \pm 6.2\,(\mathrm{stat.})\,^{+4.3}_{-4.7}\,(\mathrm{sys.}))\,\mathrm{SNU}\ [\mathrm{Ham99}],$$

the successor GNO measured after 2 years

$$\mathrm{R_{exp}} = (65.8\,^{+10.2}_{-9.6}\,(\mathrm{stat.})\,^{+3.4}_{-3.6}\,(\mathrm{sys.}))\,\mathrm{SNU}\ [\mathrm{Alt00}].$$

SAGE obtains a similar result

$$\mathrm{R_{exp}} = (75.4\,^{+7.0}_{-6.8}\,(\mathrm{stat.})\,^{+3.5}_{-3.0}\,(\mathrm{sys.}))\,\mathrm{SNU}\ \ [\mathrm{Gav01}].$$

Both experiments tested the overall detector response with intense man-made ^{51}Cr neutrino sources, and observed a good agreement between the measured and predicted ^{71}Ge production rates.

The Sudbury Neutrino Observatory (SNO)

The SNO experiment is located in the Creighton mine near Sudbury (Canada) at a depth of 5000 mwe. The detector consists of 1000 tons of heavy water (D_2O) contained in an acrylic sphere, viewed by 9500 photomultipliers, and shielded by a 3 m layer of light water (H_2O). The main feature of SNO is its ability to discriminate between charged current and neutral current reactions [McD01].
The neutrino detection reactions are:

$$\begin{array}{lcll} \nu_{\mathrm{x}} + \mathrm{e}^- & \rightarrow & \nu_x + e^- & \text{elastic scattering} \\ \nu_e + {}^2H & \rightarrow & p + p + e^- & \text{CC, threshold 1.44 MeV} \\ \nu_x + {}^2H & \rightarrow & p + n + \nu_x & \text{NC, threshold 2.2 MeV .} \end{array}$$

The electrons are detected via the Cerenkov effect, with an electron energy threshold of about 6 MeV. The neutrons are thermalized and eventually captured by deuterium, followed by the emission of 6.25 MeV gammas. For the second phase of the experiment the SNO collaboration has added recently NaCl to the heavy water in order to enhance the neutron detection by neutron capture on Cl, followed by an 8.6 MeV gamma ray cascade.

SNO started data taking in May 1999. On the 18th of June 2001 the SNO collaboration released their first results on the measurement of the CC interaction of the ^{8}B neutrinos [Ahm01]. The measured ν_e flux is

$$\Phi^{\mathrm{CC}}(\nu_{\mathrm{e}}) = 1.75 \pm 0.07(\mathrm{stat.})^{+0.12}_{-0.11}(\mathrm{sys.}) \pm 0.05(\mathrm{theor.}) \times 10^6 \mathrm{cm}^{-2}\mathrm{s}^{-1}\,.$$

The flux inferred from the electron scattering (ES), assuming no flavour transformation, is

$$\Phi^{\mathrm{ES}}(\nu_{\mathrm{x}}) = 2.39 \pm 0.34(\mathrm{stat.})^{+0.16}_{-0.14}(\mathrm{sys.}) \times 10^6 \mathrm{cm}^{-2}\mathrm{s}^{-1}\,.$$

Comparison of the two rates yields a 1.6 σ difference. Comparing the CC rate of SNO with the ES rate measured by Super-Kamiokande yields a 3.3 σ difference, providing evidence that there is a non-electron flavour active neutrino component in the solar neutrino flux. The cross section of $\nu_{\mu,\tau}$ for electron scattering is about a factor of 6 lower than for ν_e. The total flux of ^{8}B neutrinos can therefore be determined to

$$\Phi(\nu_{^8\mathrm{B}}) = 5.44 \pm 0.99 \times 10^6 \mathrm{cm}^{-2}\mathrm{s}^{-1}\,,$$

which is in agreement with the prediction of the SSM $(5.05^{+1.01}_{-0.81}) \times 10^6 \mathrm{cm}^{-2}\mathrm{s}^{-1}$ [Bah01a].

1.2.3 Future Experiments

Borexino and KamLAND

BOREXINO and KamLAND [Bra00, Pie01] both aim to detect solar ^{7}Be neutrinos by neutrino-electron scattering using liquid scintillation spectroscopy. The physics goals and the design of BOREXINO will be described in more detail in chap. 2. The design of KamLAND is very similar to that of BOREXINO, but with three times larger scintillator mass (1000 t). The KamLAND detector is currently under construction in the old Kamioka site (Japan); data taking will start in 2001. The first stage of KamLAND is primarily devoted to detecting reactor antineutrino oscillations. At a later time, low-energy solar neutrino detection is also envisioned, but this will require an additional improvement of radiopurity beyond the present design specifications.

LENS

The LENS project (low energy neutrino spectrometer) aims for real-time spectroscopy of solar electron neutrinos in the sub-MeV energy range [Rag97, Cri00]. It will use scintillator loaded with ^{176}Yb, ^{160}Gd or ^{115}In for the detection of the inverse beta decay

$$\begin{aligned} {}^{176}\mathrm{Yb} + \nu_\mathrm{e} &\rightarrow e^- + {}^{176}\mathrm{Lu}^\star \quad (\mathrm{E}_\nu > 245\mathrm{keV}) \\ {}^{160}\mathrm{Gd} + \nu_\mathrm{e} &\rightarrow e^- + {}^{160}\mathrm{Tb}^\star \quad (\mathrm{E}_\nu > 301\mathrm{keV}) \\ {}^{115}\mathrm{In} + \nu_\mathrm{e} &\rightarrow e^- + {}^{115}\mathrm{Sn}^\star \quad (\mathrm{E}_\nu > 118\mathrm{keV}) \end{aligned}$$

Characteristic electron-gamma coincidence signatures due to isomeric states occupied in the daughter nuclei (with lifetimes of ~ 100 ns) could help to achieve the required background reduction at very low energies. Combining the measured CC-rate of ^{7}Be neutrinos in LENS with the rate measured in BOREXINO (CC + NC) could give an unambiguous proof of neutrino oscillations.

1.3 The Solar Neutrino Puzzle

1.3.1 Implications from the Experimental Results

The major results from the experiments described in the last section are graphically shown in fig. 1.4 and compared to the expected values based on the SSM according to [Bah01a].

As can be seen from this figure, the measured solar neutrino fluxes are, in all instances, substantially lower than the predictions of the SSM. This discrepancy constitutes the “first solar neutrino problem”.

Translating the ^{8}B neutrino rate measured by Super-Kamiokande (about 50 %) into an expectation value for the Chlorine experiment, the result is (3 ± 0.5) SNU. Compared with the measured signal of (2.56 ± 0.22) SNU there is almost no space left for the ^{7}Be neutrinos, which theoretically should contribute to about 15 % of the Chlorine signal. This problem is known as the “second solar neutrino problem”, or the problem of the missing ^{7}Be neutrinos.

A “third solar neutrino problem” emerges from the gallium detector results: the measured rate is just sufficient to account for the pp neutrinos whose flux is determined by the luminosity of the sun. Again, there is almost no room for ^{7}Be neutrinos.

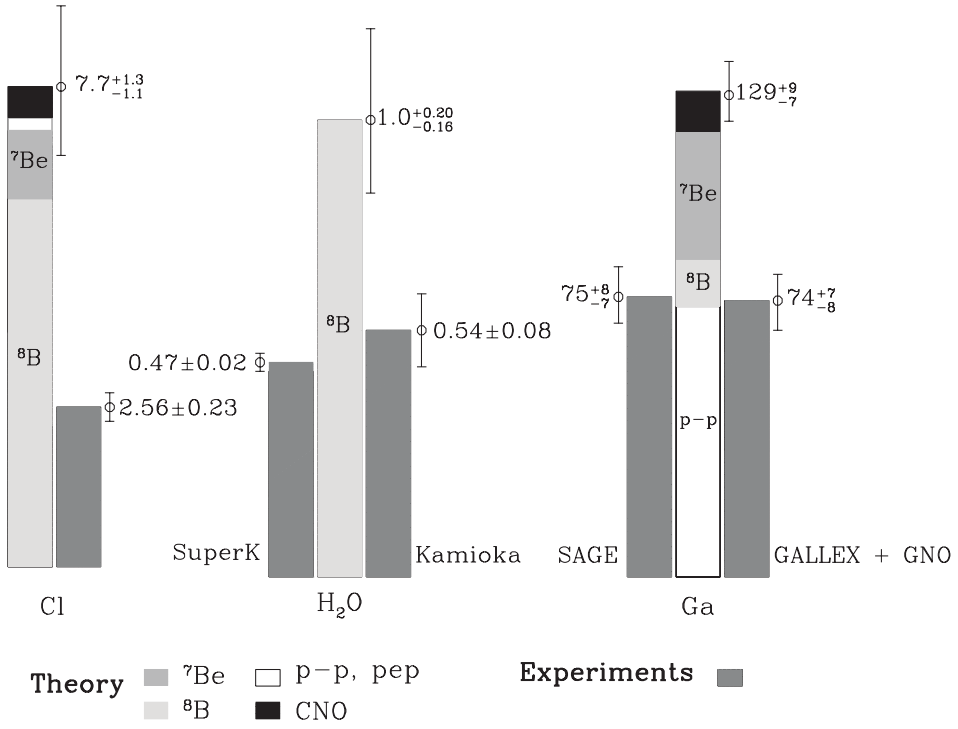

Figure 1.4: The expected total rates of the solar neutrino experiments according to the SSM [Bah01a] compared with the measured values.

1.3.2 Astrophysical Solutions

After the results of the Homestake experiment, the solar neutrino deficit was assumed to be mainly a ^{8}B deficit. As the ^{8}B flux has a very strong temperature dependence, all that is needed to reduce the ^{8}B neutrino flux is a reduction of the central temperature. However, it turns out that this cannot be achieved in the frame of the SSM without severely affecting other outputs of the model. As a consequence, many nonstandard solar models have been proposed to explain the solar neutrino problem (see fig. 1.5). Most nonstandard models are especially tailored to reduce the ^{8}B neutrino flux by various mechanisms which lower the central temperature (e.g. turbulent diffusion, axion emission). As the temperature dependence of the three main neutrino branches is [Bah96]

$$\Phi_{pp} \propto T^{-1.1}, \qquad \Phi_{^7Be} \propto T^{10}, \qquad \Phi_{^8B} \propto T^{24},$$

a reduced central temperature of the sun would affect the ^{8}B neutrinos more than the ^{7}Be neutrinos, and thus cannot explain the stronger suppression of the ^{7}Be neutrino flux.

Within recent years, accurate measurements of solar seismic modes have allowed to independently infer the sound speed $c_s(r)$ and thereby the solar density profile, inwards to about $0.05\,R_\odot$. Confronting the results from helioseismology with the solar model predictions shows an intriguing agreement, better than 1 % fractional dicrepancy [Bah01a]. This result supports the standard solar model as a reliable description of the sun and strongly disfavours most nonstandard solar models.

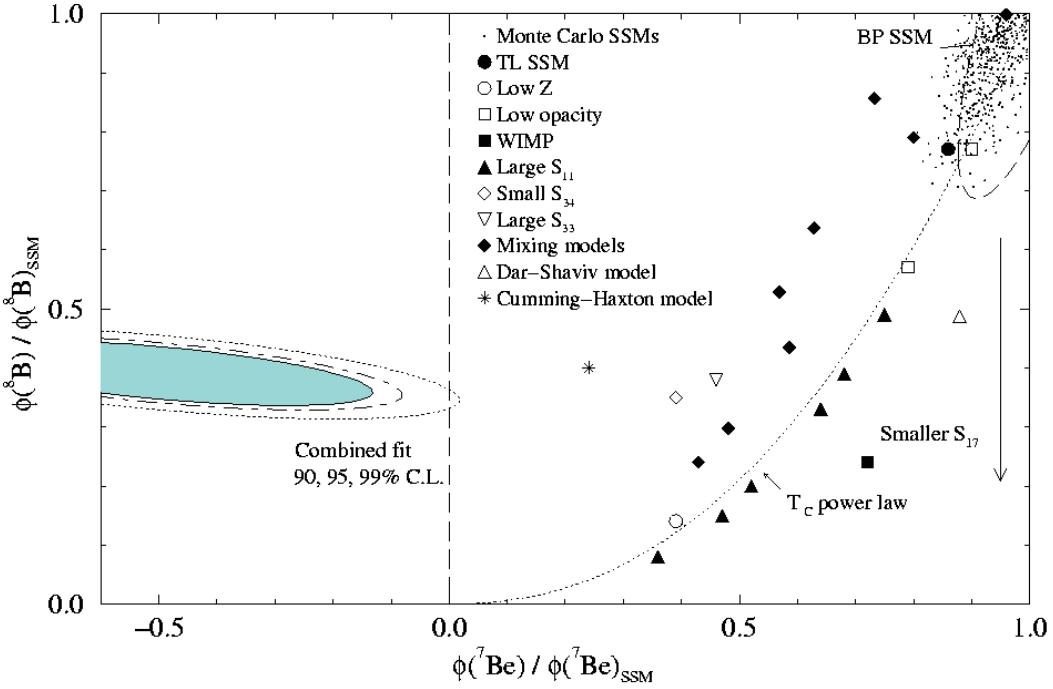

Figure 1.5: Combined fit of the results of the solar neutrino experiments (Chlorine, GALLEX, SAGE, Kamiokande) for the ^{7}Be and ^{8}B neutrino flux. Also shown are the predictions of various standard and nonstandard solar models. From [Hat97].

1.3.3 Nuclear Physics Solutions

Another solution scenario focuses on the nuclear physics side, the determination of the cross-sections for the individual fusion reactions of the pp-chain. These cross sections are accessible in laboratory experiments only at higher energies and are extrapolated down to the low energies relevant for the solar interior (few keV). By a variation of some of the reaction rates the individual neutrino branches can be suppressed differently, which seems to provide a possibility to resolve the discrepancy between the measured and predicted neutrino fluxes. To reduce the ^{8}B neutrino flux down to the measured value, an enhancement of S_{33} (e.g. due to a low energy resonance) or a reduction of S_{34} would be needed, and to suppress the ^{7}Be neutrino flux more than the ^{8}B neutrinos, an enhancement of the S_{17} would be needed. However, in a model-independent analysis of the results of the solar neutrino experiments it can be shown that tremendous changes in these reaction rates would be needed, which exceed the uncertainties of the measured cross sections by more than $10\,\sigma$ [Sch99a]. The measurement of the S_{33} down to 20 keV, which is the center of the solar Gamow peak for this reaction, didn't show any evidence for a significant enhancement [Bon99]. Recent measurements of the S_{17} indicate an even lower value than the one used in older SSM calculations [Ade98].

1.3.4 Neutrino Oscillations

An alternative and more likely path towards the solution of the Solar Neutrino Puzzle explores new neutrino physics, outside the boundaries of the Standard Model of electroweak interaction. If neutrinos have nonstandard properties, such as mass, magnetic moment and a non zero flavour mixing angle, they can take part in different physical processes that lower their rate of detection. I will discuss here only the phenomena of neutrino oscillations in vacuum and matter. A more detailed description of these phenomena can be found in [Bil99].

Neutrino Oscillations in Vacuum

The idea that neutrinos can oscillate between leptonic flavours was first suggested by Bruno Pontecorvo [Pon58a, Pon58b, Pon68]. This is a non standard phenomenon that takes place only if at least one of the neutrino states has non zero mass and if the lepton family number is not conserved.

The neutrino flavour eigenstates ν_α ($\alpha = e, \mu, \tau$) can be expressed as a linear combination of the mass eigenstates ν_i ($i = 1, 3$), which describe the free particle propagation in vacuum

$$|\nu_\alpha\rangle = \sum_i U_{\alpha i} |\nu_i\rangle \,, \quad \text{with } U^\dagger U = 1 \,.$$

The mixing matrix U is an analogy to the Cabbibo-Kobayashi-Maskawa matrix in the quark sector. In the case of mixing leptonic flavours, this matrix is non-diagonal.
If at the initial time $t = 0$ the state of neutrino is $|\nu_\alpha\rangle$, then the neutrino state at the time t is

$$|\nu(t)\rangle = \sum_i U_{\alpha i} e^{-iE_i t} |\nu_i\rangle \,.$$

Using the unitarity of the mixing matrix this can be written as

$$|\nu(t)\rangle = \sum_{i,\beta} U_{\alpha i} U^{\star}_{\beta i} e^{-iE_i t} |\nu_\beta\rangle \, .$$

The transition amplitude $A(\nu_\alpha \to \nu_\beta; t)$ is

$$A(\nu_\alpha \to \nu_\beta; t) = \langle \nu_\beta | \nu(t) \rangle = \sum_i U_{\alpha i} U^{\star}_{\beta i} e^{-iE_i t} \, ,$$

and the transition probability

$$P(\nu_\alpha \to \nu_\beta; t) = |\, A(\nu_\alpha \to \nu_\beta; t)|^2 = \Big| \sum_i U_{\alpha i} U^{\star}_{\beta i}\, e^{-iE_i t} \Big|^2 \, .$$

For the case of relativistic neutrinos ($p_i \gg m_i$) we can use the approximation

$$E_i = \sqrt{p^2 + m_i^2} \simeq p + \frac{m_i^2}{2p} \simeq E + \frac{m_i^2}{2E}$$

and write the transition probability as

$$P(\nu_\alpha \to \nu_\beta; t) = \left| \delta_{\alpha\beta} + \sum_{i=2}^{3} U_{\alpha i} U^{\star}_{\beta i} \left(\exp(-i \frac{\Delta m^2_{i1} L}{2E}) - 1 \right) \right|^2 \, .$$

It is clear that flavour transitions can occur only if neutrino mixing exists ($U \neq I$), and if at least one $\Delta m^2_{ij} \neq 0$.

Oscillations in the Two-Neutrino Case

In the simplest case of mixing only between two neutrino flavours the mixing matrix can be written as

$$U = \begin{pmatrix} \cos\theta & \sin\theta \\ -\sin\theta & \cos\theta \end{pmatrix}$$

and the transition probability is given by

$$P(\nu_\alpha \to \nu_\beta; t) = \frac{1}{2} \sin^2 2\theta \left(1 - \cos 2\pi \frac{L}{L_{\rm osc}} \right)$$

where $L_{\rm osc}$ is the oscillation length

$$L_{\rm osc} = 4\pi \frac{E}{\Delta m^2} \simeq 2.47 \, \frac{E}{1{\rm MeV}} \cdot \frac{1{\rm eV}^2}{\Delta m^2} \, {\rm m} \, .$$

Therefore the transition probability is a periodic function of L/E. This phenomenon is called neutrino oscillations. The oscillations can be observed if the oscillation length is not much larger than the distance source - detector

$$L \geq L_{\rm osc} \, .$$

Neutrino Source	$\mathbf{L/E}$ (m/MeV)	$\mathbf{\Delta m^2(eV^2)}$
Reactor	$1 - 10^2$	$10^{-3} - 10^{-1}$
Accelerator	$10^{-2} - 10$	$10^{-2} - 10$
Atmosphere	$10^2 - 10^4$	$10^{-5} - 10^{-3}$
Sun	$10^{10} - 10^{11}$	$10^{-12} - 10^{-11}$
Supernova	$10^{19} - 10^{20}$	$10^{-20} - 10^{-21}$

Table 1.2: Sensitivity level of different types of neutrino oscillation experiments depending on the neutrino energy and the distance source - detector [Bah89].

This inequality allows to estimate the sensitivity to the parameter Δm^2 of different types of neutrino experiments (assuming large mixing angles). These estimates are presented in table 1.2.

Neutrino Oscillations in Matter (MSW-Effect)

Neutrino oscillations in matter were first investigated by Wolfenstein [Wol78]. Mikheyev and Smirnov found a resonance effect in matter that strongly enhances the oscillation probability [Mik85] for electron neutrinos when traveling through a region with variable electron density. During the propagation of the neutrinos through the sun they coherently scatter forward on the particles of the solar plasma. Unlike μ- and τ-neutrinos, which only interact via NC-reactions, electron-neutrinos can in addition couple via $W^{\pm}$-bosons to the electrons. Therefore, the scattering cross section of ν_e is enhanced compared to the one of the other two neutrino flavours. The difference in the forward scattering amplitudes for electron and muon neutrinos is

$$f_{\nu_e e}(0) - f_{\nu_{\mu,\tau} e}(0) = -\frac{G_F p}{\sqrt{2}\pi}\,,$$

where G_F denotes the Fermi constant and p the momentum of the neutrino. The forward scattering amplitude is related to the refractive index via the optical theorem,

$$n_\alpha - 1 = \frac{2\pi N_e}{p^2} f_\alpha(0)\,,$$

where N_e is the particle density of electrons. Thus, the refractive index is different for ν_e than for $\nu_{\mu,\tau}$

$$n_{\nu_e} - n_{\nu_{\mu,\tau}} = \frac{2\pi N_e}{p^2}\left[f_{\nu_e e}(0) - f_{\nu_{\mu,\tau} e}(0)\right] = \frac{\sqrt{2} G_F N_e}{p}\,.$$

The oscillation length for electron neutrinos in matter then becomes

$$L_{\mathrm{mat}} = \frac{2\,\pi}{\sqrt{2} G_F N_e} = \frac{1.6}{\rho_e} \times 10^7\,\mathrm{m}$$

where ρ_e is the electron number density in units of Avogadro's number. The oscillation length in matter is independent from the neutrino energy. It is $\sim$ 200 km in the sun's core and $\sim$

10^4 km in the earth. The mixing angle in matter θ_{mat} is related to the one in vacuum by the relation

$$\sin^2 2\theta_{\mathrm{mat}} = \frac{\sin^2 2\theta}{(\cos 2\theta - L_{\mathrm{osc}}/L_{\mathrm{mat}})^2 + \sin^2 2\theta} \,.$$

This expression has a resonance for

$$\frac{L_{\mathrm{osc}}}{L_{\mathrm{mat}}} = \cos 2\theta \,.$$

Thus, for regions with

$$\rho_c = \frac{\cos 2\theta \Delta m^2}{2\sqrt{2} G_F E}$$

there is local maximal mixing

$$\sin^2 2\theta_{\mathrm{mat}} = 1 \quad \Rightarrow \quad \theta_{\mathrm{mat}} = 45^\circ$$

even though the vacuum mixing angle θ can be very small. As from the solar core to the surface, the density of the matter decreases from $\sim$150 g/cm^3 in the core to zero at the surface, this condition can be fulfilled for all electron neutrinos produced in the solar core with energies above a given threshold:

$$E > E_c = \frac{\Delta m^2 \cos 2\theta}{2\sqrt{2} G_F N_e}$$

The neutrinos with energies $E > E_c$ are generated in the solar core ($\rho > \rho_c$) as electron neutrinos, which in the high density region are mainly constituted by the heavier mass eigenstate. Under adiabatic conditions no transitions between the heavy and the light eigenstate occur, so that the neutrino leaves the sun as a neutrino of a different flavour. In the non-adiabatic case, the conversion is only partial. The phenomenon of neutrino oscillations in matter can also take place inside the earth: electron neutrinos that have been converted into other flavours inside the sun, can regenerate while crossing the earth, leading to a day/night asymmetry in the detected neutrino rate.

Neutrino-Oscillation Solutions to the Solar Neutrino Problem

A global analysis of the Homestake, SAGE, GALLEX+GNO and Super-Kamiokande results leaves only a few allowed regions in the $\Delta m^2 - \tan^2\theta$ plane. These are shown in fig. 1.6 [Bah01b]. The choice of the variable $\tan^2\theta$ rather than $\sin^2(2\theta)$ allows to include also mixing angles larger than $\pi/4$ (the so-called dark side). The no-oscillation hypothesis is excluded at 99.7 % C.L. (3σ).

The latest results from Super-Kamiokande [Fuk01] and SNO [Ahm01] disfavour the possibility of oscillations to sterile neutrinos and prefer the solutions with large mixing angles ($\sin^2(2\theta) \approx 1$), e.g. [Fog01, Bah01b]. The best fit values for the global analysis including the SNO results are listed in table 1.3 and shown in fig. 1.7 [Bah01b]. The CC measurement by SNO has not changed qualitatively the globally allowed solution space for solar neutrinos, though it has provided convincing evidence for neutrino oscillations into active neutrinos. I will show in the next chapter, that the BOREXINO experiment has the potential to distinguish between the currently allowed oscillation scenarios.

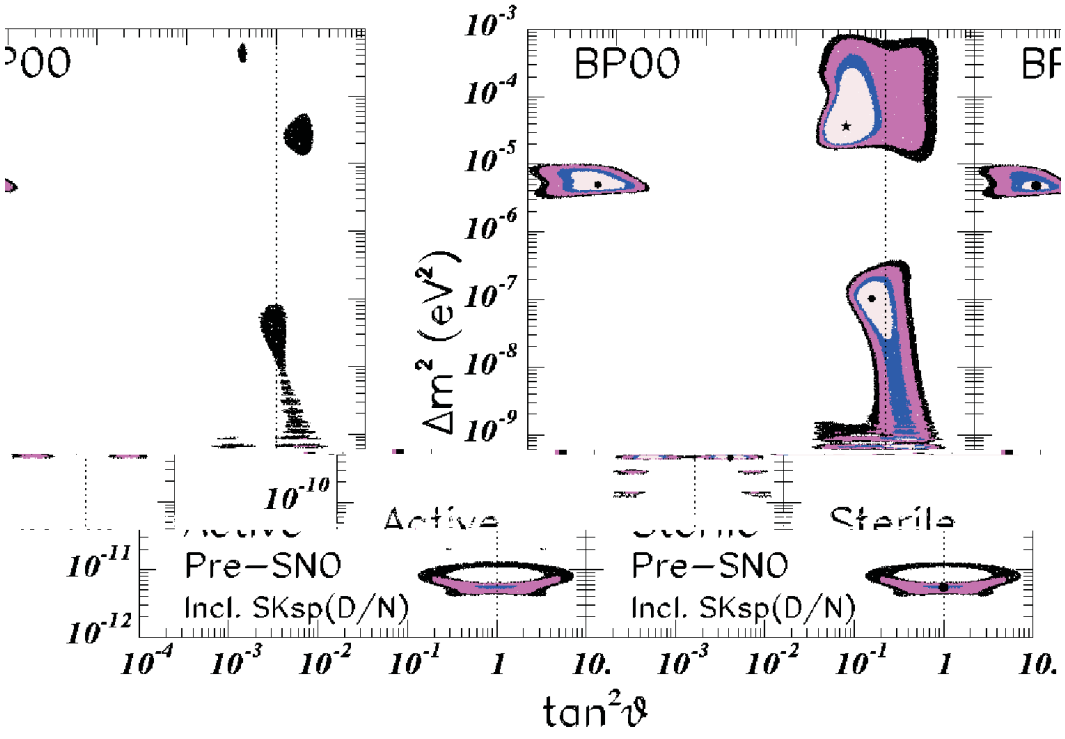

Figure 1.6: Global analysis of the Homestake, SAGE, GALLEX/GNO and Super-Kamiokande results, taking into account the total rates, and the ^{8}B energy spectrum measured by Super-Kamiokande separately during the day and during the night as well as the theoretical neutrino fluxes according to BP00. The MSW solutions are known as "small mixing angle", "large mixing angle" and "low" solution, respectively. The contours correspond to 90 %, 95 %, 99 % and 99.73 % C.L. relative to each of the best-fit solutions (marked with black circles). Taken from [Bah01b].

Solution	$\mathbf{\Delta m^2(eV^2)}$	$\tan^2(\theta)$	$\chi^2_{\min}$	**g.o.f.**
LMA	$4.5 \cdot 10^{-5}$	$4.1 \cdot 10^{-1}$	35.3	59 %
LOW	$1.0 \cdot 10^{-7}$	$7.1 \cdot 10^{-1}$	38.4	45 %
VAC	$4.6 \cdot 10^{-10}$	$2.4 \cdot 10^{0}$	39.0	42 %
SMA	$4.7 \cdot 10^{-6}$	$3.9 \cdot 10^{-4}$	45.4	19 %
Just So^2	$5.5 \cdot 10^{-12}$	$0.67(1.5) \cdot 10^{0}$	45.7	18 %
Sterile Just So^2	$5.5 \cdot 10^{-12}$	$0.67(1.5) \cdot 10^{0}$	45.8	18 %
Sterile SMA	$4.5 \cdot 10^{-6}$	$3.1 \cdot 10^{-4}$	46.6	16 %
Sterile VAC	$4.7 \cdot 10^{-10}$	$2.7 \cdot 10^{-1}$	47.2	15 %

Table 1.3: Best-fit global oscillation parameters and goodness-of-fit (calculated from $\chi^2_{\min}$/d.o.f.) with all available solar neutrino data, including the SNO CC measurement, using the BP00 theoretical neutrino fluxes. From [Bah01b].

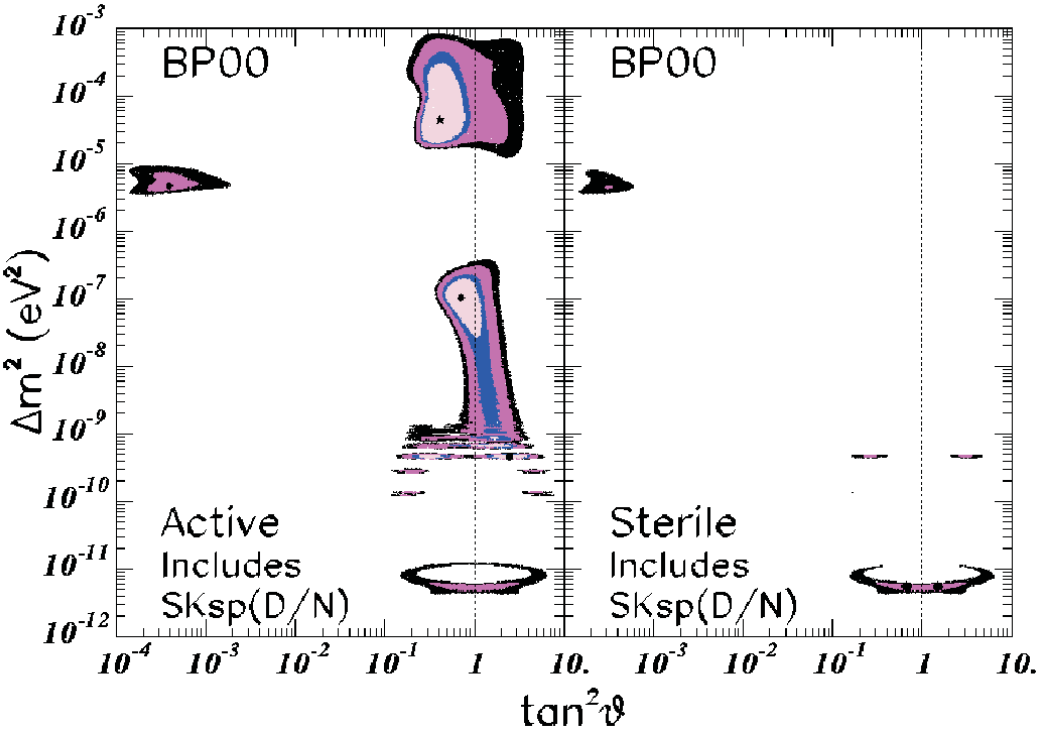

Figure 1.7: Global oscillation solutions including all available solar neutrino data. Taken from [Bah01b].

2 The Borexino Experiment

2.1 Physics Goals

The goal of BOREXINO is to measure for the first time, in real-time, the monoenergetic flux of the ^{7}Be-neutrinos from the sun ($E_\nu = 862\,\mathrm{keV}$). BOREXINO will detect neutrinos by elastic scattering on electrons. This process can occur via charged- or neutral-current interactions (exchange of a $W^\pm$- or Z^0-boson respectively), and is therefore sensitive to neutrinos of all flavours. Even in the case of complete conversion of the electron neutrinos to neutrinos of other flavours the count rate will still be measurable, though significantly reduced. The expected count rate in BOREXINO is about $50\,\mathrm{d}^{-1}$ according to the SSM, and about $12\,\mathrm{d}^{-1}$ in the case of complete conversion to other active neutrino flavours. Only conversion into sterile neutrinos could lead to an even lower count rate. Fig. 2.1 shows the expected count rates in BOREXINO for the most interesting oscillation scenarios.

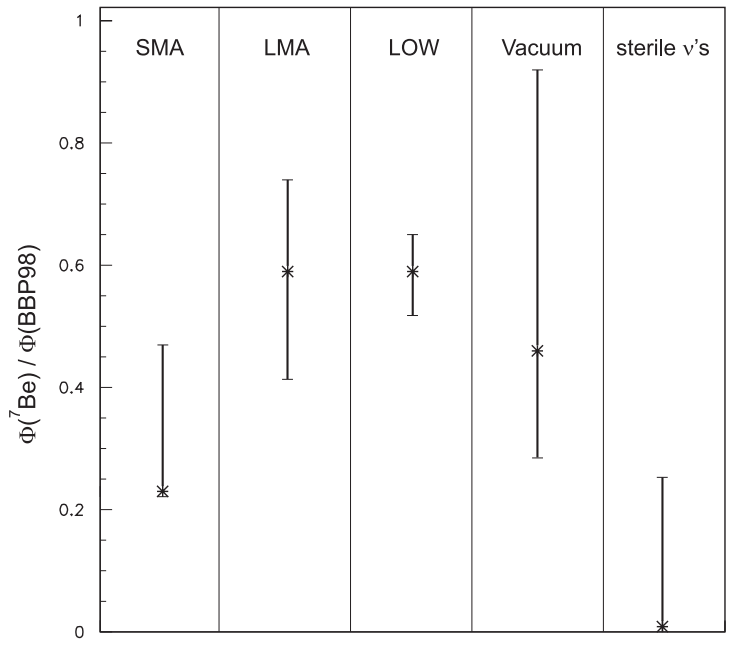

Figure 2.1: The expected signal rate in BOREXINO (99 % C.L.) for the different oscillation scenarios. The values are given relative to the SSM [Bah98].

The relatively high statistics of the ^{7}Be-neutrino signal allows the observation of time dependent effects, such as seasonal or diurnal variations. Distinguishing between the different possible solutions to the solar neutrino problem should be possible by using both the rate and the time dependence of the signal (see fig. 2.3):

- In the case of the **SMA** solution the ^{7}Be neutrinos are fully converted to other active neutrino flavours during passage through the sun. The ^{7}Be signal in BOREXINO in this case would be due solely to neutral current scattering and the rate would be reduced to about 24 % of the SSM signal.
- In the **LMA** solution the ^{7}Be neutrinos are not fully converted and the rate would be reduced to about 60 % of the SSM rate. For BOREXINO the only measurable difference between the SMA and LMA solutions is the total count rate.

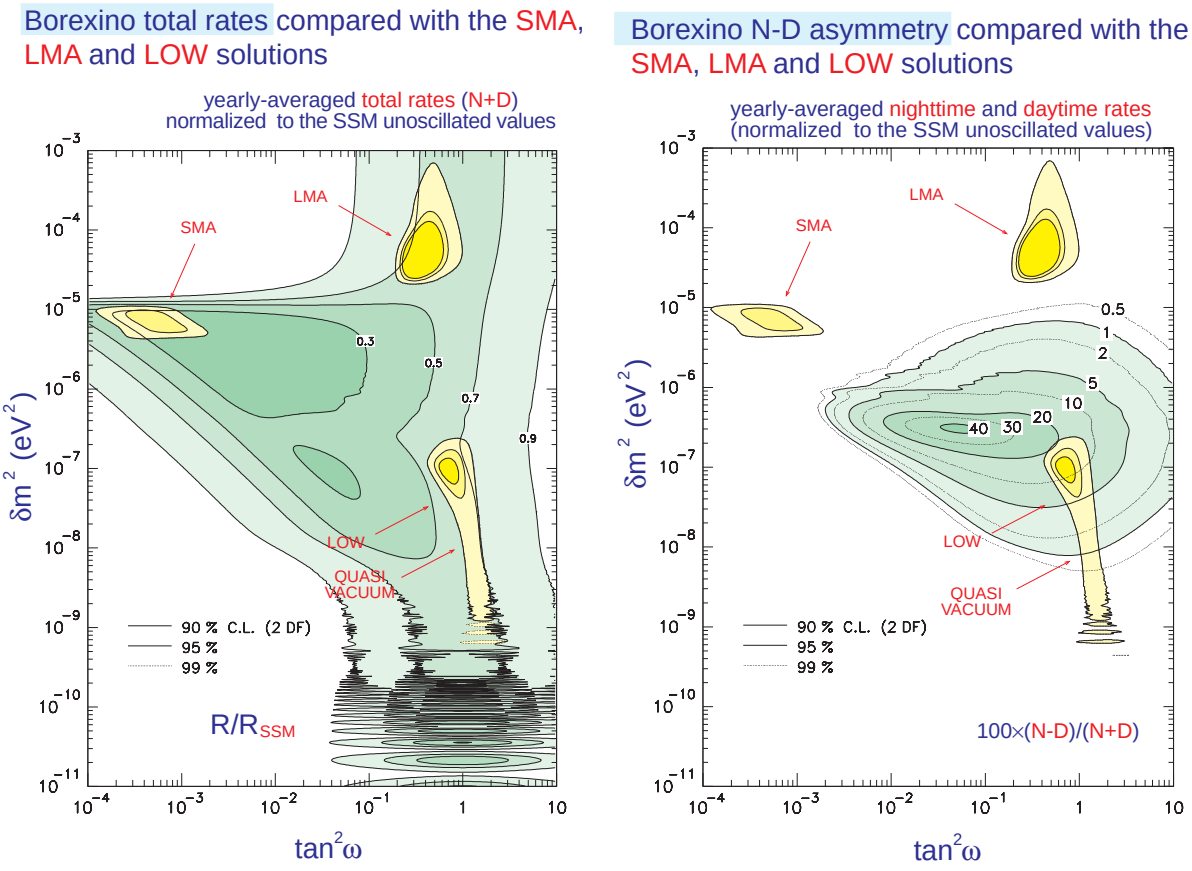

Figure 2.2: Expected count rates in BOREXINO for the different MSW scenarios. The choice of the variable $\tan^2\omega$ ($\omega = \theta_{12}$) rather than the usual $\sin^2(2\omega)$ allows an expanded view of the large mixing region. BOREXINO has the potential to discriminate between SMA, LMA and LOW solution using both information about total rates and the day-night-asymmetry.

- For the **LOW** solution there is also an incomplete conversion of ν_e in the sun, but there is a resonant regeneration of ν_e inside the earth which would lead to a significantly higher count rate during the night hours than during the day, the so-called “day-night effect”. This effect is maximal in the energy region below 1 MeV(see fig. 2.3). BOREXINO, which is the only real-time experiment measuring neutrinos at these low energies, would see a day-night difference of 10 - 20 %.

- The eccentricity of the earth’s orbit causes an annual variation of the solar neutrino flux, with a difference of ~ 7 % between perihelion and aphelion. For $\Delta m^2 \simeq 5{\cdot}10^{-10}\,\mathrm{eV}^2$ the **vacuum oscillation** length for ^{7}Be neutrinos is about 3 % of the sun-earth distance. This would lead to significant seasonal variations of the counting rate (see fig. 2.4), as the oscillation probability changes with the distance from the sun.

- In the case of **oscillations into sterile neutrinos**, the conversion of the electron neutrinos is almost complete. As the sterile neutrinos don’t interact in any way in the detector, the measured count rate in BOREXINO would range from 0 to 25 % of the SSM flux.

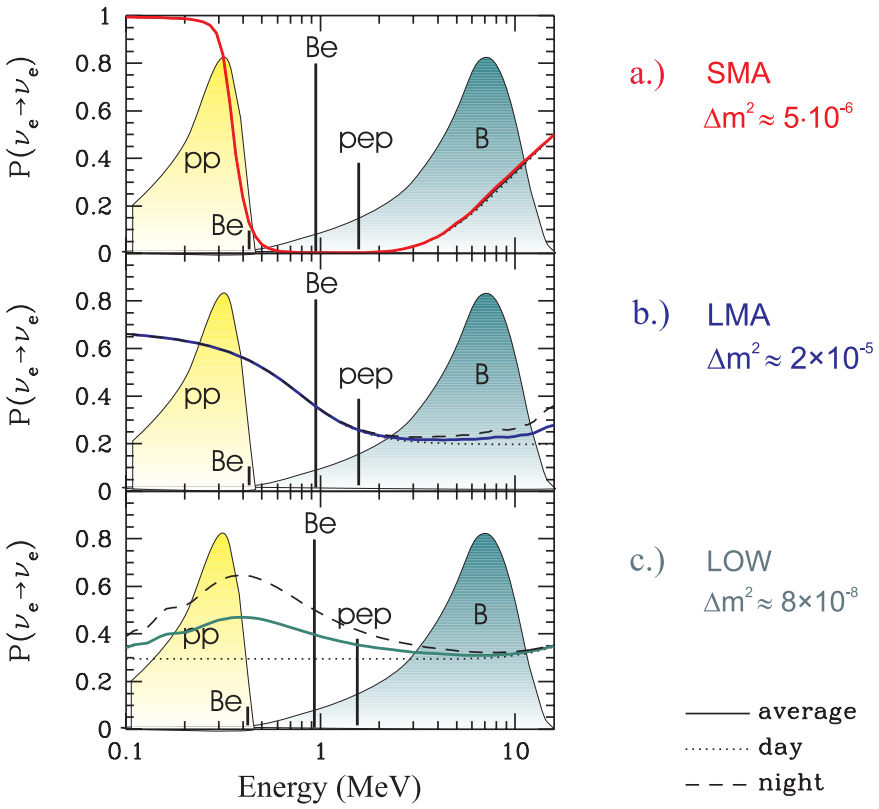

Figure 2.3: Energy dependent survival probabilities of electron neutrinos for the different MSW scenarios. The time averaged probability is shown in addition to the separate probabilities for day and night hours. Only for the LOW solution there is a significant day-night effect for the ^{7}Be neutrinos.

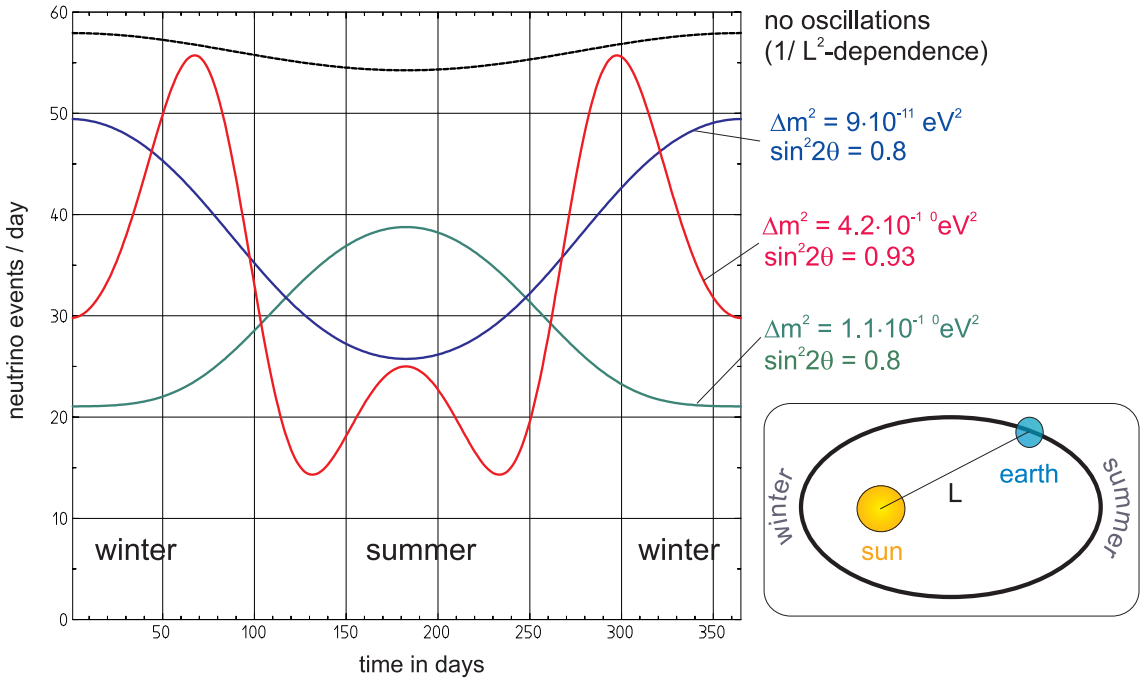

Figure 2.4: Test of vacuum oscillations with BOREXINO. The annual variation of the signal rate is shown for the case of no oscillations (variation due to the eccentricity of the earth's orbit) and for three different values of the parameters $\Delta m^2,\ \sin^2 2\theta$. Taken from [Hag00a].

Physics Beyond Solar Neutrinos

In addition to the main goal of BOREXINO, i.e. to measure solar neutrinos, there are also some further purposes of the detector:

- BOREXINO is an excellent detector of electron antineutrinos via the inverse decay of the proton. This is due to the delayed coincidence between the initial positron signal and the delayed 2.2 MeV neutron-proton capture gamma ray, following an interaction.

$$\bar{\nu}_e + p \rightarrow e^+ + n$$

$$n + p \rightarrow d + 2.2\,\mathrm{MeV}\gamma$$

  The threshold antineutrino energy is 1.8 MeV and the lifetime of the neutron in the scintillator is about 250 μs. This may be useful for setting limits on the flux of antineutrinos from the sun, and for detecting antineutrinos from other sources (see below).

- The BOREXINO detector is sensitive to neutrino bursts from type II supernovae in our galaxy. For a supernova at the center of our galaxy (10 kpc), over 100 neutrinos will

be detected in 300 tons of scintillator [Ali99]. This will be mainly due to CC scattering of electron antineutrinos on protons $\mathrm{p}(\bar{\nu}_\mathrm{e}, \mathrm{e}^+)\mathrm{n}$ (threshold 1.8 MeV), with an additional contribution from NC scattering of neutrinos on carbon $^{12}\mathrm{C}(\nu_\mathrm{x}, \nu_\mathrm{x})^{12}\mathrm{C}^\star$ (threshold 15.1 MeV). The potential of the BOREXINO detector for Supernova neutrino detection is discussed in more detail in [Cad00].

- The uranium and thorium content in the earth's crust can be determined by measuring the antineutrinos from their decay chains via inverse beta decay $\mathrm{p}(\bar{\nu}_\mathrm{e}, \mathrm{e}^+)\mathrm{n}$ (threshold 1.8 MeV). This will give important geophysical information on the heat generation inside the earth [Rag98]. The estimated geophysical antineutrino event rate in BOREXINO is 10 events per year.

- Nuclear power reactors are strong sources of electron antineutrinos. By measuring the rate of antineutrinos from the nuclear power plants in Europe it is possible to perform a long-baseline neutrino oscillation search to probe the LMA solution of the MSW effect [Sch99b]. The nuclear reactors which dominate the flux are at a distance of ~ 800 km to Gran Sasso, as Italy itself has no nuclear power reactors. Since the distances to the reactors are known, and the fuel composition and operating cycle of the reactors can also be known very well, the antineutrino event rates and the positron spectrum in BOREXINO can be calculated with an uncertainty less than 3 %. The expected reactor antineutrino event rate in 300 tons of scintillator is ~ 30 events per year. For the LMA solution the neutrino flux would be suppressed by $\sim 50\,\%$. The expected background due to accidental coincidences is less than 1 event per year.

- The magnetic moment of the electron neutrino can be determined by using a strong artificial neutrino source, e.g. ^{51}Cr or ^{90}Sr, that allows one to measure the shape of the neutrino energy spectrum [Ian98, Ian99a, Ian99b]. The source will be placed in a tunnel directly below the BOREXINO tank.

- It is also possible to load the scintillator with a double beta unstable isotope, e.g. ^{136}Xe, and search for neutrinoless double beta decay [Cac00, Bel01], which is allowed only if the neutrino is a massive Majorana particle. A different approach uses scintillating crystals doped with the double beta instable isotope, namely $^{116}\mathrm{CdWO}_4$, which would be placed inside the scintillator. In this case, the liquid scintillator would serve only as a veto detector [Bel00]. The limit on $T_{1/2}(0\nu2\beta)$ reachable with 65 kg of $^{116}\mathrm{CdWO}_4$ crystals in the CTF is $\sim 10^{26}$ a, corresponding to $m_\nu \leq 0.06$ eV. With 1000 kg $^{116}\mathrm{CdWO}_4$ in BOREXINO a limit for $m_\nu \leq 0.02$ eV could be reached.

2.2 The Detection Principle

The neutrino detection in BOREXINO is based on neutrino-electron scattering using the well-known technique of liquid scintillation spectroscopy. The Feynman diagram of the process of neutrino-electron scattering was shown in fig. 1.3. Solar neutrinos scattering off the electrons in the scintillator will result in a recoil electron which can be detected via scintillation light. The cross section for this pure leptonic reaction can be calculated using the standard theory of electroweak interactions [t'H71]:

$$\frac{d\sigma_\nu}{dT} = \sigma_e \left(g_L^2 - g_R^2 \left(1 - \frac{T}{E_\nu} \right)^2 - g_L g_R \left(\frac{T}{E_\nu} \right)^2 \right),$$

where: T = kinetic energy of the scattered electron

E_ν = energy of the incoming neutrino

$\sigma_e = 2G_F^2 m_e^2 / \pi\hbar^4 \; = \; 88.083 \cdot 10^{-46}$ cm^2

$g_R = \sin^2\theta_W \; = \; 0.2315 \pm 0.0004$

$g_L = (\sin^2\theta_W \pm 1/2)$, + for ν_e, – for $\nu_{\mu,\tau}$.

For a neutrino with a given energy E_ν the maximum kinetic energy of the electron is

$$T_{max} = \frac{2\,E_\nu^2}{m_e\,c^2 + 2\,E_\nu} \; .$$

A monoenergetic neutrino source produces an electron recoil spectrum with a sharp edge and thus a good signature. For the ^{7}Be-neutrinos at 862 keV this edge lies at 665 keV (see fig. 2.5). Even though the recoil spectrum goes from zero to the edge, in practice the optimum ^{7}Be-ν signal window in BOREXINO is from 250 - 800 keV. The lower threshold has to be set due to

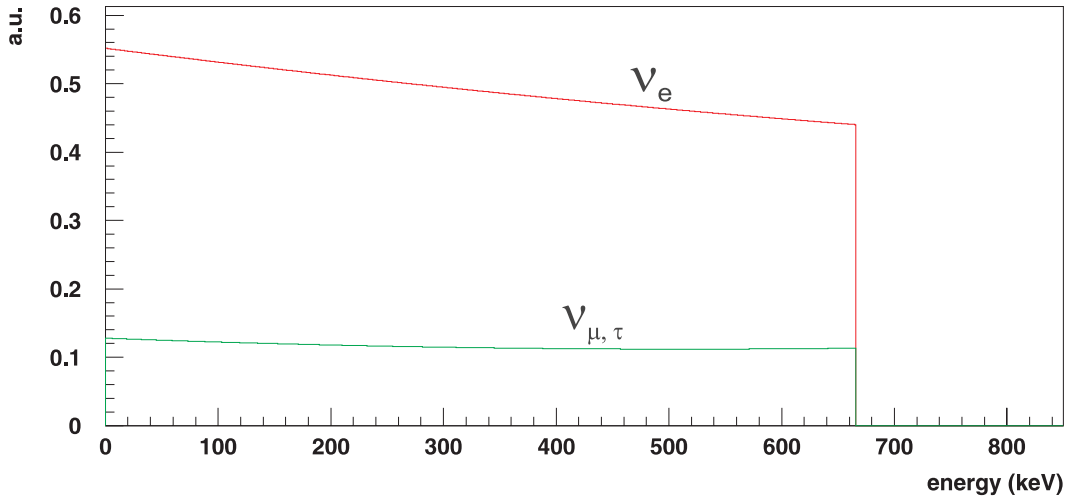

Figure 2.5: The cross section for $\nu - e^-$ scattering for monoenergetic neutrinos with $E_\nu = 862$ keV.

intrinsic background present in the organic scintillator (mainly ^{14}C), the upper limit is chosen to accommodate the finite energy resolution of the detector (about 7 % at 665 keV).

BOREXINO is sensitive to all neutrino flavours, as ν_e, ν_μ and ν_τ can interact via neutral current interactions while only ν_e can additionally interact via charged current interactions. The ratio of the cross-sections for ν_e and $\nu_{\mu,\tau}$ is about 5:1 in the ^{7}Be-ν signal window. In principle, the shape of the recoil spectrum is slightly different for ν_e and $\nu_{\mu,\tau}$, but the difference is probably too small to be distinguishable in practice.

As the scintillation light is emitted isotropically, the directional information of the scattered neutrino is lost and no directional cuts on the neutrino source can be applied. Since the experimental signature is simply a few hundred keV energy deposition in the scintillator, the requirements on the radiopurity of the detector components, especially the scintillator, are very high. The different sources of background and their suppression will be discussed in detail in section 2.4.

Solar neutrinos from other branches of the pp-cycle also contribute to the count rate in the ^{7}Be neutrino window (250 - 800 keV). These are summarized in table 2.1. With a threshold energy of 250 keV for the recoil electron, the lowest energy for neutrinos that can be be detected is 410 keV.

neutrino branch	SSM	LMA	SMA	LOW
pp	1.3	1.0	0.6	0.6
^{7}Be	45.7	26.0	9.7	25.1
pep	2.0	1.0	0.4	1.0
^{13}N	4.2	2.3	0.9	2.3
^{15}O	5.5	2.8	1.1	2.8
^{17}F	0.07	0.03	0.01	0.03
^{8}B	0.01	0.04	0.05	0.05
Sum	58.78	33.17	12.76	31.78

Table 2.1: Expected signal rates (counts per day in 100 tons of scintillator in the energy range from 250 - 800 keV) in BOREXINO from neutrinos of the individual branches for different oscillation scenarios.

2.3 Detector Design

2.3.1 The Main Detector

The BOREXINO detector is being constructed in hall C of the Gran Sasso underground laboratory (LNGS) in Italy. The laboratory is shielded by an overburden of 3600 mwe which leads to a suppression of the cosmic muon flux by a factor of 10^6, down to a value of $1.1\,\mathrm{m}^{-2}\mathrm{h}^{-1}$.

The detector is designed in such a way as to reduce the external gamma ray background in the central fiducial volume to a level well below the expected solar neutrino signal. A detailed description of the BOREXINO detector can be found in [Ali01]. A sketch of the detector is shown in fig. 2.6.

The active part of the detector is an unsegmented volume of 300 tons of liquid scintillator, contained in a thin (0.1 mm) spherical nylon vessel of diameter 8.5 m (Inner Vessel). The scintillator consists of the solvent pseudocumene (PC, 1,2,4 trimethylbenzene) with 1.5 g/l PPO (3,5 diphenyloxazole) added as fluor.

The scintillation light is observed by 2200 8" diameter photomultiplier tubes (PMTs) mounted on the inside surface of a stainless steel sphere with a diameter of 13.7 m. 1800 PMTs are equipped with light concentrators for an efficient collection of the scintillation light from the Inner Vessel. Signals from the 400 remaining PMTs without concentrators will be used for distinguishing muon tracks producing Cerenkov light in the buffer region from events inside the scintillator. The three dimensional arrangement of the photomultipliers allows the position of the neutrino interactions within the detector volume to be reconstructed using the timing information of the triggered PMTs. Thus, a fiducial volume of 100 tons of scintillator (radius ~ 3 m) can be defined by software cuts to reduce the external background.

The volume between the Inner Vessel and the stainless steel sphere is filled with $1000\,\mathrm{m}^3$ of a buffer liquid which serves as shielding against radioactive background from the outer detector parts. This buffer liquid has to fulfill several requirements: it should be optically transparent to the fluorescence emission of PPO (i.e. it should not absorb the scintillation light from the active scintillator volume), and it should not emit fluorescence light itself, as this would lead to very high counting rates mainly due to the background from the PMTs. Ideally, the refractive index of the buffer should match that of the scintillator. The density of the buffer liquid should be very close to the density of the scintillator to minimize the buoyancy-induced stress on the thin nylon vessel (thickness only 0.1 mm). The buffer liquid was chosen to be pseudocumene with the addition of 5 g/l DMP (dimethylphthalate) as a quencher to suppress the fluorescence in the buffer PC by a factor of 20 [Che99]. A second nylon barrier with a diameter of 10.5 m should prevent the ^{222}Rn atoms emanating from the steel, PMTs and concentrators from getting close to the active scintillator volume.

The external steel tank with a height of 17 m and 18 m diameter filled with deionized water provides a final shield against gamma rays and neutrons from the surrounding rocks. The thickness of the water buffer is 2 m, except at the bottom where it is only 1 m. Steel plates under the floor of the tank provide the equivalent of 1 m of water shielding. 200 phototubes

mounted on the outer surface of the stainless steel sphere facing outwards detect the Cerenkov light produced by muons intersecting the water buffer. The collection of the Cerenkov light is enhanced by reflecting sheets of Tyvek film that cover all surfaces of the external tank and the sphere. The design of the muon veto system is described in [Obe98].

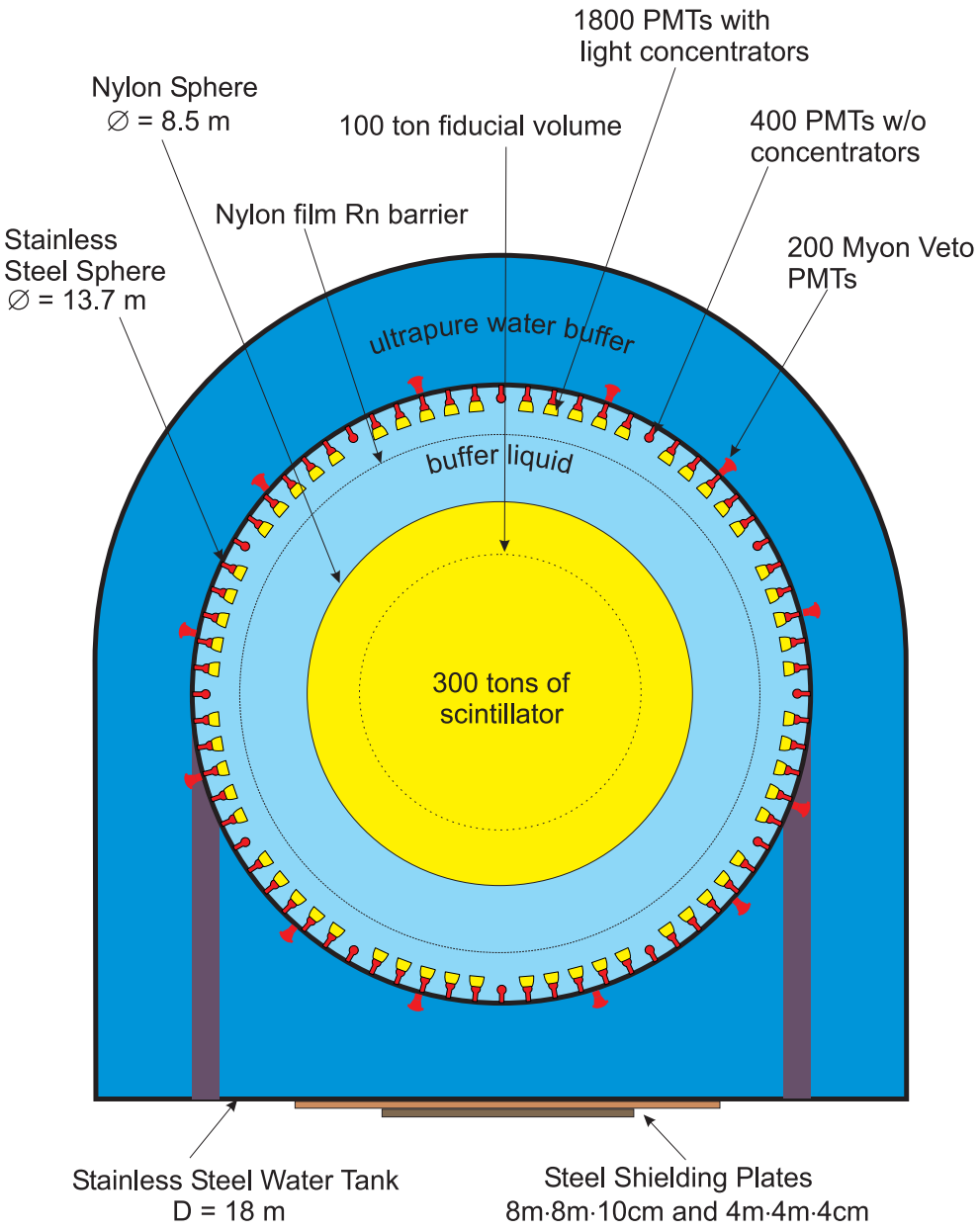

Figure 2.6: Sketch of the BOREXINO detector.

2.3.2 Ancillary Systems

Scintillator Purification and Fluid Handling System

The system to store, handle and purify the 300 tons of PC scintillator and 1000 tons of PC buffer consists of a storage area for the scintillator and the concentrated fluor and quencher solutions, several purification systems, and detector filling systems for BOREXINO and the Counting Test Facility (CTF) (see fig. 2.7).

The purification system is composed of five separate units to apply different purification methods to the scintillator: sub-micron filtration to remove dust particles, water extraction to remove ionizable elements like metals, vacuum distillation to remove low volatility contaminants like dust particles and degraded solvent molecules, nitrogen stripping to remove gaseous impurities (^{222}Rn, ^{85}Kr) and water dissolved in the scintillator, and solid column purification to remove polar impurities. The method of column purification will be described in more detail in chapter 6. A complete description of the purification system can be found in [Ben98, Sch99c].

The purification plants are designed to carry out the purification prior to and during the filling operations. Continuous on-line purification of the scintillator as a whole is provided, if necessary, though the hope is that this procedure will not be required in BOREXINO. The PC used for the scintillator will be delivered well in advance of the filling operation. It will be tested in

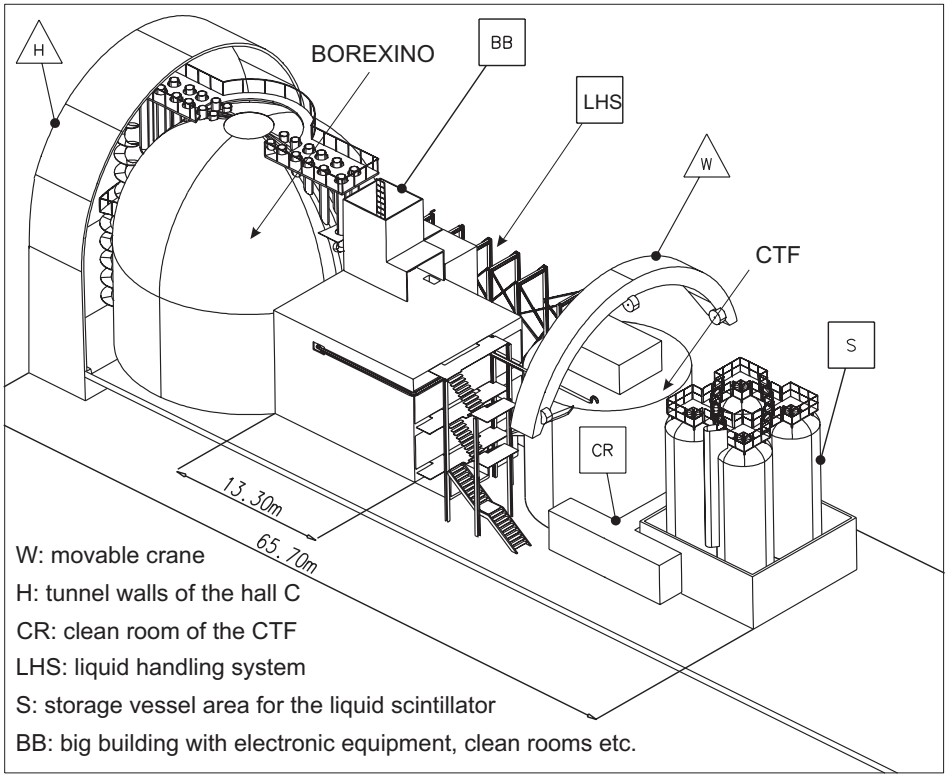

Figure 2.7: Layout of the BOREXINO installations in hall C.

the CTF for radioactive impurities and for optical properties and then stored in three 120 m^3 stainless steel storage vessels until filling of the BOREXINO detector. The raw material for the PC may come from different petroleum sources, which can cause variability in the ^{14}C level. The CTF will be used to test the ^{14}C level to assure that the scintillator is appropriate for BOREXINO. The fluor PPO will be purified off-line as concentrated solution in pseudocumene. The existing CTF purification plant will be modified to process the fluor solution, by a combination of water extraction and distillation. The concentrated fluor solution will be stored in two 4 m^3 vessels until it is added to the solvent during the filling operation to a concentration of 1.5 g/l. The PC used for shielding will be delivered and purified on-line for direct filling of the buffer. The DMP is added on-line to a concentration of 5 g/l .

Water Purification System

Water is a major shielding component for both BOREXINO and the CTF, attenuating the gamma ray flux from the rock surrounding hall C. The design purity goal is about $10^{-13}\,\mathrm{g/g}\,^{238}\mathrm{U}$ in the CTF and about $10^{-11}\,\mathrm{g/g}\,^{238}\mathrm{U}$ in BOREXINO (where additional shielding is provided by the PC buffer). The water purification system consists of a purification system for raw water from the rock, and a recirculation loop to maintain the purity of the water. The water is processed by reverse osmosis, a continuous deionization unit, ultra filtration, an ion exchanger and a final nitrogen stripping to remove ^{222}Rn. For details see [Bal96].

Nitrogen System

Nitrogen gas is used in BOREXINO as a purge gas to remove gaseous contaminations (^{222}Rn, ^{85}Kr) from the scintillator and buffer fluids as well as a buffer gas against recontamination with atmospheric air. Two qualities of gaseous nitrogen with the following Rn-purity are provided by the nitrogen plant: regular nitrogen (RN_2, 1 mBq/m^3) and high purity nitrogen (HPN_2, $10\,\mu\mathrm{Bq/m^3}$). The primary source of the nitrogen will be liquid nitrogen commercially delivered to the LNGS and stored in three 6 m^3 tanks. The regular nitrogen is produced by direct evaporation of the liquid. The high purity nitrogen is obtained from two high purity charcoal traps operated at $-196\,^{\circ}\mathrm{C}$ in line with the liquid flow from the storage tanks to a special evaporator and heater. The high purity line is fabricated of electropolished stainless steel to maintain the Rn-purity level. For a detailed description of the system see [Rau99, Heu00].

Electronics and Data Acquisition

In order to get the information on time, position and energy of an event, the time and pulse height information of each PMT are needed. The basic block diagram of the electronics is shown in fig. 2.8. The PMTs will work mainly in the single photoelectron mode (events in the neutrino window have pulse heights between 50 and 300 photoelectrons), but can also give very large signals due to cosmic rays. The PMT signals arrive at the Front End Board,

which performs the high voltage decoupling, low frequency noise filtering, fast amplification and integration of the total charge for each channel. The resistive sum of each 24 channels is sent to the flash ADC which records the total charge and the pulse shape of these sum signals. The flash ADC will provide an energy measurement in the range from 1 to 8 MeV (detection of ^{8}B neutrinos, Supernova neutrinos ...), where the single PMT chain signals will already be saturated. The fast and the integrated PMT signal are sent from the front end board to a digital readout board. The fast PMT signal is used to fire the discriminator and to give the time information. The integrated PMT signal gives the energy information. It goes into a dual sampling 8 bit ADC which samples the signal just before its rising edge and 80 ns later using the discriminator output signal. The difference between the two measurements is then proportional to the charge collected by the PMT. The data is written into a local FIFO buffer where it is stored temporarily while the system is waiting for a possible trigger. The BOREXINO trigger algorithm is to count the PMTs fired in a 50 ns time window and start the data acquisition if this number is greater than a given threshold. The data acquisition will read data in a time range from 1 μs before the trigger to 4 - 5 μs after the trigger, so that also short delayed coincidences will be registered. A detailed description of the data acquisition system can be found in [Gat99, Gat01].

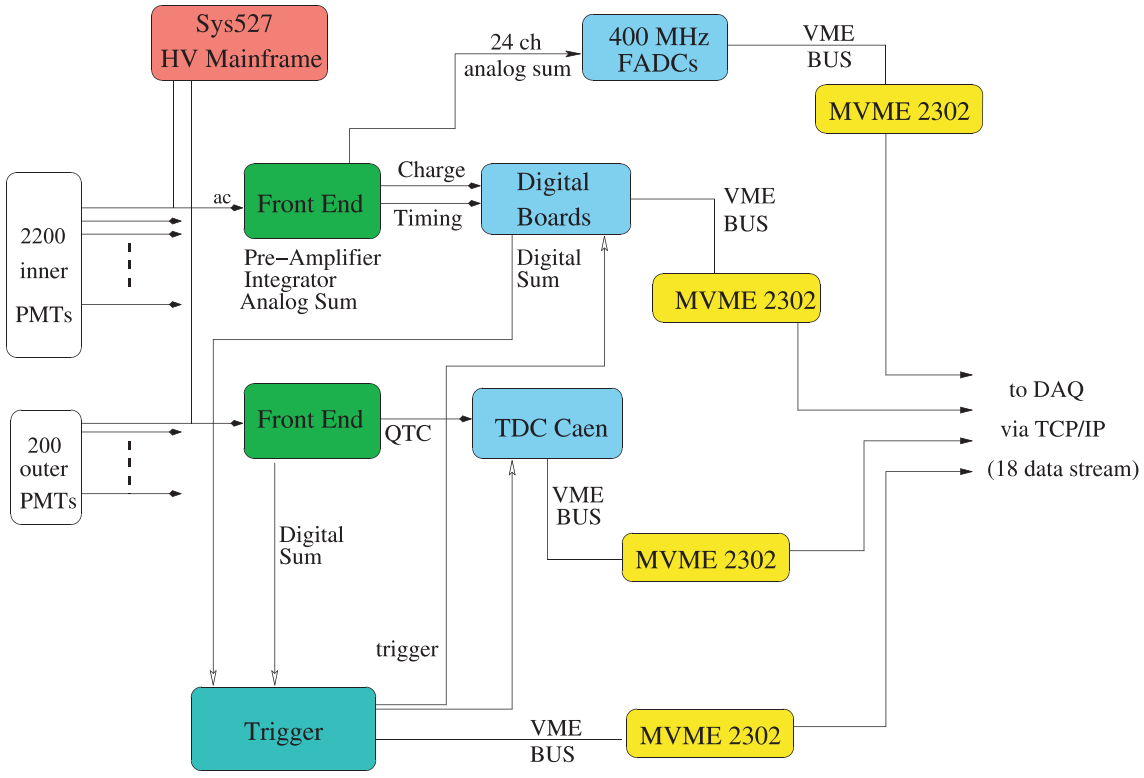

Figure 2.8: Schematic overview of the BOREXINO electronics. Taken from [Pal00].

Calibration and Monitoring

The calibration program for BOREXINO covers the energy and time response of the detector using built-in systems, active tags of trace impurities in the scintillator, and the insertion of localized radioactive sources [Man00]:

- The pulse timing and gain of each phototube is calibrated by a laser system. Photons from a laser are carried by thin optical fibers connected to each light concentrator, with a light yield corresponding to single photoelectron signals.

- ^{14}C present in the scintillator can be used to monitor the stability of the energy response of the detector in the low energy range. Also the 2.2 MeV γ ray emitted after neutron capture on a proton can be used for an energy calibration. Neutrons are created in the scintillator by cosmic ray muons at a rate of about 0.3 per day and ton (experimentally determined in the CTF), and are captured by protons in the scintillator after a lifetime of $\sim 250\,\mu$s.

- Optical sources will be used to monitor the scintillator and buffer transparency. Laser light with several different wavelengths will be carried into different regions of the detector by optical fibers.

- As the energy response of the detector will be position dependent, a calibration with a point-like source at several known positions in the detector is needed. The plan is to insert a small encapsulated source that can be moved to known positions inside the scintillator.

- An unambiguous, straightforward test of the overall detector response will be provided by a calibration with a ^{51}Cr source with an activity in the MegaCurie range. It emits neutrinos of 740 keV energy, which is close to the ^{7}Be neutrino energy. The source would be placed in an existing tunnel under the detector.

2.4 Background

2.4.1 Internal Background

Background from radioactive contaminants intrinsic in the organic liquid scintillator is classified as internal background. Organic liquid scintillator is likely to have very low levels of intrinsic radioactivity for two reasons:

1. Metal impurities (such as ^{238}U, ^{232}Th, ^{40}K) which typically exist in ionic form, are insoluble in non-polar organic solvents.
2. The liquid scintillator is synthesized from petroleum which has resided deep underground for millions of years. As a consequence, some activities (e.g. ^{14}C) will have decayed away and new cosmogenic activity is kept to a minimum.

Table 2.2 gives the allowed concentrations of several potential background elements in the scintillator, which were derived by Monte-Carlo simulations. The most important isotopes dangerous for BOREXINO are shortly reviewed here:

- **^{14}C** is continuously produced in the atmosphere by cosmic rays via the reaction $^{14}\mathrm{N(n,p)}^{14}\mathrm{C}$. It decays by beta emission with an endpoint of 156 keV and a half life of 5730 a. In living organic matter the ratio $^{14}\mathrm{C}/^{12}\mathrm{C}$ is about 10^{-12}. The petrochemical origin of the carbon in the scintillator should guarantee sufficient age for the ^{14}C to have decayed away. However, underground production through (α,n) and (n,p) reactions on carbon results in a finite level of ^{14}C that varies depending on the petroleum source. As carbon is part of the molecular structure of the scintillator itself, it cannot be removed by chemical purification methods. If the ^{14}C level in the scintillator is too high, the only solution is to obtain scintillator from a different petroleum source. At a concentration of $^{14}\mathrm{C}/^{12}\mathrm{C} = 10^{-18}$ there are about 70 decays per second in 300 tons of scintillator. The background in the neutrino window due to the poor energy resolution at low energies and pile-up events is still less than 1 event per day.
- **^{238}U** decays to ^{206}Pb by 8 α and 6 β decays. Assuming secular equilibrium in the decay chain, the tolerable level of ^{238}U in the scintillator is $< 10^{-16}$ g/g. The secular equilibrium might be broken at the long-lived ^{234}U, ^{230}Th, ^{226}Ra or ^{210}Pb isotopes. A special concern is ^{222}Rn, which is continuously produced by ^{238}U contained in the detector materials, and as a noble gas with a half life of 3.8 days can readily diffuse into the scintillator. Another problem is the long-lived radon daughter ^{210}Pb, which will be plated on the surfaces that were exposed to air during the detector construction, and which decays with a half life of 22.3 a.
- **^{232}Th** decays to ^{208}Pb by 6 α and 4 β decays. The tolerable concentration for ^{232}Th in the scintillator is about 10^{-16} g/g. The secular equilibrium may be broken at the long-lived ^{228}Ra or ^{228}Th isotope. The radon isotope ^{220}Rn is not a problem, as it has only a short half life (55.6 s) and decays via short-lived daughters to the stable isotope ^{208}Pb.

- Potassium is ubiquitous with a concentration of 2.4 % in the earth's crust. Naturally occurring **^{40}K** has an isotopic abundance of 1.2×10^{-4} with a half life of 1.3×10^{9} years; 89 % of its decays proceed by beta emission with an endpoint of 1.3 MeV and 11 % decay by electron capture with the emission of a 1.46 MeV gamma. The tolerable limit for BOREXINO is 10^{-14} g/g (K_{nat}) in the scintillator. The potassium content in the fluor PPO as delivered was measured by NAA to be $2 \cdot 10^{-7}$ g/g [Gol97]. By water extraction of a concentrated solution (100 g/l PPO in PC) this could be reduced several orders of magnitude, so that the final potassium concentration in the CTF scintillator (1.5 g/l PPO in PC) was below the sensitivity limit of both the CTF ($< 2 \cdot 10^{-11}$ g/g) and NAA ($< 4 \cdot 10^{-12}$ g/g). The purity requirement is thus not directly confirmed, but it is expected to be met because of the high efficiency of the water extraction.

- **^{7}Be** can be formed by proton and neutron reactions on ^{12}C from cosmic radiation. It decays by electron capture with a half life of 53 days, with a 10 %-branch emitting a 478 keV gamma. In equilibrium at the earth's surface ^{7}Be gammas are expected to give a count rate of 2700 per day and ton of scintillator [Vog96]. This rate can be reduced by bringing the scintillator underground directly after distillation, before the equilibrium rate of ^{7}Be is reached (after one day of surface exposure the expected gamma rate is ~ 30 per day and ton), and storing the scintillator underground for a sufficient period of time to allow the ^{7}Be to decay, or by removing the ^{7}Be through purification. At a small rate, ^{7}Be will also be produced on site by cosmic ray muons (see paragraph 2.4.3).

Though there is no clear signature for a single neutrino event, there are several methods to discriminate certain classes of background events:

- **correlated events**: the method consists of tagging delayed coincidences in the U and Th decay chains (^{214}Bi-^{214}Po, β-α with $t_{1/2} = 164\,\mu$s; ^{212}Bi-^{212}Po, β-α with $t_{1/2} =$

Isotope	Abundance	$T_{1/2}$ [a]	Concentration [g/g]
^{113}Cd	12.2 %	$9.3 \cdot 10^{15}$	$2.8 \cdot 10^{-9}$
^{115}In	95.8 %	$4.4 \cdot 10^{14}$	$2.4 \cdot 10^{-12}$
^{40}K	0.01 %	$1.3 \cdot 10^{9}$	$7.8 \cdot 10^{-15}$
^{138}La	0.09 %	$1.1 \cdot 10^{11}$	$1.2 \cdot 10^{-12}$
^{176}Lu	2.59 %	$3.8 \cdot 10^{10}$	$3.7 \cdot 10^{-15}$
^{87}Rb	27.8 %	$4.7 \cdot 10^{10}$	$3.2 \cdot 10^{-14}$
^{232}Th	100 %	$1.4 \cdot 10^{10}$	$2.4 \cdot 10^{-16}$
^{238}U	99.3 %	$4.5 \cdot 10^{9}$	$1.0 \cdot 10^{-17}$

Table 2.2: Trace element concentrations at an equal amount of 1 event/(100t day) to the background rate in BOREXINO in the energy range from 250 - 800 keV, after application of all cuts (correlated events, α/β discrimination, statistical subtraction).

300 ns; ^{220}Rn-^{216}Po, α-α with $t_{1/2} = 0.15$ s), which can be identified using a cut on the α energy and the coincidence time.

- **pulse-shape-discrimination**: in organic scintillators, the pulse shape is different for α and β events, which can be used for identifying and rejecting α internal background events. A detailed description of this method will be given in chap. 5.

- **statistical subtraction**: after tagging the delayed coincidences in the uran and thorium chain, also the activity of the corresponding parent isotope is known, if they are in equilibrium. This is a valid assumption only for short-lived, non-mobile isotopes. In the ^{238}U chain, this can be done back to the mobile ^{222}Rn isotope ($t_{1/2} = 3.8$ d); in the ^{232}Th chain back to ^{228}Th ($t_{1/2} = 1.9$ a). When the activity of the parent isotope is known, then the spectrum of all following decays can be subtracted. This subtraction cannot be done event by event, but only after a sufficient statistics of correlated events has been accumulated.

2.4.2 External Background

Any γ-ray emitting radioactivity outside the scintillator contributes to the external background. Sources to be considered are the nylon vessel, the buffer liquid, the PMTs and concentrators,

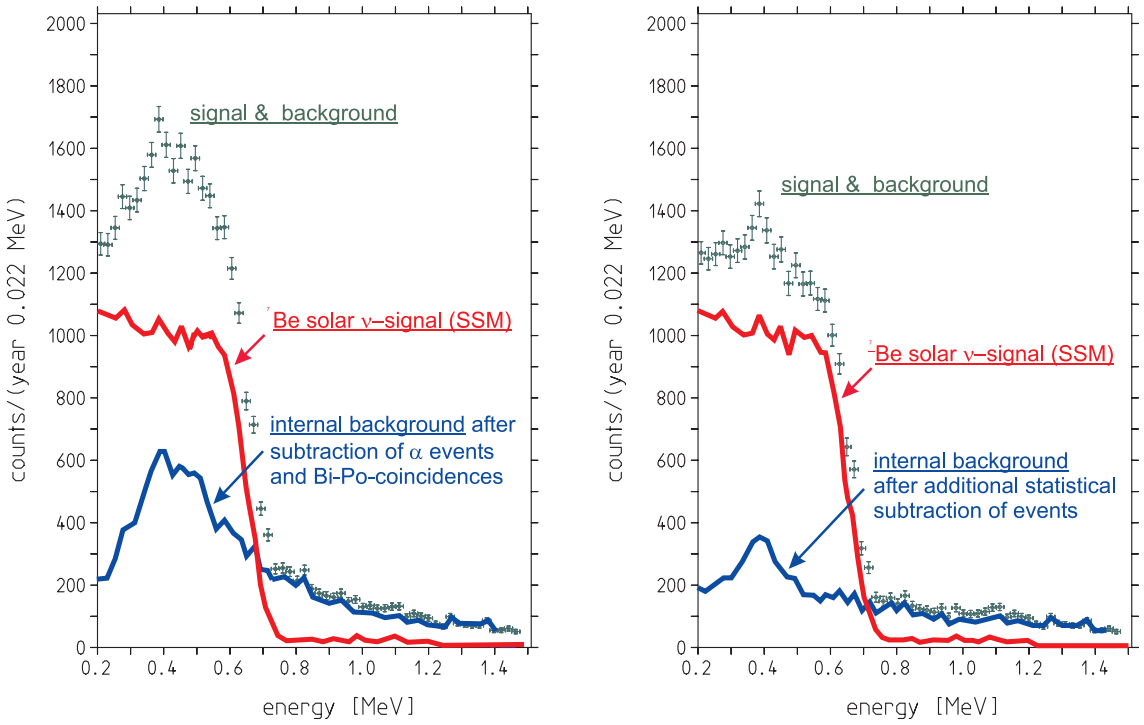

Figure 2.9: Simulation of SSM neutrino signal plus the internal background spectrum in BOREXINO after the application of the individual cuts.

the steel sphere, the outer steel tank and the surrounding rocks. The most dangerous isotopes are the ones emitting the highest energy γ-rays, which are ^{208}Tl (2.6 MeV γ) in the thorium chain, ^{214}Bi in the uranium chain (1.7 MeV γ), and ^{40}K (1.46 MeV γ). A careful selection of the materials used for the detector components was necessary to reduce the external background contribution. Systematic measurements of the gamma activity and the ^{222}Rn emanation were done for all components (see [Arp01, Rau00, Gol98, Rie99]).

The radial distribution of the external background events drops rapidly towards the center, so that this background can be suppressed very efficiently with a radial cut (see fig. 2.10). The remaining γ-rays which produce a signal inside the fiducial volume, have to penetrate at least 1 m of scintillator first, so their spectrum is shifted towards higher energies; thus they won't contribute to the background in the neutrino window (250 - 800 keV). The background requirements for the outer detector components (see table 2.3) were calculated for a fiducial volume of 3 m radius (100 tons of active target), but a lower external background would allow to set a larger fiducial volume, increasing the active target mass. It has to be noted, that for the definition of the fiducial volume and the suppression of external background events the understanding of the position reconstruction of the scintillation events is crucial, as the number of background events rises very steeply with increasing radius. The total number of external background events with energies in the neutrino window is about 40 times higher than the expected SSM ^{7}Be neutrino signal, and about 180 times higher than the expected SMA signal. If only 1 % of the external background events is not correctly identified by the reconstruction code, but shifted towards the center by a systematic effect, then the background in the fiducial

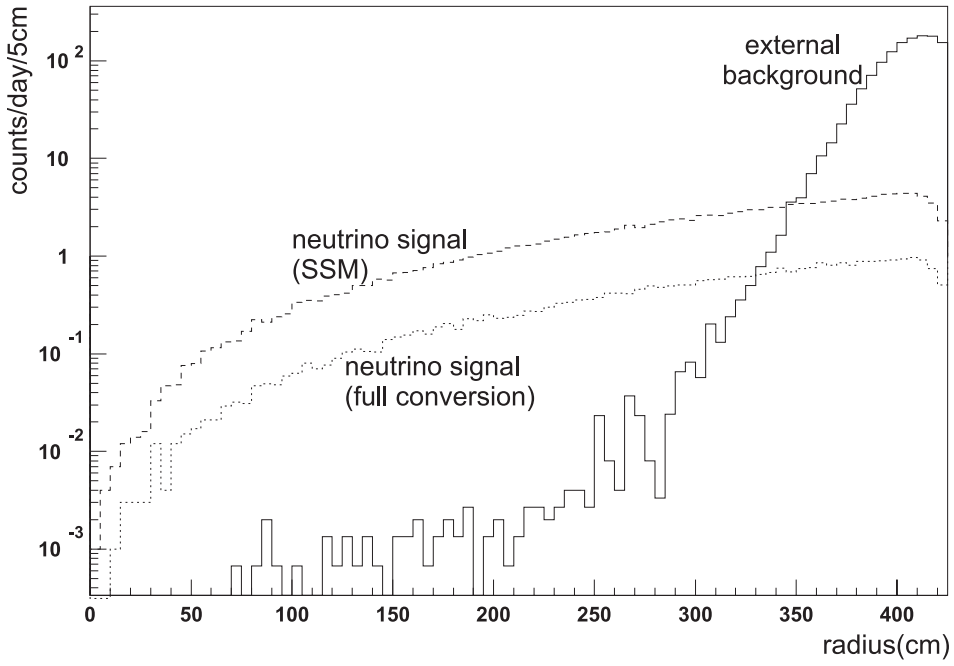

Figure 2.10: Simulated radial distribution of external background and neutrino events in the energy window 250 - 800 keV. An energy dependent position resolution is included $\sigma_x \sim 5.4\,\mathrm{cm}/\sqrt{\mathrm{E(MeV)}}$.

volume would be of the same order or even higher than the expected neutrino signal. It is therefore important to exclude systematic errors of the position reconstruction well below the percent level.

Material	^{238}U (g/g)	^{232}Th (g/g)	^{40}K (g/g)
scintillator	10^{-16}	10^{-16}	10^{-14}
nylon vessel	10^{-10}	10^{-10}	10^{-7}
buffer liquid	10^{-13}	10^{-13}	10^{-10}
PMTs	10^{-7}	10^{-7}	10^{-4}
stainless steel tank	10^{-8}	10^{-8}	10^{-5}

Table 2.3: Background requirements for the BOREXINO detector components.

2.4.3 Background from Cosmic Ray Events

The flux of cosmic rays is dramatically suppressed by locating the detector underground. For this reason the detector is installed in the Gran Sasso underground laboratory, with an overburden of about 1400 m of rocks which provides a shielding of about 3600 mwe and suppresses the cosmic ray flux by a factor of 10^6. The remaining flux of about $1.1\,\mathrm{m}^{-2}\mathrm{h}^{-1}$ is composed essentially of ultrarelativistic muons with energies of several hundred GeV.

A muon passing through the scintillator will produce a large amount of scintillation photons and can hence easily be identified. A fraction of muons, though, cross only the buffer without entering the scintillator. They could produce few enough photons (by Cerenkov light or scintillation of the PC in the buffer) to be misidentified as a low energy electron. These muons will be identified over the Cerenkov photons they produce in the outer water tank, which will be detected by 200 outward looking PMTs mounted on the outside of the Stainless Steel Sphere.

Another source of background are short-lived radioactive nuclides produced on-site by muon inelastic interactions in the scintillator (see table 2.4). Most of the isotopes have half-lives in the sub-seconds scale. With the identification of the muon by the outer Cerenkov detector, it is possible to discard these activities with a moderate loss of measuring time by imposing a veto cut subsequent to a muon signal in the off-line analysis. However, this is not the case for ^{11}Be (β^-, $E_{max} = 11.5$ MeV, $t_{1/2} = 13.80$ s) and ^{7}Be ($t_{1/2} = 53.3$ d, EC, 10 % γ with 478 keV). From the measurement of the cross sections for the production of these isotopes one can expect in BOREXINO a background of less than 1 event per day in the ^{7}Be neutrino window (250 - 800 keV) in 100 t of scintillator [Hag00b]. The large background contribution of ^{11}C in the energy region from 0.8 - 1.4 MeV however jeopardizes the detection of the solar pep-neutrinos, with an expected event rate of only 1.5 counts/(day 100 t) according to the SSM.

	Isotopes	$T_{1/2}$	E_{max} (MeV)	counts/day 100t 250 - 800 keV	counts/day 100t 0.8 -1.4 MeV
β^-	^{12}B	0.02 sec	13.4		
	^{11}Be	13.81 sec	11.5	$< 4 \cdot 10^{-4}$	$< 1 \cdot 10^{-4}$
	^{11}Li	0.09 sec	20.8		
	^{9}Li	0.18 sec	13.6	$< 7 \cdot 10^{-4}$	$< 1 \cdot 10^{-3}$
	^{8}Li	0.84 sec	16.0	$2.5 \cdot 10^{-4}$	$8.0 \cdot 10^{-4}$
	^{8}He	0.12 sec	10.6	$< 7 \cdot 10^{-4}$	$< 1 \cdot 10^{-3}$
	^{6}He	0.81 sec	3.5	0.04	0.07
β^+	^{11}C	20.39 min	0.96	0	7.4
	^{10}C	19.26 sec	1.9 ($+0.72\gamma$)	0	0
	^{9}C	0.13 sec	16.0	0	0
	^{8}B	0.77 sec	13.7	0	$3.3 \cdot 10^{-5}$
EC	^{7}Be	53.3 days	0.478 (γ, 10 %)	0.34	0

Table 2.4: Radioactive isotopes that can be produced by muons and their secondary shower particles when passing through a scintillator target consisting mainly out of ^{12}C and ^{1}H, and their background contribution in BOREXINO in the ^{7}Be and the pep neutrino window.

3 The Counting Test Facility (CTF) of Borexino

3.1 Motivation

At the end of the last chapter I discussed the extremely high requirements on the radiopurity of the detector components for a successful neutrino detection in BOREXINO. Standard analysis methods, such as mass spectrometry or gamma spectroscopy, are sufficient to check most of the outer detector components on their radiopurity, but the demands on the radiopurity of the scintillator itself are beyond the sensitivity of these other methods, the only exception being the high sensitivity neutron activation analysis (NAA) developed in Munich during the last few years [Gol97, vH99]. To study and check the feasibility of the BOREXINO experiment in terms of radiopurity of the liquid scintillator and the other detector components, a 5 ton-prototype of BOREXINO was constructed in hall C of the Gran Sasso Underground Laboratory, the Counting Test Facility (CTF). The main goals of the CTF were:

- measurement of the ^{238}U and ^{232}Th content of the liquid scintillator with a sensitivity of 10^{-16} g/g;
- measurement of the $^{14}\mathrm{C}/^{12}\mathrm{C}$ ratio at a level of 10^{-18};
- determination of the optical properties of the liquid scintillator;
- radioactivity screening of the construction materials of various detector components;
- test of several purification methods for the liquid scintillator and the shielding water;
- implementation of methods for cleaning and controlling dust and air impurities during the detector construction;
- development of analysis methods to discriminate different classes of background events.

^{40}K and ^{7}Be cannot be tested on a level relevant for BOREXINO because the detector is not big enough to provide sufficient shielding from external background.

3.2 Detector Design

The CTF is located in the hall C of the Gran Sasso underground laboratories. Its conceptual design reproduces on a small scale the philosophy of the BOREXINO detector (see fig. 3.1). A detailed description of the detector and its performance can be found in [Ali98a]. The central part of the detector consists of 4.8 m^3 organic liquid scintillator contained within a spherical nylon vessel (2 m diameter, 0.5 mm thick). The scintillation light is detected by 100 PMTs mounted on a spherical support structure (open structure) with a diameter of 7 m. The PMTs are the same 8" Thorn EMI 9351 tubes that will be used in BOREXINO. Light concentrators (57 cm long, 50 cm aperture diameter) are affixed to the PMTs in order to increase the effective area coverage to about 21 %.

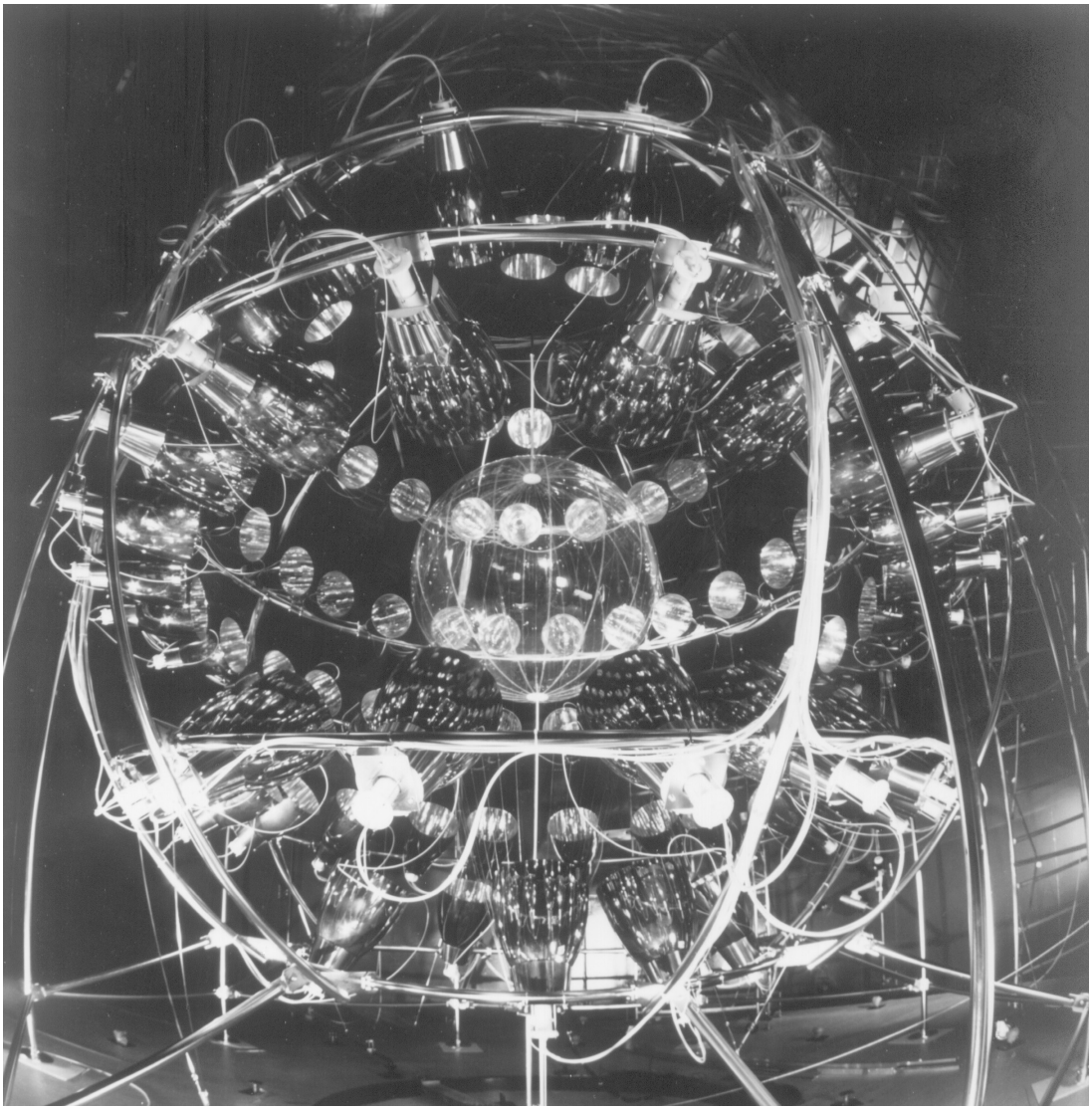

Figure 3.1: View of the CTF detector

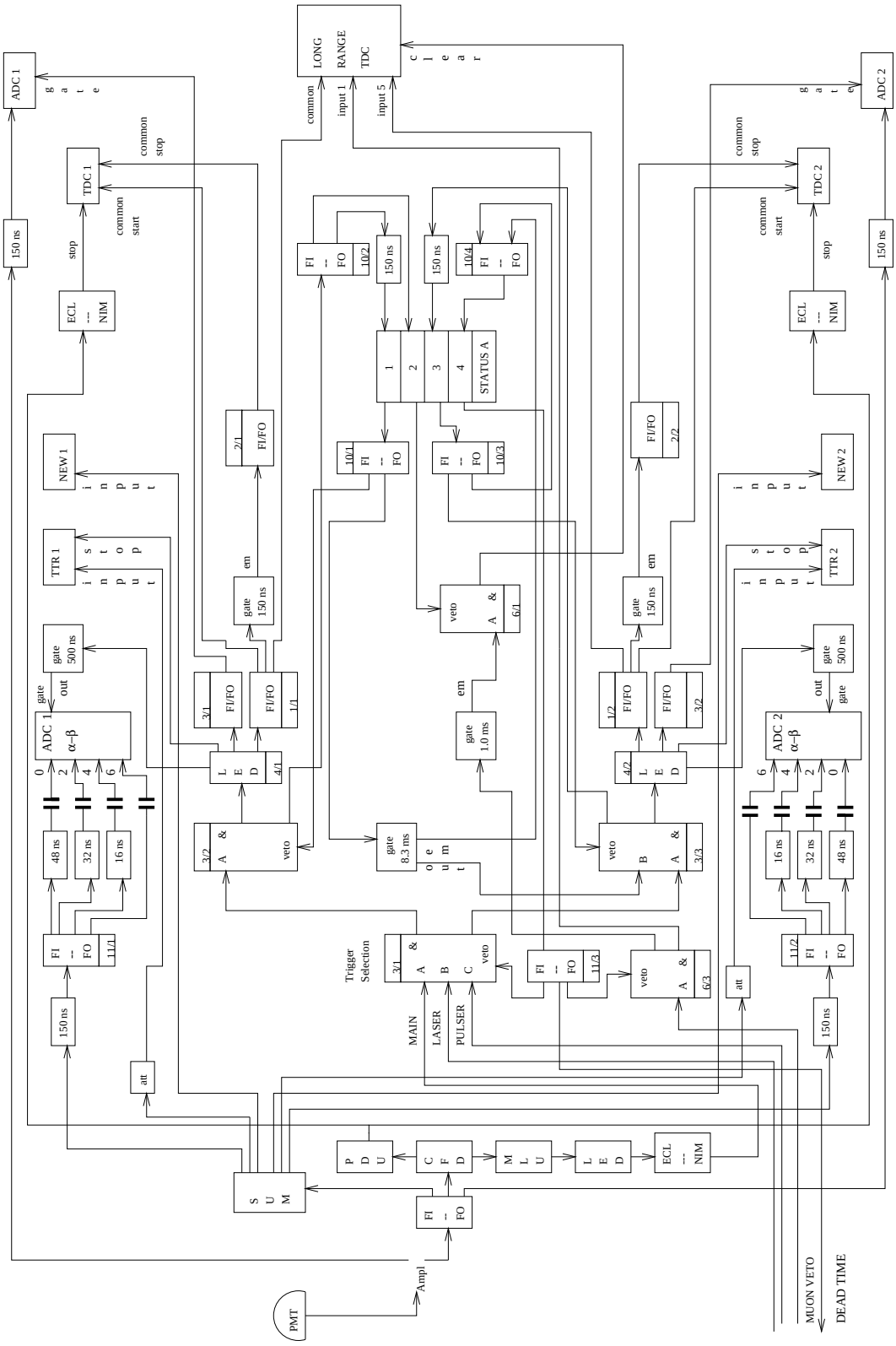

Figure 3.2: Block diagram of read out electronics of the CTF.

All the structure is immersed in 1000 tons of deionized water contained within a carbon steel tank (11 m diameter, 10 m high), whose inside walls are coated with a black epoxy resin in order to minimize light reflections from the tank walls. The water provides shielding from the external γ-ray background coming from the PMTs, the steel, and the surrounding rocks.

Fig. 3.2 shows the data acquisition logic. The 100 photomultiplier outputs are processed in 64 electronic channels, 72 PMTs are fanned together in pairs into 36 channels, and 28 PMTs are read as single channels. Each electronic channel has a time-to-digital-converter (TDC) and an analog-to-digital-converter (ADC). The trigger is provided by a Majority Logic Unit. The trigger condition is set so that a certain number of PMTs (usually 6) must receive a photon within a time window of 30 ns. This trigger condition is necessary because each PMT has a dark noise of approximately 1 kHz. For each event the charge and timing of the hit phototubes are recorded. To avoid missing fast time correlated events, each processing channel is doubled by a second channel to record events coming within a time window of 8 ms after the first event. The delay time is measured with a precision of 1 ns. For longer correlation times, the internal clock of the computer is used (with a resolution of ~ 0.1 s). The PMT analog signals are also summed up to provide the total charge and the charge integrated over the pulse tail (with a delay of 32 ns and 48 ns), to discriminate between alpha and beta events, and to record the pulse shape of each event by a waveform digitizer. The time calibration of the PMT signals is done with a pulsed laser (pulse width 50 ps) with a wavelength of 410 nm, which is coupled to a bunch of 100 optical fibers leading to each PMT. The intensity of the laser signal is attenuated so that each PMTs receives ≤ 1 photoelectron from each laser pulse.

3.3 Results from the CTF1

From March 1995 until August 1996 the scintillator $\mathrm{PC} + \mathrm{PPO}\,(1.5\,\mathrm{g/l})$ was tested in the CTF. With the CTF the scintillator radiopurity was measured at previously unachieved levels. It is the largest nuclear detector ever built with sensitivity down to the sub 100 keV spectral regime; and with a background of 0.03 events $\mathrm{kg}^{-1}\,\mathrm{keV}^{-1}\,\mathrm{yr}^{-1}$ in the 0.25 - 2.5 MeV energy window [Ali98c] it is the detector with the lowest background activity in this regime, even better than detectors searching for neutrino-less double beta decay.

The ^{14}C content in the scintillator was determined by normalizing the CTF low energy spectrum (50 - 150 keV) to the spectral shape expected from the decay of ^{14}C (see fig. 3.3), giving a value of

$$\frac{^{14}\mathrm{C}}{^{12}\mathrm{C}} = (1.94 \pm 0.09)\,10^{-18}\ \text{[Ali98b]}.$$

The concentration of ^{222}Rn and ^{228}Th in the scintillator was determined by tagging the correlated decays of their short-lived daughters $^{214}\mathrm{Bi}-^{214}\mathrm{Po}$ ($\mathrm{t}_{1/2} = 164\,\mu\mathrm{s}$) and $^{212}\mathrm{Bi}-^{212}\mathrm{Po}$ ($\mathrm{t}_{1/2} = 300\,\mathrm{ns}$). Assuming secular equilibrium in the decay chains, this activity can be ex-

pressed in ^{238}U and ^{232}Th equivalents [Ali98c]:

$$1.5\,\mathrm{c/d} \quad {}^{214}\mathrm{Bi} - {}^{214}\mathrm{Po} \quad \Rightarrow \quad \mathrm{c}({}^{238}\mathrm{U}) \quad = (3.5 \pm 1.3) \times 10^{-16}\,\mathrm{g/g}$$

$$0.3\,\mathrm{c/d} \quad {}^{212}\mathrm{Bi} - {}^{212}\mathrm{Po} \quad \Rightarrow \quad \mathrm{c}({}^{232}\mathrm{Th}) = (4.4 \pm 1.4) \times 10^{-16}\,\mathrm{g/g}$$

There were, however, strong indications that the observed ^{214}Bi$-^{214}$Po coincidence rate was not due to the scintillator intrinsic radioactivity, but rather due to the diffusion of ^{222}Rn from the shielding water through the nylon vessel into the scintillator, as the coincidence rate increased with the ^{222}Rn level in the shielding water.

By studying the radial distribution of all the background events, they could be divided into an internal and external contribution. The total internal background with energies in the neutrino window (250 - 800 keV) went down from (470 ± 90) counts/day before purification to (21 ± 47) counts/day after the purification operations (nitrogen sparging, water extraction, distillation) [Ali98c].

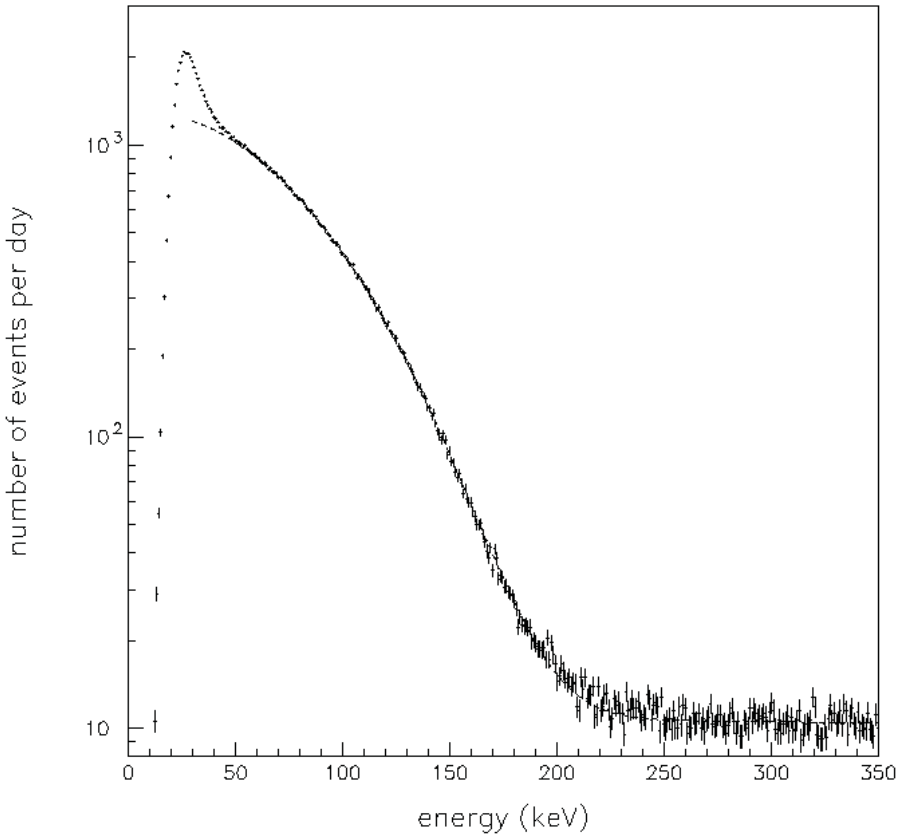

Figure 3.3: Low energy spectrum measured in the CTF, with the fit of a ^{14}C beta spectrum. Taken from [Ali98b].

3.4 The upgraded Counting Test Facility: CTF2

3.4.1 Motivation

The CTF1 has continuously operated from January 1995 to July 1997. At the end the number of PMTs functioning was substantially reduced due to a failure of the sealing of the PMTs. Therefore the Counting Test Facility was refurbished and upgraded during the years 1998 and 1999 and restarted data taking in May 2000.

The CTF2 will be used as a quality control facility for BOREXINO, its main goals are:

- to test a sample of each batch of scintillator as it is delivered for BOREXINO on its ^{14}C content and its radiopurity;
- to test and optimize the BOREXINO liquid handling and purification systems after their installation on site before the final operation in order to guarantee the high purity standards requested.

As a first campaign from June to September 2000 an alternative liquid scintillator for BOREXINO based on phenyl-o-xylylethane (PXE) was tested. The results of this campaign will be reported in chapter 6.

3.4.2 Design Improvements

New PMT Design and Readout

The sealing of the PMTs in the CTF1 revealed several serious structural problems that caused a failure of more than 80 % of them. Therefore, a completely new PMT sealing design was developed for the CTF2. The part of the tube to be protected, i.e. the pins and the voltage divider, are enclosed in a cylindrical stainless steel housing filled with several layers of potting materials (see fig. 3.6). An underwater connector and an underwater cable, the same developed for BOREXINO, allowed the mounting of PMTs and cables to be done in separate steps. Only one cable supplies the high voltage and transmits the signal. The capacitive decoupling of the signal is done in the electronics room. This technique will also be used for BOREXINO.

Homogeneous Distribution of PMTs

The CTF has 100 PMTs to have a photoelectron (pe) yield big enough to measure energies as low as a few keV, but only 64 electronic channels (due to funding reasons). Therefore, 72 PMTs are fanned together in pairs, and only 28 PMTs are single electronic channels. In the CTF1 the distribution was chosen as shown in fig. 3.4, a and b. Having only few electronic channels at the top and bottom ring leads to a spatial resolution that is much worse in the z-direction than in the x and y direction. As could be shown with a Monte-Carlo simulation (MC), the spatial resolution can be improved by putting single channels on the top and bottom ring, and arranging all the PMTs at the equator rings as double channels (see fig. 3.4, c and d). Distributing all the PMTs homogeneously over the rings, improves the homogeneity of the

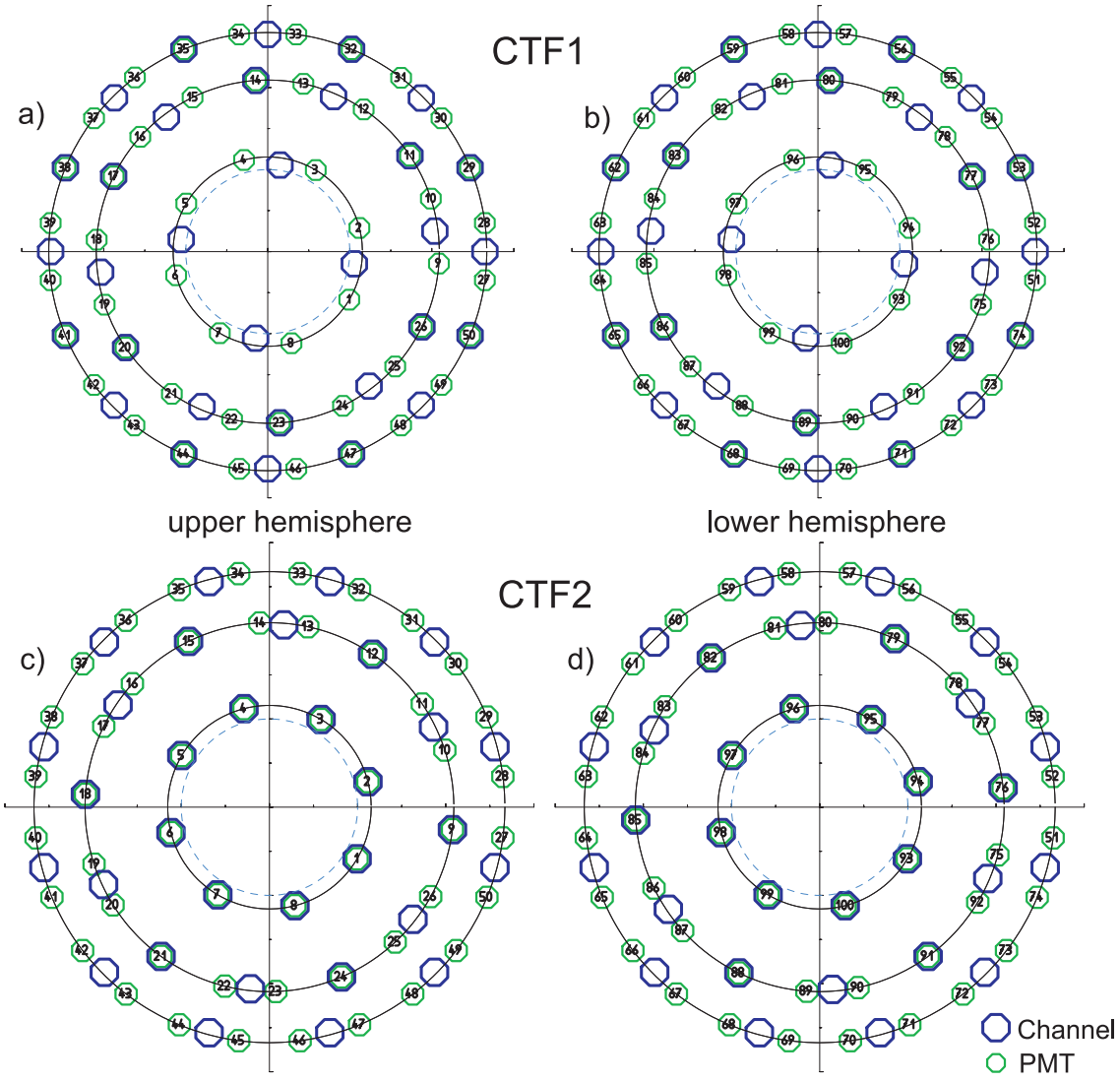

Figure 3.4: Schematic drawing of the distribution of the PMTs and electronic channels over the rings of the support structure.

detector response without deteriorating the spatial resolution (as the relative time difference between neighbouring PMTs is anyway very small). A MC of homogeneously distributed events in the Inner Vessel showed, that the resolution in x and y stays the same for both PMT/channel-distributions, while the resolution in the z-direction improves about 5 % ($\sigma_{x,y} \approx 6.7\,\mathrm{cm}, \sigma_z \approx 7.3\,\mathrm{cm}$ @ 250 pe for the old distribution, and $\sigma_{x,y} \approx 6.7\,\mathrm{cm}, \sigma_z \approx 6.9\,\mathrm{cm}$ @ 250 pe for the new distribution).

Rn Shroud

Radon diffusion through the nylon membrane was observed in the CTF1 and studied in laboratory measurements [Woj00]. In order to reduce the background induced by ^{222}Rn present in the shielding water (originating from emanation off the tank walls, PMTs and other detector components or the shielding water itself) in the CTF2 a second nylon vessel (diameter 4 m) was introduced as Radon barrier (see fig. 3.5).

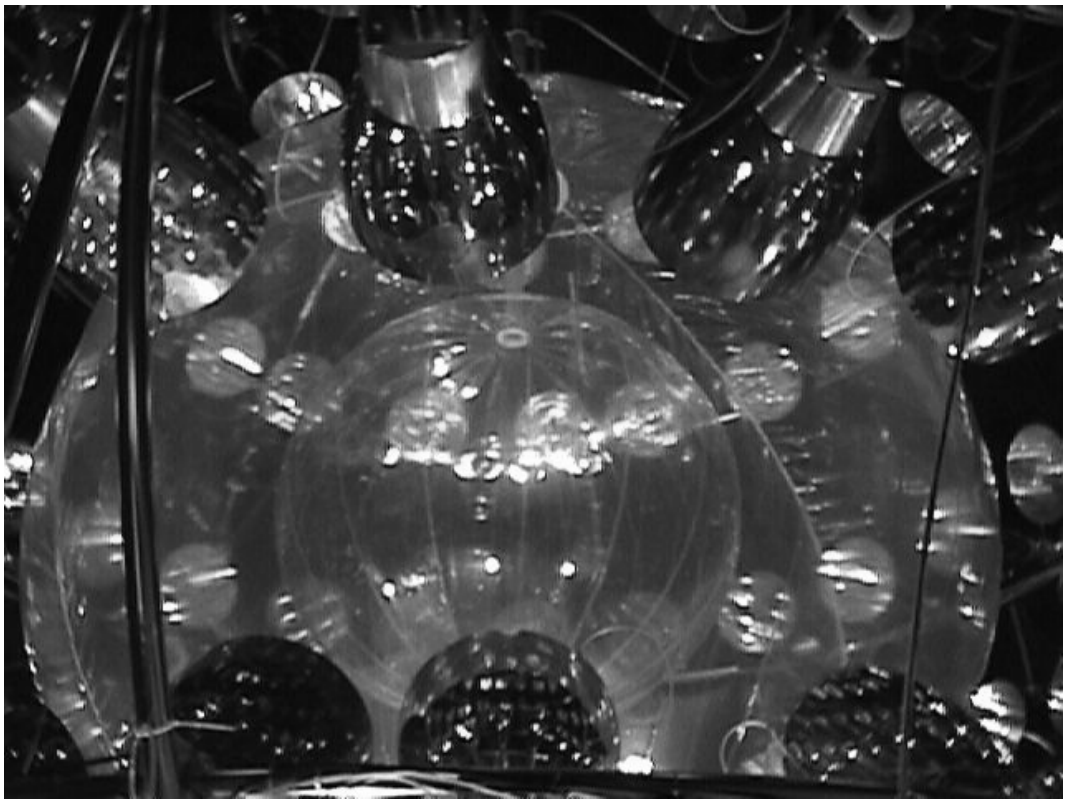

Figure 3.5: Photograph of the CTF2 Inner Vessel and Rn shroud.

Muon Veto

A muon veto was installed consisting of 16 PMTs mounted on the floor of the water tank looking upwards to detect Cerenkov light from muons crossing the water. For the muon veto PMTs a new encapsulation design has been developed by our group which will be used for the Outer Detector in BOREXINO and has been implemented in the CTF as a long-term test [Sei00, Len01]. Fig. 3.6 shows the design of the PMT encapsulation.

The PMT distribution has been optimized to detect muons that would produce signals with an energy in the neutrino window. The probability that the muon veto does not trigger on a muon event giving rise to a signal in the energy range of the neutrino window, is 0.8 % [Gri00]. The muon veto PMTs are located on the floor of the water tank on two rings with radius 2.4 m and 4.9 m, respectively. As their distance to the Inner Vessel is much bigger than that of the PMTs mounted on the open structure, as they are not directly looking towards the Inner Vessel and as they don't have light concentrators, their efficiency to detect scintillation light is substantially reduced compared to the PMTs mounted on the open structure. The trigger threshold of the muon veto is set to 4 photoelectrons. The probability that the muon veto triggers on normal scintillation events in the energy range of the neutrino window has been evaluated in a Monte Carlo simulation to be below 0.5 % for energies in the neutrino window (see fig. 3.7).

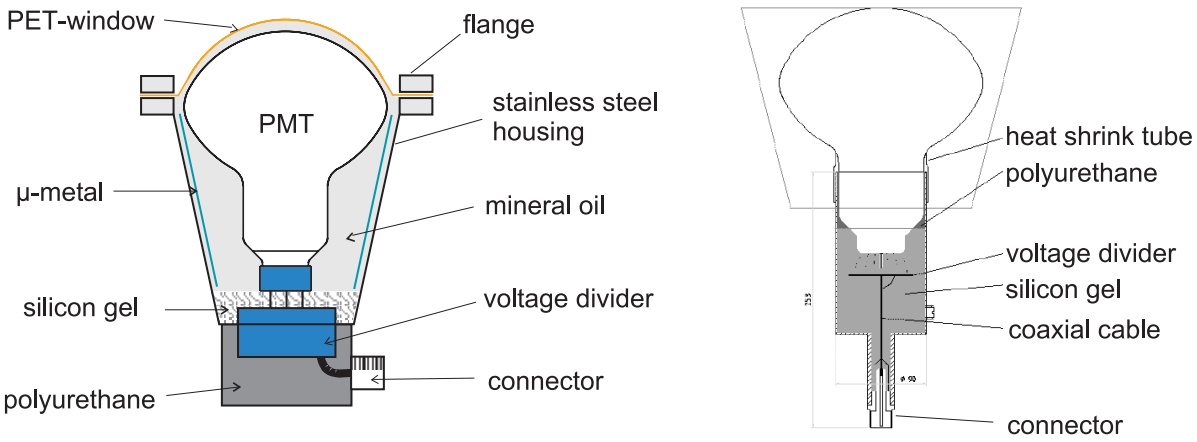

Figure 3.6: Design of PMT encapsulation for the CTF. The left picture shows the design of the muon veto PMTs for the CTF and BOREXINO. The right picture shows the design of the PMTs used in CTF2.

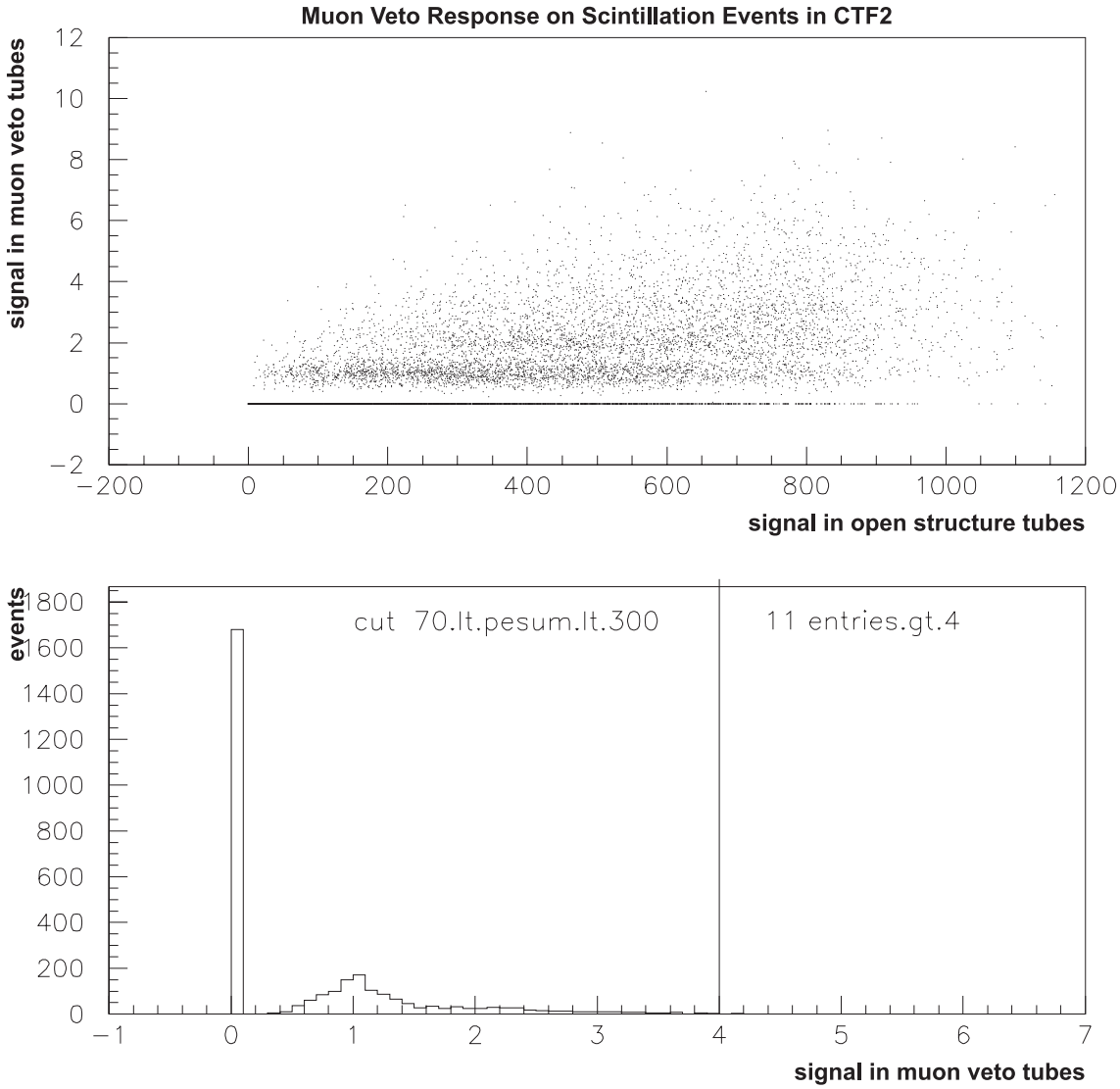

Figure 3.7: Monte Carlo simulation of the muon veto response on scintillation events. In the upper plot the pulse height in the muon veto PMTs is plotted versus the pulse height in the 100 PMTs on the open structure for scintillation events in the energy range 0 - 3 MeV. The pulse height signal in the muon veto PMTs for normal scintillation events in the energy range from 250 - 800 keV is plotted in the lower picture.

4 Position Reconstruction of Scintillation Events

4.1 Basic Idea

The position of a scintillation event is reconstructed using the timing information of the scintillation photons detected by the PMTs. The energy range of interest for BOREXINO goes from a few hundred keV to several MeV (the ^{7}Be window is from 250 to 800 keV). The track length of electrons with these energies in the scintillator is of the order of 1 cm, for alpha particles it is less than 1 mm. Compared to the spatial resolution of ~ 10 cm at 1 MeV, the track length is negligible, and the scintillation events can be considered as pointlike.

The reconstruction method developed in the frame of this work is based on a comparison of the measured data with simulated events:

1. The first step is a Monte Carlo simulation of the production and tracking of the scintillation photons through the detector and of the time and pulse height signals induced by localized energy deposits in the scintillator. This is done with a very high statistics for a number of grid points throughout the detector (the distance between the grid points is optimized between resolution and computing time).

2. The second step is the reconstruction program itself. It uses a maximum likelihood method for the comparison between a measured event and the simulated events from the grid points. For a given measured event (= a number of time and pulse height signals) the program scans the grid and calculates for each grid point the probability, that the event could originate from this grid point. The point with the highest probability, with an interpolation to its nearest neighbours, is assumed to be the place where the event occurred.

This method allows to consider a number of effects for the position reconstruction that cannot be accounted for in an analytical approach. The Monte Carlo code was designed to include all the physics felt to be important in light propagation, and uses parameters obtained from small-scale measurements and from source measurements in the CTF.

4.2 The Tracking of the Scintillation Photons

In the Monte Carlo simulation each photon is tracked from the place where it was produced to the place where it is absorbed or detected. The propagation of the photon in the transparent media of the detector (scintillator, water) is described by optical laws. In the tracking procedure the scintillation decay, the absorption and reemission of photons, the light scattering, the reflection or refraction on the border of different media, the reflection on the light guide surface and the photo multiplier time jitter are taken into account.

The Scintillation Process

Ionizing radiation passing through the organic scintillator transfers energy to the scintillator molecules. A fraction of this energy goes into the excitation of scintillator molecules which relax back to their ground state and sometimes emit light in this process, the remainder is dissipated nonradiatively. Due to the decay into lower energy states of the excited scintillator molecules the generation of scintillation photons is delayed a time t_d. The distribution of this delay is described by an exponential probability density function $f(t, \tau)$ where the parameter τ is the scintillation decay time. Generally the scintillator has more than one component, where each component is characterized by its decay time τ_i and its intensity q_i. The different components are due to different excited states of the molecules, which will be explained in more detail in chapter 5. The probability density function is

$$f(t, q, \tau) = \sum_i \frac{q_i}{\tau_i} e^{-t/\tau_i} , \qquad \sum_i q_i = 1 .$$

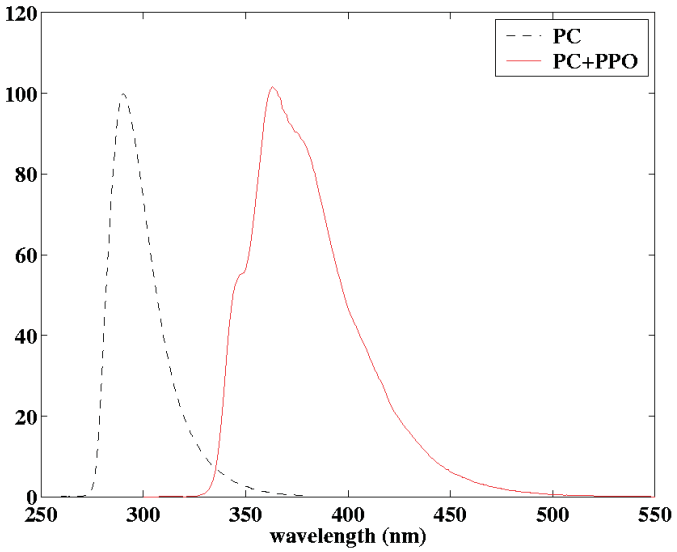

Figure 4.1: Normalized emission spectra of PC and $\mathrm{PC} + \mathrm{PPO}\,(1.5\,\mathrm{g/l})$.

The scintillator decay time was measured in laboratory experiments for excitation by alpha and beta particles (see table 4.1 and also fig. 5.2). The emission spectrum of the BOREXINO scintillator is shown in fig. 4.1.

particle excitation	τ_1 (ns)	τ_2 (ns)	τ_3 (ns)	τ_4 (ns)	q_1	q_2	q_3	q_4
β and γ	3.57	17.61	59.50	-	0.895	0.063	0.042	-
α	3.25	13.49	59.95	279.1	0.63	0.178	0.119	0.073

Table 4.1: The decay times and the relative quantities of the decay components of the liquid scintillator $\mathrm{PC} + \mathrm{PPO}\,(1.5\,\mathrm{g/l})$.

Absorption and Light Scattering

The attenuation length for $\mathrm{PC} + \mathrm{PPO}\,(1.5\,\mathrm{g/l})$ and for pure PC was obtained by measuring the absorption of a monochromatic light beam propagating along the x direction using a spectrometer and defining $\Lambda(\lambda)$ according to

$$I(x, \lambda) = I_0(\lambda) e^{-x/\Lambda(\lambda)}\,.$$

As shown in figure 4.2, interaction with the fluor is the most probable process for photons having wavelengths shorter than about 370 nm while photons with higher wavelengths preferably interact with the solvent. The photons absorbed by the fluor are reemitted isotropically with a

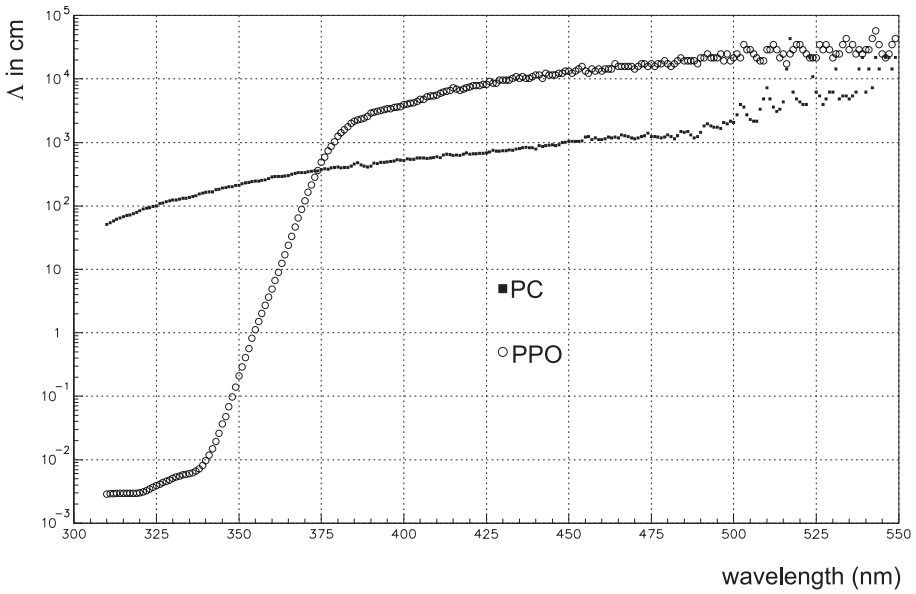

Figure 4.2: Attenuation length of PC and $\mathrm{PPO}\,(1.5\,\mathrm{g/l})$, calculated from the measured extinction coefficients [Ali00].

probability of 0.8 (the PPO quantum efficiency). The band-gap of the lowest electronic transitions in the PC molecule is at 320 nm, so that the absorption of PC drops rapidly at higher wavelengths. At longer wavelengths the measured extinction coefficient obeys roughly a λ^{-4} dependence typical for Rayleigh scattering.

In the simulation the interaction probabilities with PC and PPO were extracted from the extinction coefficient measurements. The interactions with PC were simulated as absorption for wavelengths shorter than 320 nm and as Rayleigh scattering for longer wavelengths. The interactions with PPO were modeled as absorptions for wavelengths shorter that 400 nm, and as Rayleigh scattering for longer wavelengths. In the case of an absorption in the scintillator, the reemission occurs with the quantum efficiency of PPO (0.8), as in the case of absorption by PC the excitation energy is shifted non-radiatively to the PPO, just as in the primary scintillation process. The reemission probability of the pure PC in the buffer region is only 0.34. The reemitted fluorescence photons were modeled with an isotropic distribution and with an emission time delay following the exponential fluorescence decay with $\tau = 1.6$ ns for PPO and $\tau = 27$ ns for pure PC. The spectrum of the reemitted photons was assumed to be the same as the primary emission spectrum.

The elastic Rayleigh scattering was simulated with an angular distribution of $P(\theta) \propto (1 + \cos^2\theta)$, with no effective time delay and no shift in the wavelength of the scattered photon.

Reflection and Refraction at Borders and Surfaces

In the CTF as well as in BOREXINO the scintillator will be $\mathrm{PC} + \mathrm{PPO}\,(1.5\,\mathrm{g/l})$, whereas the buffer liquid is different for the two detectors: water in the CTF and $\mathrm{PC} + \mathrm{DMP}\,(5\,\mathrm{g/l})$ in BOREXINO. If the refractive index is not the same for the two media, the processes of refraction and reflection at the interface can occur. The refraction angle at the interface can be calculated according to Snellius' law

$$\frac{\sin\varphi_1}{\sin\varphi_2} = \frac{n_2}{n_1}\,.$$

The probability that a photon is reflected at the interface scintillator-water is given by the Fresnel's law, depending on the polarization of the photon,

$$\begin{aligned} R_\perp &= \left(\frac{\sin(\varphi_1 - \varphi_2)}{\sin(\varphi_1 + \varphi_2)}\right)^2 \\ R_\parallel &= \left(\frac{\tan(\varphi_1 - \varphi_2)}{\tan(\varphi_1 + \varphi_2)}\right)^2 . \end{aligned}$$

As the refractive index of the scintillator (~ 1.5) is larger than that of water (~ 1.33), for incident angles $\varphi_1 > \arcsin(n_2/n_1) \approx 62.5^\circ$ total reflection occurs. If the scintillator/water interface is an ideal sphere, then this totally reflected light is 'trapped' by a number of successive internal reflections (as the incidence angle relative to the sphere stays the same). This 'trapped light' may be detected at the PMTs only after a long delay, depending on whether it

eventually escapes due to imperfections of the Inner Vessel (IV) shape and material. This creates unpredictable distortions in the energy spectrum and the time distributions, and therefore has negative effects on position reconstruction (fiducial volume) and pulse shape discrimination. The exact behaviour is hard to predict by simulations, since the shape of the vessel would have to be known very accurately.

While in the CTF the inside tank walls are coated with a black epoxy with a very low reflectivity, in BOREXINO reflections from the surface of the stainless steel sphere have to be taken into account. The diffuse reflectivity of passivated stainless steel has been measured with a photo spectrometer using an integrating sphere. The wavelength dependence of the diffuse reflectivity for two different surface treatments of the stainless steel is shown in fig. 4.3. For the BOREXINO steel sphere, the passivated surface has been chosen.

Reflections at the Stainless Steel Sphere are simulated according to Lambert's law (reflection of rays on rough surfaces)

$$dW \;=\; C\,\cos\theta\,d\Omega \;=\; C\,\cos\theta\,\sin\theta\,d\theta\,d\varphi$$

For incident angles greater than 80° mirror reflection is assumed.

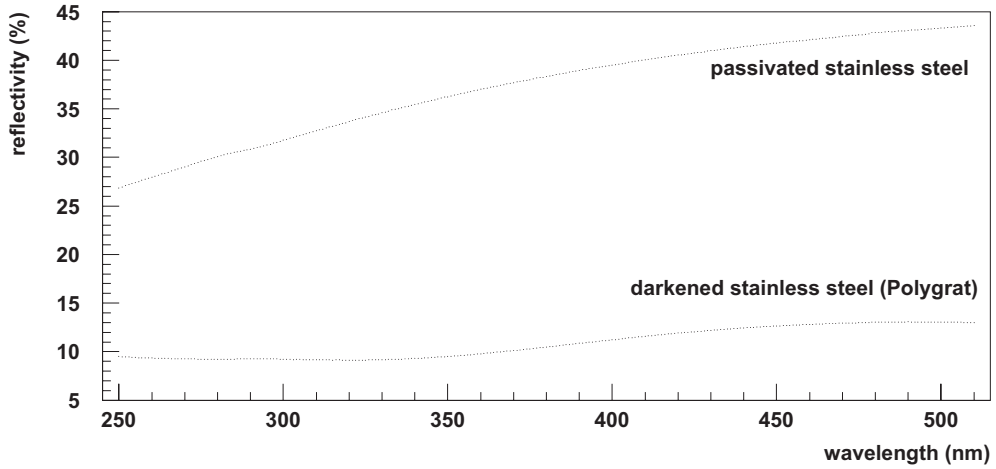

Figure 4.3: The diffuse reflectivity of passivated stainless steel and darkened stainless steel. The BOREXINO Stainless Steel Sphere has a passivated surface.

Light Concentrators

The shape of the concentrators is designed to produce a uniform response to events inside the IV with a misalignment tolerance of $\sim$5 degrees. The angular acceptance of the concentrators drops rapidly for angles greater than 36 degrees, i.e. for events at a radius bigger than 5 m. The concentrators for BOREXINO are made of high purity aluminum. The reflectivity of aluminum is 92 % at 400 nm. The amplification factor of the concentrators has been measured to be 1.9 ± 0.2, which is very close to the optimal amplification factor (geometrical factor

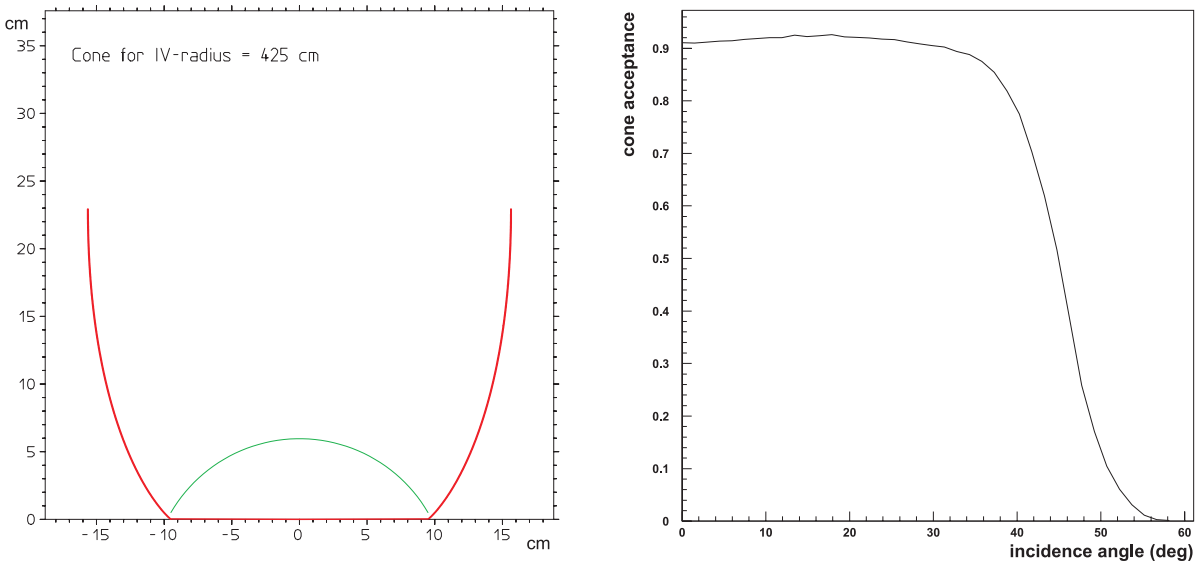

Figure 4.4: In the left picture the shape of the BOREXINO concentrators is shown. In the right picture the angular acceptance of this cone shape is shown.

$(15\,\mathrm{cm}/9.5\,\mathrm{cm})^2 \times$ reflectivity 92 % ≈ 2.3) [Obe01]. The shape and the angular acceptance of the light concentrators are shown in fig. 4.4.

PMT Quantum Efficiency, Time Jitter and Counting Statistics

The PMTs used in the CTF as well as in BOREXINO are the 8" Thorn EMI 9351 photomultipliers. Their characteristics are: high quantum efficiency (26 % at 420 nm), limited transit time spread ($\sigma = 1$ ns), good pulse height resolution for single photoelectron pulses (peak/valley $= 2.5$), low dark noise rate (1 kHz), low after pulse probability (2.5 %), gain 10^7. The quantum efficiency of the photo cathode of the PMT is shown in fig. 4.5. A typical pulse height distribution of single photoelectron pulses and the transit time distribution is shown in fig. 4.6 for one of the PMTs used in BOREXINO. In the simulation, if a photon hits a PMT, the probability for a reflection at the water-glass interface is calculated. If the photon is not reflected, it creates a photoelectron with a probability according to the PMT quantum efficiency. The pulse height signal is calculated according to a Poisson distribution. For the time signal, the transit time of the PMT has to be taken into account. The mean transit time is 4.5 ns, with a Gaussian time jitter of 1 ns.

The Tracking Program

The data flow of the tracking program is outlined here for BOREXINO (the tracking in the CTF is analogous):

1. The tracking algorithm starts with the generation of a scintillation photon at the position

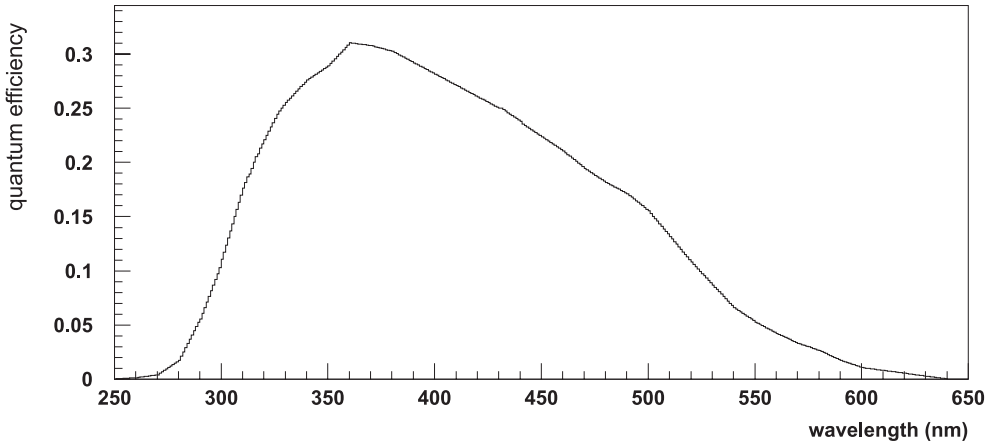

Figure 4.5: Quantum efficiency of the 8” Thorn EMI 9351 photomultiplier used in BOREXINO.

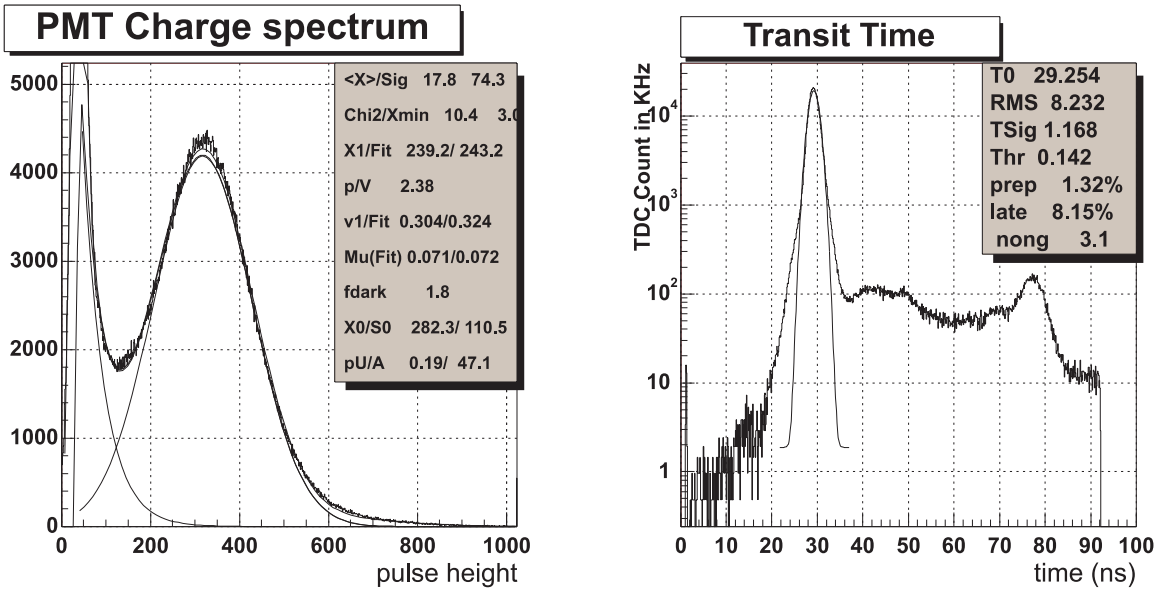

Figure 4.6: Pulse height distribution of the single photoelectron pulse and transit time distribution measured with one of the 8” Thorn EMI 9351 photomultipliers used in BOREXINO.

$\vec{x}$. It is assigned a wavelength λ, a scintillation delay time t_s, and a direction $\vec{u}$. The refractive index $n(\lambda)$ is calculated depending on the medium and wavelength.

2. Calculate the distance to the next border and the free path lengths for absorption and scattering on PC and PPO. The process with the minimum distance r_{min} occurs. The photon proceeds to this point ($t \to t + r_{min}n(\lambda)/c$, $\vec{x} \to \vec{x} + r_{min}\vec{u}$).

3. If an interaction occurs:

   - Scattering: new direction of the photon $\vec{u} \to \vec{u'}$, continue with 2.
   - Absorption: calculate the probability for reemission. If reemission occurs, go to 1.

4. If the photon reaches a surface:

   - Inner Vessel Radius, 425 cm (only for water buffer): Reflection? Refraction? Calculate new direction ($\vec{u} \rightarrow \vec{u'}$), index of refraction in the new medium, and continue with 2.
   - Radius of PMTs with cones, 635 cm: Cone aperture hit? Is it reflected by the cone? If it is accepted, proceed to the PMT. Is it reflected on the surface? If not, go to 5, otherwise continue with 2.
   - Radius of PMTs without cones, 655 cm: PMT hit? If yes, is it reflected? If not, goto 5, otherwise calculate reflection angle and continue with 2.
   - Stainless Steel Sphere, 685 cm: absorption or reflection on stainless steel?

5. PMT hit: the photon is converted into a photoelectron according to the photocathode efficiency. Calculate the time jitter and the pulse height signal. If the pulse height is above the threshold, store the time of the signal.

When the grid for the reconstruction is computed, the program loops over a spatial grid, where a fixed number of photons starts from each grid point. In the end, only the time of the first photoelectron of each PMT is stored for each grid point. This simulation has to be done with a very high statistics, in order to get the earliest possible arrival time of a photon at each PMT $t_{\mathrm{min},i}(x, y, z)$.

The probability density function for a single photoelectron $\rho(t)$ is derived from a Monte Carlo simulation, where a number of photons starts from the center of the detector (so that the distance to all PMTs is the same) and is stored in a separate file. This probability density function reflects the decay time of the primary scintillation light emission, additional delays introduced through absorption and reemission, scattering, reflection, etc. of the photon on its way to the PMT, and the time jitter of the PMT. In principle, this distribution also depends on the distance between the primary emission point and each individual PMT, but in the first order it is the same for all positions inside the scintillator. Fig. 4.7 shows the averaged probability density function for the CTF for two different positions, in the center and in a distance of 94 cm from the center (corrected for the time of flight to the PMTs). There are notable differences only for late arrival times, which do not provide good information for the position reconstruction, anyway.

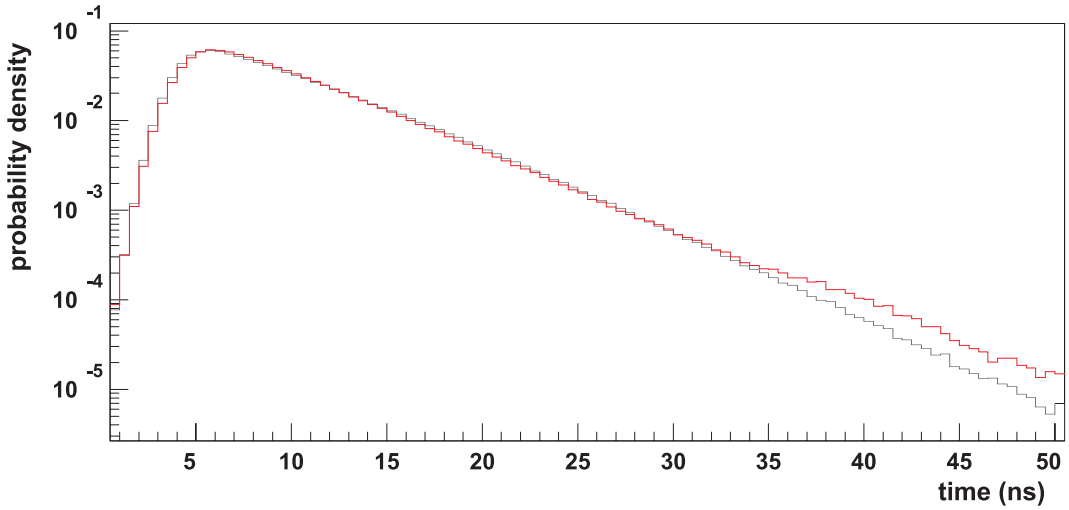

Figure 4.7: The probability density function for a single photoelectron $\rho(t)$ in the CTF, averaged over all 100 PMTs for two different locations inside the scintillator: in the center (0,0,0) and at (60cm,60cm,40cm).

4.3 The Reconstruction Program

The reconstruction is based on a maximum likelihood method. For a given measured event (= a number of time and pulse height signals) the program scans the grid and calculates for each grid point the probability that the event could have taken place at this grid point. The point with the highest probability, with an interpolation to its nearest neighbours, is assumed to be the place where the event occurred.

The Likelihood Function

The likelihood function can be written as

$$\mathcal{L}(x,y,z) = \left(\prod_{i=1}^{N_{hit}} p_i(t_i, n_i, x, y, z) \right)$$

where $p_i(t_i, n_i, x, y, z)$ is the normalized probability, that the i-th PMT registers n_i photoelectrons after the time t_i, under the assumption that the photons were emitted at the point (x, y, z). In practice, one maximizes $\log \mathcal{L}$, which is the sum of $\log(p_i(t_i, n_i, x, y, z))$.

The Single Photoelectron Probability Density Function

The arrival time of each photoelectron follows a probability density function $\rho(t)$ which is a convolution of the decay time of the scintillator, the time of flight of the photon through the

detector, the time delay introduced by scattering and/or absorption-reemission processes, and the time jitter of the PMT. The probability density function for a single photoelectron $\rho(t)$ is derived from a Monte Carlo simulation of the detector and archived in a look-up table. For the CTF, it is shown in fig. 4.7.

Multiple Hits

In the CTF the data acquisition registers only the arrival time of the first photoelectron for each electronic channel while the total number of photoelectrons per channel arriving within a time window of a few hundred nano seconds is recorded with an ADC. In BOREXINO the arrival time of each photoelectron will be recorded, if they arrive with at least 140 ns distance. In BOREXINO the probability for multiple hits is greatly reduced compared to the CTF, as each PMT covers a smaller solid angle. In the CTF, for a 1 MeV event the average value is 3 hits per PMT, while in BOREXINO it will be only 0.2 hits per PMT.

The probability for PMT i, that the first one out of n_i photoelectrons has been registered at the time t_i can be calculated to be

$$p_i^1(t_i, n_i) = n_i \cdot \rho(t_i) \cdot \left(\int_{t_i}^{\infty} \rho(\tau) d\tau \right)^{n_i - 1} ,$$

where t_i is derived from the measured time tdc_i in the following way:

$$\begin{aligned} tdc_i &= T_{\text{event}} + t_{\text{emission},i} + t_{\text{flight},i} + t_{\text{scatter},i} \pm t_{\text{jitter},i} \\ &= T_{\text{event}} + t_{\text{min},i}(x, y, z) + t_i \\ \\ tdc_j &= T_{\text{event}} + t_{\text{min},j}(x, y, z) + t_j \\ \\ \Rightarrow \qquad t_j &= t_i + (tdc_j - t_{\text{min},j}(x, y, z)) - (tdc_i - t_{\text{min},i}(x, y, z)) \end{aligned}$$

The $t_{\text{min},i}(x, y, z)$ are archived in a large multidimensional look-up table for each grid point and PMT (they are derived from the Monte Carlo simulation, which was described in the last section).

Noise Hits

The problem of (white) noise hits, which occur uncorrelated with the scintillation event, is equivalent to a probability density ρ_0 constant in time. This is already solved by substituting $\rho(t)$ with the maximum probability $\texttt{MAX}(\rho(\texttt{t}), \rho_0)$. More correctly one has to add ρ_0 to $\rho(t)$ and renormalize afterwards. In practice this is equivalent to an additional constant bias to $\log \mathcal{L} \sim N_{hits} \cdot \log(\rho_0)$, which thus only slightly affects the minimization process. For a noise rate of 1 kHz one gets $\rho_0 \approx 1 \cdot 10^{-6} \text{ns}^{-1}$.

Grid Search and Interpolation

The reconstruction algorithm scans the grid, and calculates the likelihood for various grid points. The point with the maximum value is then assumed to be the place where the event occurred. In the beginning the whole grid was searched to make sure that the global minimum of the likelihood function is found. It turned out, that a simple gradient search is good enough to give the same results, i.e. local minima are not a problem for the reconstruction. The 'center of light', which is calculated by summing up the position of the fired PMTs (channels) weighted with their charge signal, is taken as start position for the grid search:

$$\vec{r}_{start} = \sum_{i=1}^{N_{hit}} n_i \cdot \vec{r}_i \; .$$

The 'center of light' usually lies within 1 m distance from the real position, i.e. it is a good first estimator for the real position.

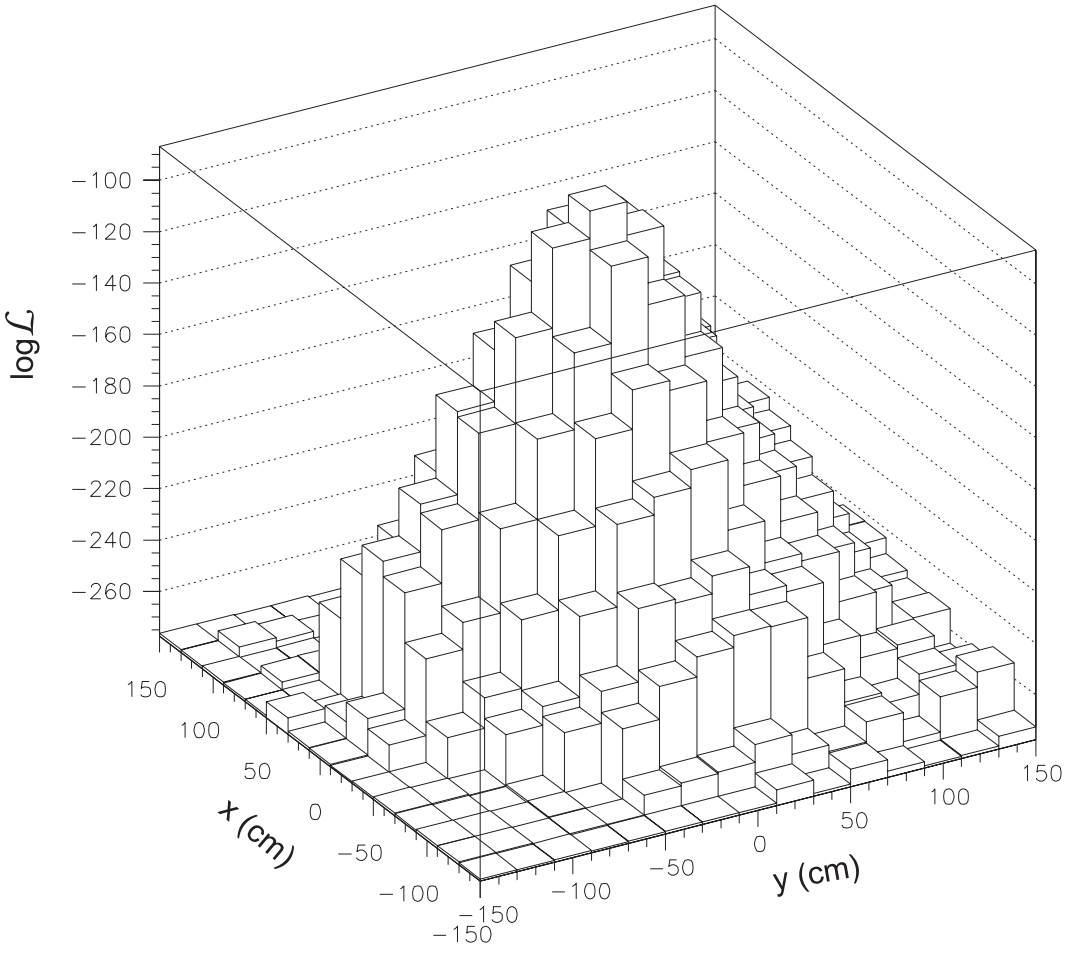

Figure 4.8: For a simulated CTF event with 20 cm grid size, $\log \mathcal{L}$ is plotted versus the coordinates of one plane of the grid, including the position where $\log \mathcal{L}$ is maximal.

In fig. 4.8 the logarithm of the likelihood function is shown for one plane of the grid including the maximum value. It can be seen from this picture that the shape of $\log \mathcal{L}$ around the maximum is well approximated by a parabolic shape. The position of an event is calculated by parabolic interpolation from the grid point with the maximal $\log \mathcal{L}$ to its nearest neighbours. Applying an overall fit instead of a direct interpolation could help to further improve the position resolution.

Error Estimation

As the likelihood function can be approximated with a Gaussian, $\log \mathcal{L}$ can be written as

$$y = \log \mathcal{L} = -\frac{1}{2\sigma^2}x^2 + c \qquad \Rightarrow \qquad y'' = -\frac{1}{\sigma^2}$$
$$\Rightarrow \qquad \sigma = \sqrt{-\frac{1}{y''}}\,.$$

The inverse square root of the second derivative is taken as an estimate for the error of the reconstructed position. A larger value of σ corresponds to a less pronounced maximum of the likelihood function.

The Optimum Grid Size

The optimum grid size was chosen as a compromise between resolution and size of the grid file (i.e. memory usage and computing time). Comparing the results obtained with a grid size of 50 cm, 20 cm, 10 cm and 5 cm in the CTF, it turned out that the resolution doesn't improve for a grid size finer than 20 cm. For the CTF a 20 cm grid was used for all the following calculations. For BOREXINO a 50 cm grid was used for the simulations, due to limited computing power. For the reconstruction of real BOREXINO events, one possibility would be to presort the events according to their 'center of light'-position into several subvolumes of the detector and use a finer grid for the reconstruction in these smaller volumes. The 'center of light' usually lies within 1 m distance from the real position, i.e. it is a good first guess for the real position of the event.

4.4 Results Obtained with Simulated Data

Monte Carlo for Alpha, Beta and Gamma events

To study the behaviour of the reconstruction code depending on the position, energy and decay type, I have simulated energy deposits from α, β and γ decays at different positions in the BOREXINO and CTF detector.

The simulation uses the scintillation decay times measured for different types of particle excitation (see table 4.1). The photon yield of the scintillator is assumed to be 10500 photons/MeV. This number reproduces approximately the photoelectron yield measured in the CTF (~ 300 photoelectrons/MeV). The energy deposits of α and β particles are assumed to be pointlike. The quenching of the alpha energies is included as measured in laboratory (see table 5.1). The energy of the α or β decay is 'translated' into the corresponding number of photons which start at the point of the energy deposit with a time delay according to the scintillation decay time, and are tracked throughout the detector as described in section 4.2.

The interaction of γ-rays in the scintillator is simulated including Compton scattering and photo effect. Pair production plays no significant role in the energy range of interest ($\leq$ 3 MeV). The γ travels through the detector with the speed of light (index of refraction ≈ 1). At each interaction point, the number of photons corresponding to the energy of the scattered electron, start with a time delay according to the excitation by β particles, and are tracked throughout the detector.

Energy Dependence of the Spatial Resolution for Different Particles

The approximation of the resolution of the spatial reconstruction for a point-like event is given by

$$\Delta r \sim \frac{c\,\sigma_t}{\sqrt{n_{pe}}}$$

where c is the speed of light, σ_t is the error of one time measurement and n_{pe} is the number of measurements (= number of detected photons).

The Monte Carlo simulation for the CTF leads to the following results, which are plotted in fig. 4.9:

For beta events the Monte Carlo gives an energy dependence of the spatial resolution as

$$\sigma_x \simeq \frac{104\,\mathrm{cm}}{\sqrt{n_{pe}}} \simeq \frac{6.0\,\mathrm{cm}}{\sqrt{E\,(\mathrm{MeV})}}\,,$$

assuming a photoelectron yield of 300 photoelectrons per MeV in the CTF.

For alpha events the spatial resolution is slightly worse, as more scintillation light is emitted at late times. The energy dependence is still approximately $\propto 1/\sqrt{n_{pe}}$.

For gamma events the situation is more complicated: a gamma interacts in the scintillator mainly due to Compton scattering. Therefore it deposits energy at various points in the scintillator at different times (the γ-ray travels with the speed of light, as $n \approx 1$). The event registered by the detector consists of an overlap of these single interactions. The effective position of such an event is the 'center of light' of the various energy deposits. A gamma event is therefore called an 'extended event'. The higher the energy of the gamma, the larger the extension of the event. The Monte Carlo gives for the energy dependence of the spatial resolution a rather flat curve, after an initial decrease at low energies. Plotting the reconstructed position of the γ minus its 'center of light' position, yields about the same position resolution as for β events. The different behaviour for the resolution of gamma events therefore really originates in the spatial extension of the energy deposit itself. Therefore the resolution for beta-like events has to be employed for the prediction of the radial distribution of the external background. The external background consists of gamma rays that are emitted outside the

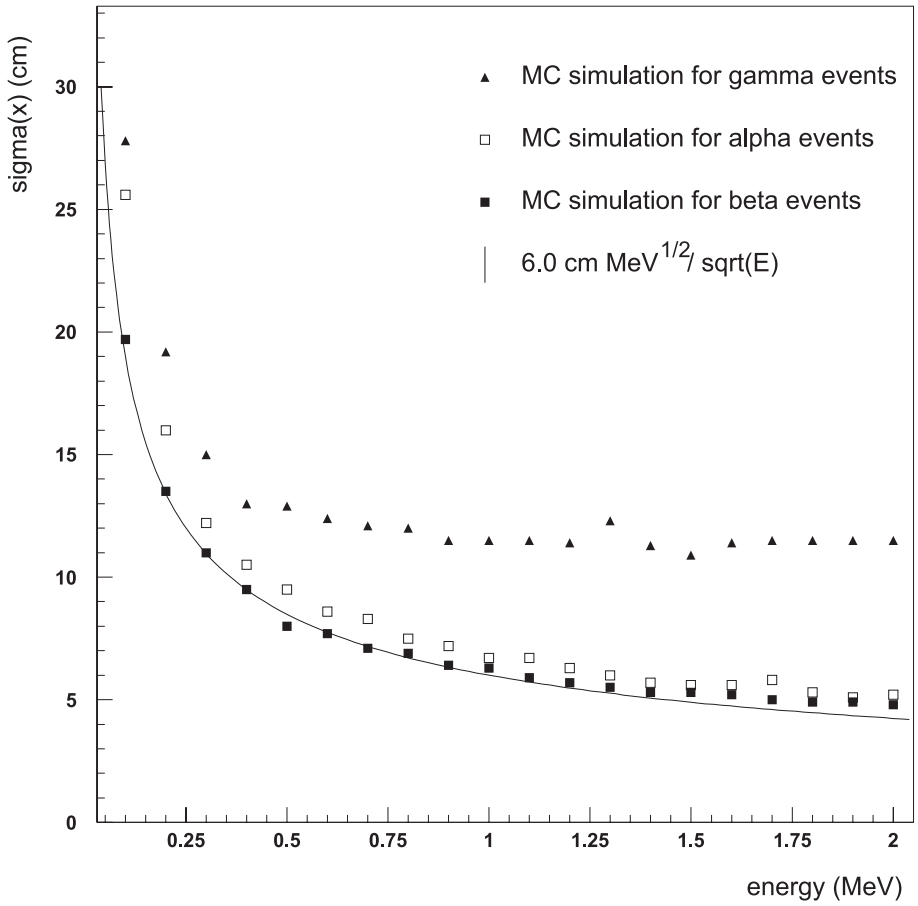

Figure 4.9: Energy dependence of the position resolution for alpha, beta and gamma events starting from the center of the CTF Inner Vessel. For the pointlike alpha and beta events the resolution follows very closely the expected $1/\sqrt{n_{pe}}$ behaviour. As the gammas interact at various points in the scintillator, and the distance between these interactions increases with energy, the resolution doesn't improve with increasing energy.

scintillator volume, but deposit a fraction of their energy in the scintillator. Monte Carlo simulations of these background events yield their 'center of light' position, which then has to be folded with the estimated energy resolution to give a meaningful prediction.

For BOREXINO the behaviour is very similar to the CTF (see fig. 4.10). The position resolution for the pointlike beta events is a little bit better than in the CTF, due to the higher photoelectron yield (~ 350 pe/MeV for BOREXINO, ~ 300 pe/MeV for the CTF). The larger detector size however gives rise to a bigger time spread due to scattering and absorption/reemission processes. The energy dependence of the spatial resolution is

$$\sigma_x \simeq \frac{101\,\mathrm{cm}}{\sqrt{n_{pe}}} \simeq \frac{5.4\,\mathrm{cm}}{\sqrt{E\,(\mathrm{MeV})}}\,.$$

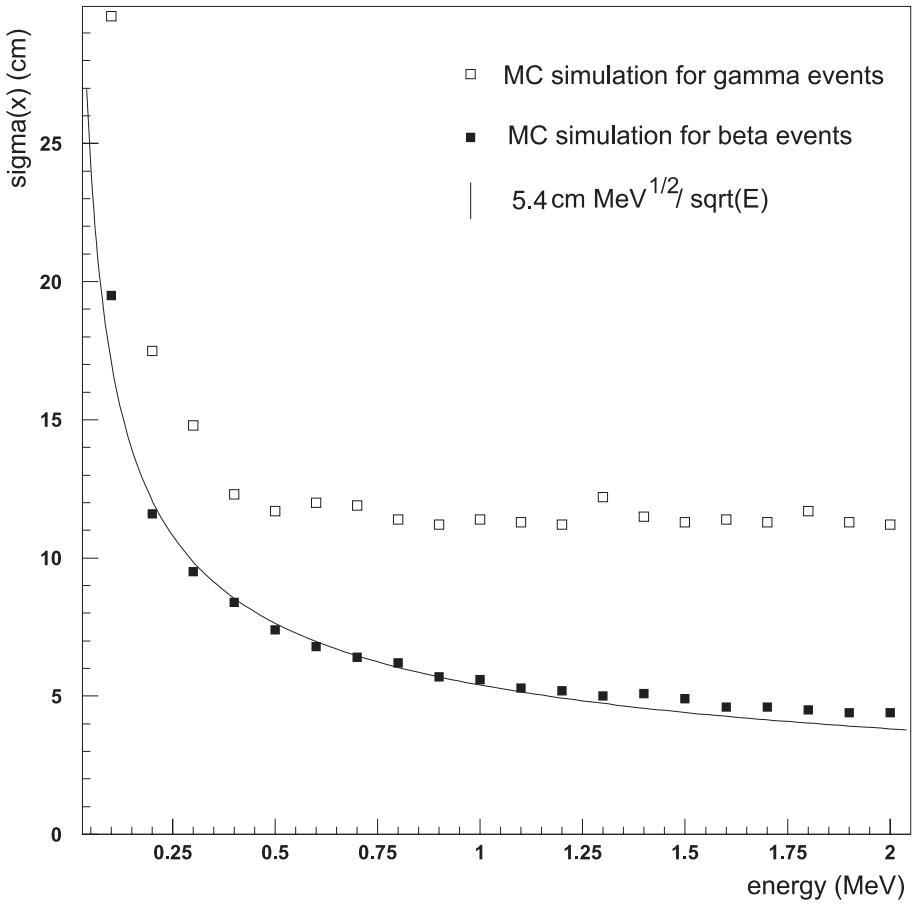

Figure 4.10: Energy dependence of the position resolution for beta and gamma events starting from the center of the BOREXINO Inner Vessel.

5 Particle Identification with a Neural Network

In the first section of this chapter I will describe the scintillation process in organic scintillators, and explain how the ionization density of the exciting radiation is related to the timing behaviour of the emitted scintillation photons. This difference can be exploited for α/β discrimination. In the next section I will introduce the method of neural networks, that I have applied to the problem of α/β identification. In the last section results obtained with Monte Carlo simulations of the CTF and BOREXINO and with data from a CTF2 source run are reported and confronted with the standard 'charge integration' method.

5.1 Pulse Shape Discrimination in Liquid Scintillator

5.1.1 The Scintillation Process

Organic scintillators are aromatic compounds with planar molecules built up mainly from condensed or linked benzenoid rings (see e.g. fig. 6.1). One fundamental characteristics of the molecular structure is the presence of delocalized electrons occupying so called π-orbitals which extend above and below the molecular plane. The π-electronic states are of particular interest because transitions between these states lead to the luminiscence observed in the scintillation process.

The electronic levels of an organic molecule with a π-electron structure can be represented schematically as shown in fig. 5.1. The ground state is a singlet in which the π-electron spins are fully paired. Excitation can lead from the ground state S_0 to an excited singlet state S_i (electron spins paired) or triplet state T_i (electron spins unpaired). Associated with each π-electronic level is a vibrational band of substates S_{ix}, T_{ix}. The absorption transition from the ground state S_0 to the triplet states T_i is spin-forbidden and unlikely to occur due to photon excitation. Excitement into triplet states is possible with ionizing radiation. The higher singlet electronic states are quickly (on the order of pico seconds) de-excited to the S_{10} state through radiationless internal conversion. Fluorescence light is emitted by radiative transitions between the first excited π-electron state S_{10} and the vibrational substates of the ground state S_{0x}, hence the fluorescence spectrum lies predominantly at wavelengths longer than the singlet

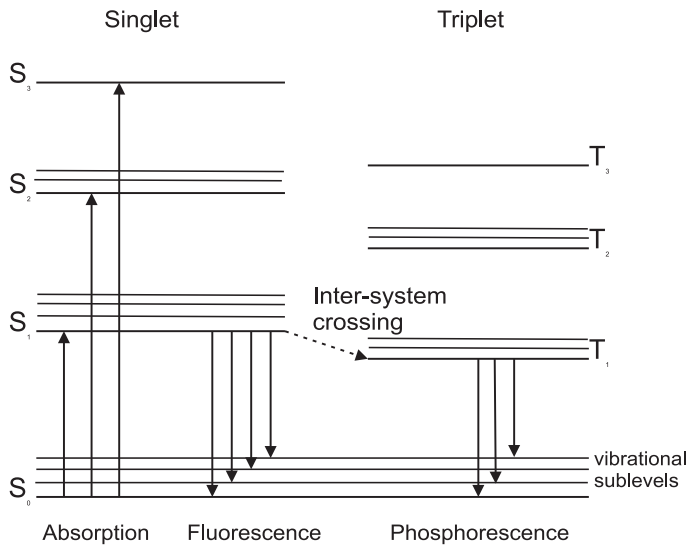

Figure 5.1: π electronic energy levels of an organic molecule. S_0 is the ground state. S_i are excited singlet states (spin 0), T_i are excited triplet states (spin 1). Taken from [Bir64].

absorption threshold. The scintillator is thus transparent to its own scintillation emission. The typical radiative lifetime of the π-singlet state S_{10} is of the order of $10^{-8} - 10^{-9}$ s. Radiative transitions from T_1 to S_{0x} are called phosphorescence. Due to the forbidden nature of the transition, the radiative lifetime of T_1 can range up to a few seconds. Phosphorescence does not play a significant role in the scintillation process. The T_1 state decays instead by the process of triplet annihilation:

$$T_1 + T_1 \rightarrow S_1 + S_0 + \text{phonons}$$

The molecule in S_1 subsequently decays to the ground state with the same wavelength spectrum, but with a time delay that is determined by the rate of collisions between T_1 exited molecules. This process is called delayed fluorescence. In some scintillators, this slow component can last up to 1 μs.

5.1.2 Response to Different Radiations

Only a small fraction q_E of the energy of the incident particle or radiation is transformed into light. For radiation with a low ionization density (electrons, γ-rays), the relation between the differential energy loss per path length dE/dx of the incident particle and the resulting luminiscence energy per path length dL/dx is linear:

$$\frac{dL}{dx} = A \cdot \frac{dE}{dx}$$

The higher specific ionization of heavier particles (protons, alpha particles, ...) results in a lower scintillation yield as more of the energy goes into nonlight-producing processes. Compared to an electron track, nearly 90 % more of the excited molecules produced along an alpha

track are quenched by competing reactions before they have an opportunity to transfer their energy to the fluors which will emit the photons. Hence, an alpha particle will produce, on average the same number of photons as an electron with about one tenth of its energy. Quenching results in a non-linear relation between the deposited energy and the emitted scintillation light. This relation can be parametrized as

$$\frac{dL}{dx} = \frac{A\frac{dE}{dx}}{1 + kB\frac{dE}{dx}} \quad \text{(Birk's law)}.$$

kB is a characteristic magnitude of the quenching (in Birks model, $B\frac{dE}{dx}$ is the fraction of 'damaged' molecules along the particle track; k is the fraction of these molecules which cause quenching). The alpha quenching in the scintillator mixtures tested in the CTF has been measured on laboratory samples for various alpha energies (see table 5.1). The pulse height of the alpha particles was compared to the pulse height of betas with known energies (Compton scattering of gamma rays). The ratio of the alpha energy to the 'beta -equivalent', measured energy is defined as the quenching factor. From these measurements, the value of kB can be calculated:

$$\mathrm{PC} + \mathrm{PPO}\,(1.5\,\mathrm{g/l}) \qquad kB = (1.10 \pm 0.05) \cdot 10^{-2}\,\mathrm{cm/MeV}$$

$$\mathrm{PXE} + \mathrm{TP}\,(2\,\mathrm{g/l}) + \mathrm{bisMSB}\,(20\,\mathrm{mg/l}) \qquad kB = (0.89 \pm 0.05) \cdot 10^{-2}\,\mathrm{cm/MeV}$$

The relative intensity of the fast and the slow scintillation components also depends on the energy loss per unit path length, since the slow component is less affected by quenching. Thus, the relative intensity of the slow component is larger for alpha particles than for electrons, thus allowing to discriminate between the two types of radiation on the basis of the decay time distribution.

Element	α-energy (MeV)	measured energy (keV)	quenching factor
$\mathrm{PC} + \mathrm{PPO}\,(1.5\,\mathrm{g/l})$			
^{222}Rn	5.49	(410 ± 6)	(13.3 ± 0.2)
^{218}Po	6.00	(483 ± 6)	(12.4 ± 0.2)
^{214}Po	7.69	(751 ± 7)	(10.2 ± 0.1)
^{210}Po	5.30	(395 ± 10)	(13.4 ± 0.4)
$\mathrm{PXE} + \mathrm{TP}\,(2\,\mathrm{g/l}) + \mathrm{bisMSB}\,(20\,\mathrm{mg/l})$			
^{222}Rn	5.49	(534 ± 10)	(10.3 ± 0.2)
^{218}Po	6.00	(624 ± 10)	(9.6 ± 0.2)
^{214}Po	7.69	(950 ± 12)	(8.1 ± 0.1)
^{210}Po	5.30	(490 ± 10)	(10.8 ± 0.2)

Table 5.1: Quenching factors for alpha particles with different energies for scintillator mixtures based on PXE and PC. Measured on small samples [Nef96].

5.1.3 Pulse-Shape-Discrimination

The intensity of photons from a scintillation event as a function of time can be divided into at least two components, fast and slow. The fast component has a decay time equal to the fluorescence lifetime of the fluorescing species (the fluorescence solute). The slow component has a decay time which is diffusion controlled. It has been shown to be due to the annihilation of two triplet excited molecules $\mathrm{T} + \mathrm{T} \rightleftharpoons \mathrm{S}_1 + \mathrm{S}_0$. The production of triplet excited molecules is related in part to the specific ionization of the excitation particle: The higher the specific ionization of the particle, the more triplet excited molecules are created. Two different types of particle which produce the same intensity of the fast component will have different intensities of the slow component. Thus it is possible with pulse shape discrimination to distinguish two types of particles with different specific ionization, especially electrons from heavy particles like neutrons or alpha particles. The ability to discriminate between α and β or γ radiation is based on the difference in the tail of the time distributions of the scintillator decay, as shown in fig. 5.2 (see also table 4.1).

5.1.4 The Flash-ADC

In collaboration with the company CAEN, a 400 MHz waveform digitizer was developed for BOREXINO, which was first tested in the CTF2. Its basic function is to digitize the analog

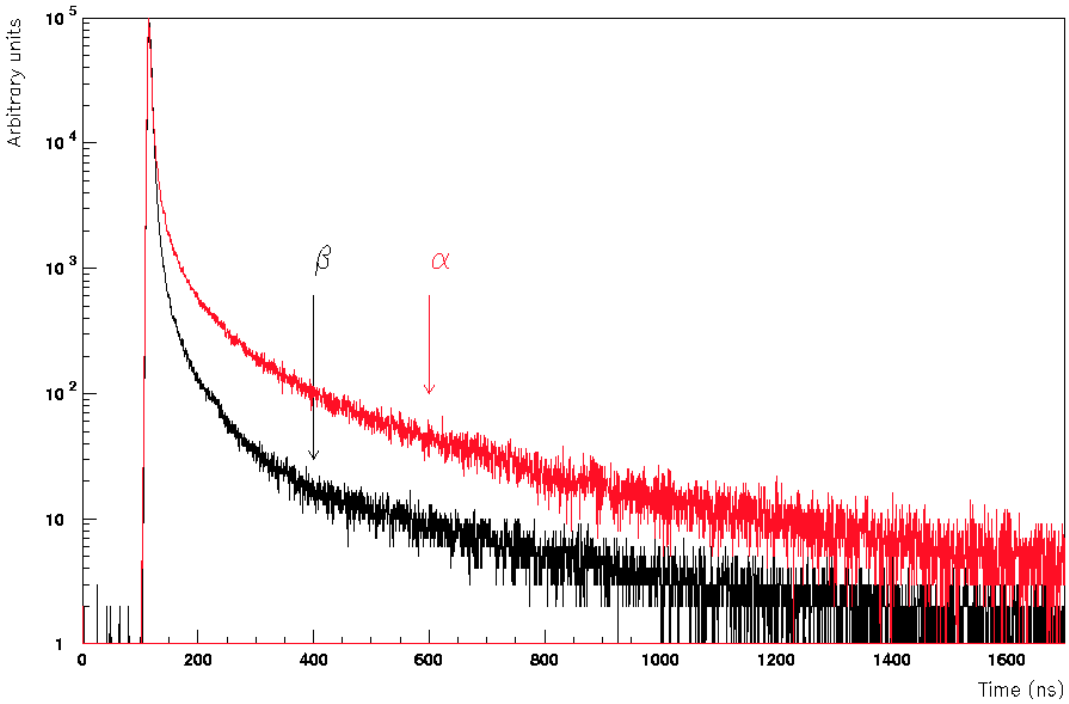

Figure 5.2: Time decay distribution of $\mathrm{PC} + \mathrm{PPO}\,(1.5\,\mathrm{g/l})$ for emission excited by α or β radiation.

input signals and store the data into dual port buffers where they may be read by the VME bus. The digitizer type is an 8 bit flash ADC with a sampling period of 2.5 ns. There are three flash ADC channels per board. Each channel is associated to a 256 kbyte memory, giving a 655.36 μs memory depth. The read-out has no dead time and is limited only by the speed of the VME bus.

In the CTF2, one prototype board with three channels was used: channel 1 was fed with the sum of all PMTs, channel 2 with the amplified sum, and channel 3 with the signal of one PMT.

In BOREXINO, each flash ADC channel will have the analog sum of 24 PMTs as input. The gain will be adjusted so that signals up to 8 MeV energy can be recorded. The main acquisition system of BOREXINO, which is designed to detect single photoelectrons, suffers from photoelectron pile-up for energies higher than 2 MeV. This is well above the solar neutrino detection window (250 - 800 keV for ^{7}Be neutrinos, 800 - 1400 keV for pep neutrinos), but some interesting signals lie above 2 MeV (reactor-antineutrinos, neutrinos from Supernovae ...). The energy and waveform of these events will be recorded by the flash ADCs. One additional flash ADC channel will be fed with the analog sum of all PMTs with the gain adjusted to performing pulse shape based particle discrimination in the energy range below 1 MeV.

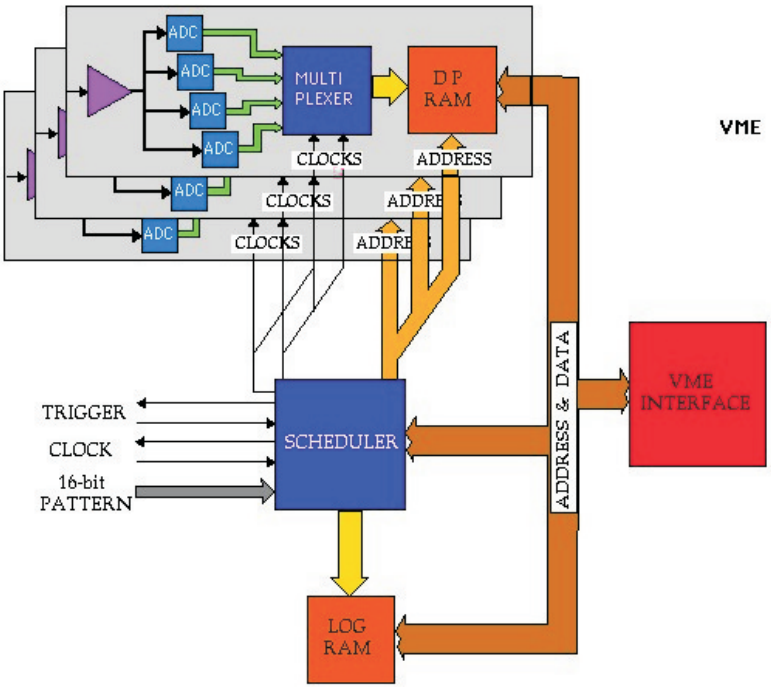

Figure 5.3: Block diagram of the flash ADC board.

5.2 Artificial Neural Networks

The term artificial neural network (NN) describes where they come from: the task to replicate the main feature of the human brain, i.e. the network of neurons. The hope was that a combination of the complex design of the brain and the technology of modern micro processors could combine the advantages of both: good pattern recognition capabilities and fast signal transmission.

An artificial neural network can be thought of as a sort of 'black box' processing system; its operational capabilities allow the reproduction of an application $X \to Y$ between two sets of vectors. In a neural network the basic units are called neurons. A neuron has several input and output connections, and the weighted sum of all the signals received by a neuron generates its activation

$$a_j = f_{\text{act}} \left(\sum_i w_i x_i + \theta_j \right) ,$$

x_i are the input values, w_i are the weights and θ_j is a threshold potential (see 5.4). The activation function g is very often chosen as a sigmoidal function such as

$$g(x) = \frac{1}{1 + e^{-x/T}} .$$

The constant T sets the gain of the activation function. The output o_j, the signal which is sent to the neighbouring cells, is calculated from the activation a_j by an output function

$$o_j = f_{\text{out}}(a_j) .$$

In the simplest case, the output function is the identity function, so that

$$o_j = f_{\text{out}}(a_j) \equiv a_j .$$

With this simple neuron, various types of networks and architectures can be built. One of the most widely used is the feed-forward, multilayer neural network with supervised training. In

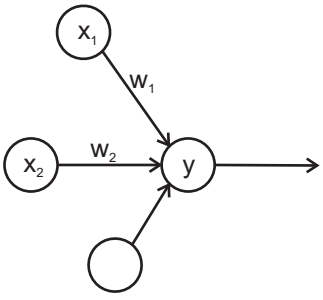

Figure 5.4: A simple neural network consisting of two input neurons, x_1 and x_2, with specific weights w_1 and w_2, and one output neuron y with a threshold θ.

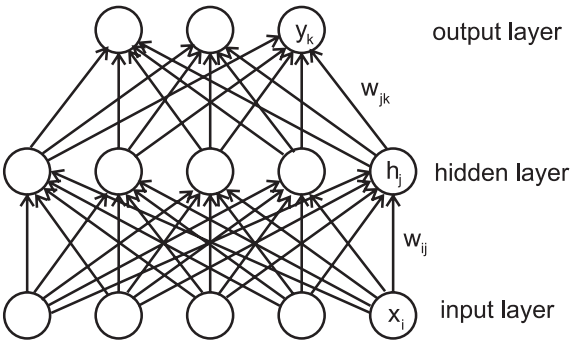

Figure 5.5: Schematic of a three layer feed-forward neural network.

this configuration the neurons are grouped in layers: an input layer, one or more hidden layers and an output layer. Each neuron is connected with all the neurons of adjacent layers, but no back-coupling links or links within the same layer are allowed (see fig. 5.5). In principle, one hidden layer is sufficient to fit any continuous function, but it may well be more practical to use a network with more than one hidden layer.

Once the weights are set in the training process, the network architecture is completely determined. There is a variety of training methods. In the present case I have used a method known as back-propagation. A set of Monte-Carlo simulated data is presented to the net with the corresponding output. For each input pattern the energy function is evaluated

$$E = \frac{1}{2N_p} \sum_{i=1}^{N_p} (O_i - T_i)^2$$

where O_i is the computed network output for the given pattern and T_i is the desired value (target) for the same pattern. The energy function is computed by the net and its value is propagated backwards to modify each weight. The updating function is

$$\Delta w_{ij}^{(k+1)} = -\eta \frac{\partial E}{\partial w_{ij}} + p\, \Delta w_{ij}^{(k)}$$

where $\Delta w_{ij}^{(k+1)}$ is the $(k+1)$st update of the weight w_{ij} and η is the learning parameter, representing the step length on the error surface that is defined by the value of the error as a function of all weights. The last term is a momentum term which stabilizes the training by avoiding oscillations. The strength of the damping is set by the parameter p which should be between 0 and 1. The updating of the weights can be done after each pattern, after a group of patterns or just once after the complete training set, called one epoch. The smaller the number of patterns the energy function is averaged over, the faster, but the more unstable, the training process can be. The training starts with randomly selected weights and relatively high values of the learning rate and the momentum; the factors are changed during the training over several thousands of epochs, until the error function reaches a minimum on a validation set, a Monte Carlo generated set different from the learning set.

It is important that the input variables are of the same order of magnitude and range in order to obtain stable convergence towards the minimum: the simplest method to obtain this is to renormalize the input variables to an interval $[0, 1]$. Furthermore, in order to avoid local minima, it is recommended to pick the input event at random from the simulated set, and, to prevent overfitting, to have the number of simulated learning patterns at least one order of magnitude higher than the number of weights in the net. The problem of overfitting arises when there are too many weights in the net with respect to the number of learning patterns, so that the net becomes very specialized in fitting only those patterns and loses its generalization capability.

For the NN computations the Fortran package JetNet 3.4 [Pet93] was used. A three-layer NN was chosen with a sigmoidal activation function having the output in the range $[0, 1]$. The training was performed using the back-propagation algorithm. The training was stopped when the error function behaviour became flat.

5.3 Results

5.3.1 Simulated Data

In a Monte Carlo simulation, 20 000 alpha and beta events were generated all over the Inner Vessel, with random energies from 0 to 3 MeV. Fig. 5.6 shows a typical simulated alpha and a beta pulse for the CTF2 geometry. The time spectrum recorded was binned in such a way to reproduce the flash ADC output (2.5 ns sampling time, 8 bit depth).

The input values for the NN were:

- 100 bins of the normalized flash ADC spectrum (250 ns);
- the radial distance from the center (reconstructed position), normalized to the Inner Vessel radius;
- the energy of the event, in MeV.

The NN had 102 neurons in the input layer, 102 neurons in the hidden layer, and 1 neuron in the output layer, giving $102 \times 102 + 102 = 10\,506$ weights w_{ij}. The output parameter of the net is called nn_β and can take values between 0 and 1. Ideally it should be 1 for beta events and 0 for alpha events. If nn_β is between 0 and 0.5, the event is classified as alpha event; if nn_β is larger than 0.5, the event is classified as beta event. The training set consisted of 8000 events. After each 10 events the weights were updated using the backpropagation algorithm. The validation set consisted of 8000 events (different from the training set). The results of the NN after 5000 generations are shown in in fig. 5.7 for events with energies greater than 0.2 MeV. From 3629 beta events only 46 were misidentified as alpha events. From 3607 alpha events 42 were misidentified as beta events. This means, that for 98.7 % beta identification efficiency, 98.8 % of the alpha events are rejected.

For a comparison I also calculated the tail-total-ratio from the flash ADC spectrum with the tail starting after 47.5 ns (see fig. 5.8). For the same beta identification efficiency (98.7 %) with this method, I also got the same alpha rejection efficiency (98.8 %).

The neural network has the same discrimination capability as the standard tail-to-total ratio, but it cannot beat this simpler and more straightforward technique.

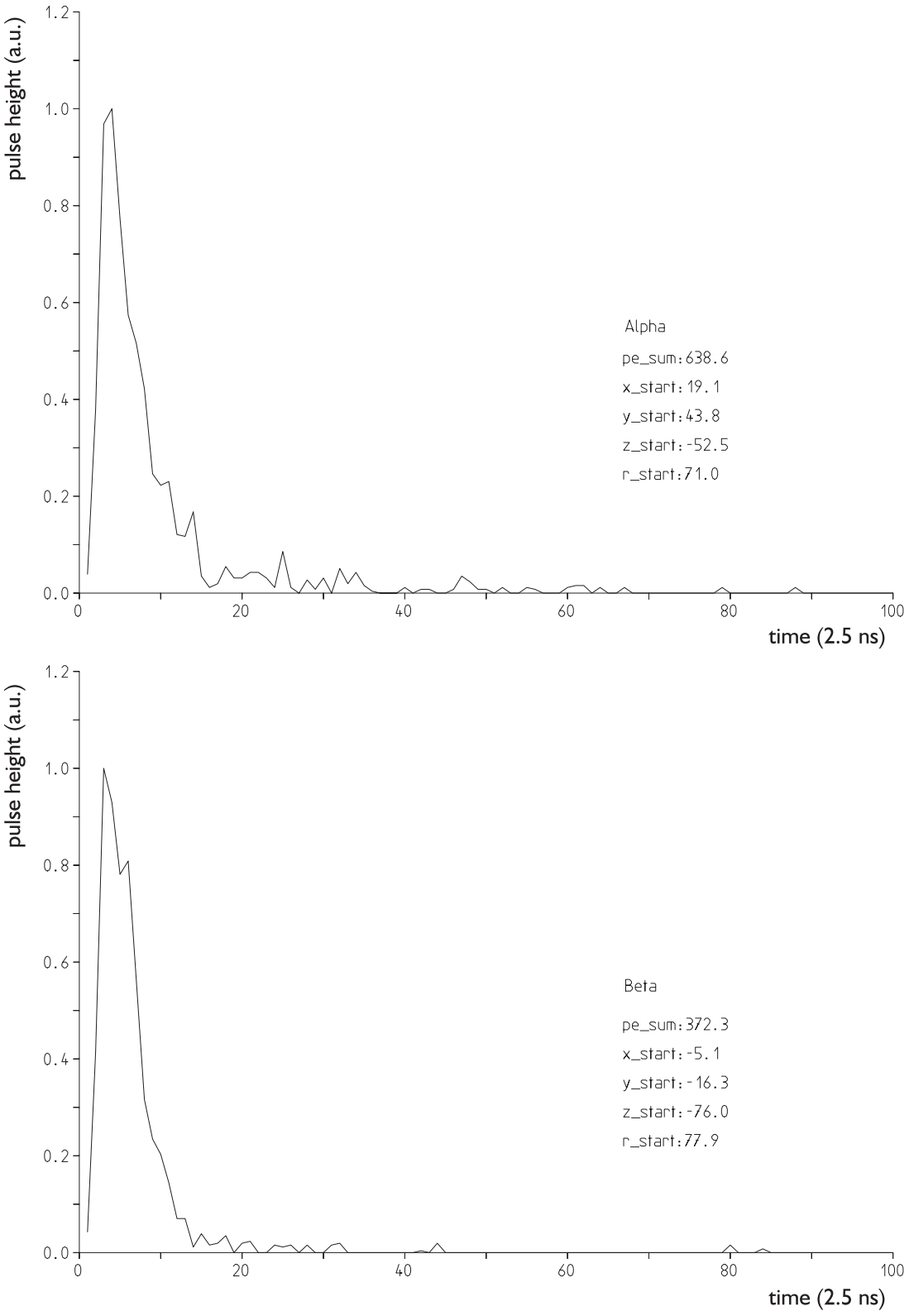

Figure 5.6: A simulated alpha and beta pulse in the CTF2.

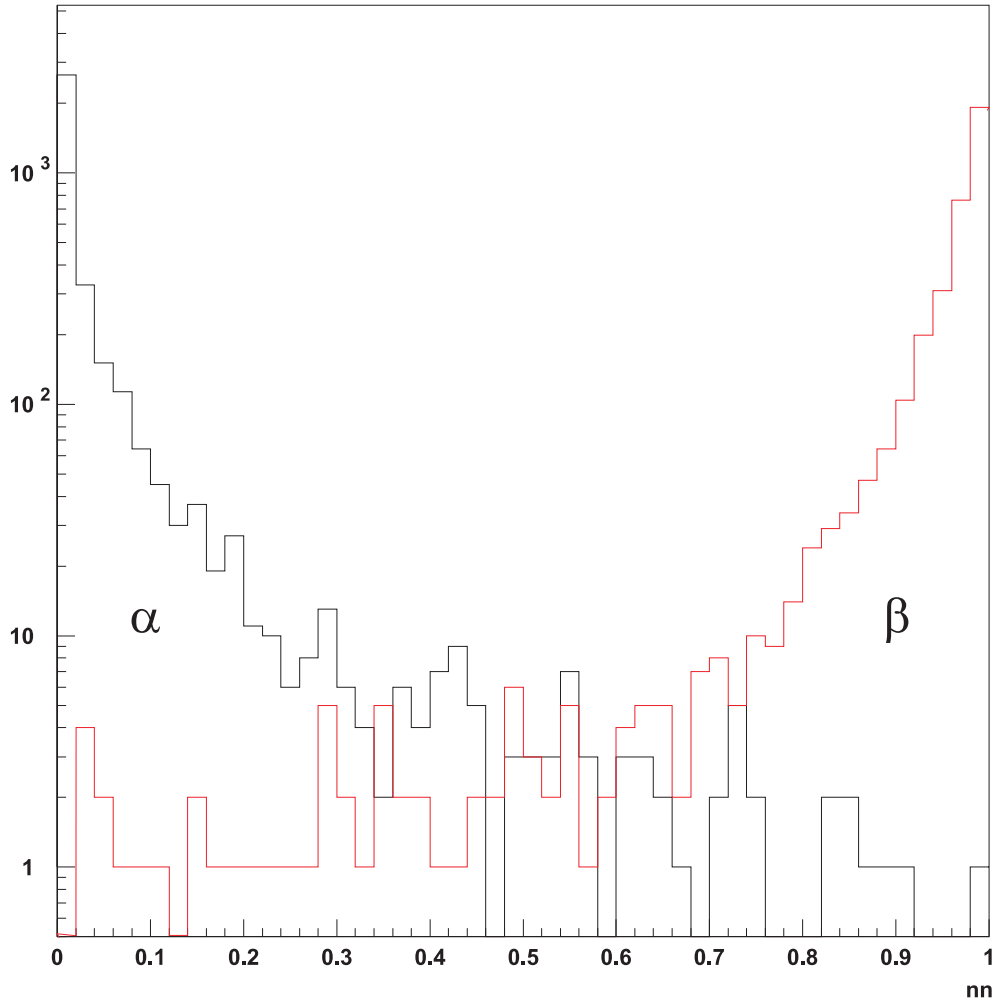

Figure 5.7: Alphabeta discrimination of MC events from the CTF2. The distribution of alpha events (solid line) and beta events (dashed line) is plotted versus the discrimination parameter nn, which was derived with a three-layer NN using the flash ADC spectrum as input.

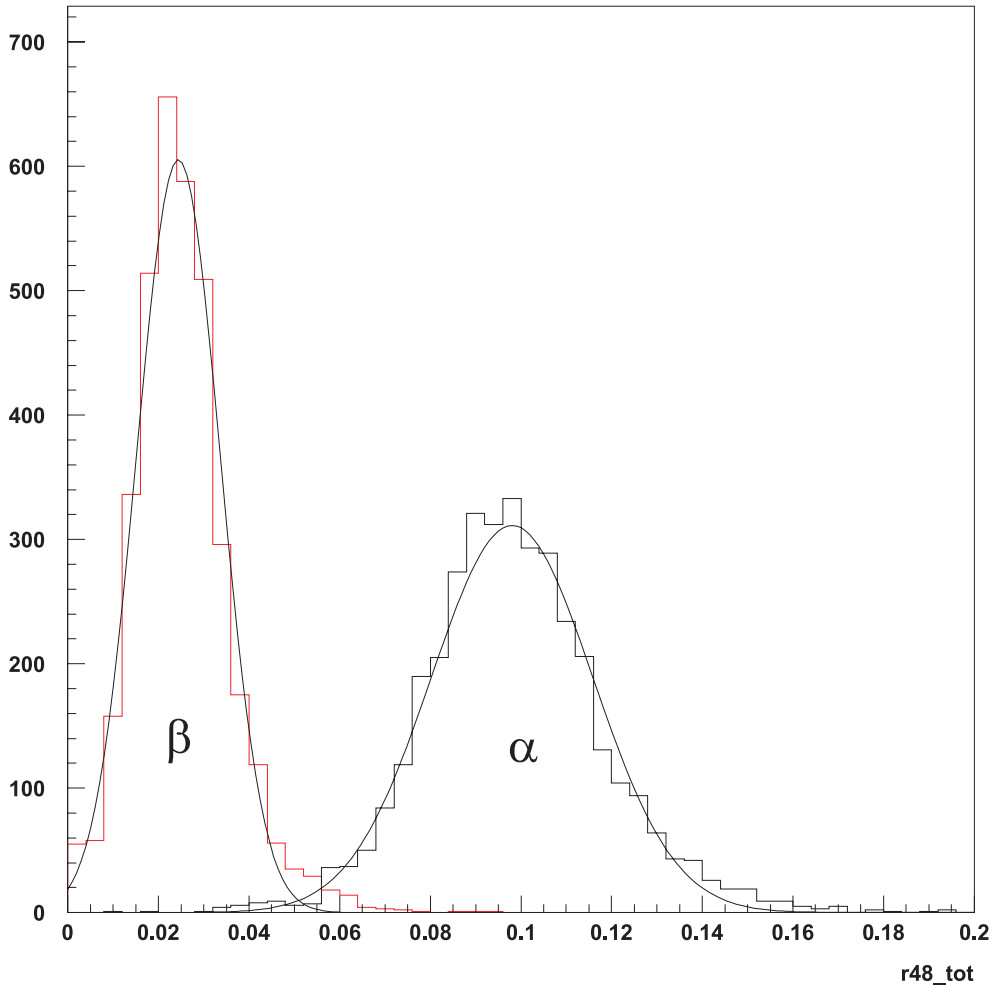

Figure 5.8: Alphabeta discrimination of MC events from the CTF2, using the tail-to-total ratio (tail starts at 47.5 ns) as discrimination parameter. The distribution of alpha events (solid line) and beta events (dashed line) is plotted versus the tail-to-total ratio r_{48_tot}.

5.3.2 Data from CTF2

I tested the neural network also with real CTF data to see if in the case of real, more noisy spectra the NN would be superior to the tail-to-total method. Not for all CTF2 runs flash ADC data are available. To have a sufficiently high statistics for the training of the net, I chose one of the source runs, run 793. In this run, all the ^{214}Bi and ^{214}Po events occurred at the same position, i.e. the center of the Inner Vessel. In this case, the pulse shape is not further broadened by the time of flight differences to the different PMTs, so that the pulse shape discrimination should yield better results than for randomly distributed events. Fig. 5.9 shows a typical ^{214}Bi beta and a ^{214}Po alpha pulse.

A total sample of 2360 events was available from run 793. The sample was too small to reduce it further by restricting the energy of the ^{214}Bi events to the same energy range as the ^{214}Po events, which would have been the case for only ~ 200 events. Giving the energy of the event as input parameter for the NN could lead to the unwanted case, that the NN uses the energy as decision criterium: high energy beta events, low energy alpha events. Hence I took as input parameter only the normalized flash ADC spectrum (100 bins = 250 ns). 1000 events were chosen as training set for the NN. The other 1360 events are the validation set.

The training process continued 5000 epochs, until the error function became flat. The results of the NN algorithm are shown in fig. 5.10. From 680 beta events only 26 were misidentified as alpha events. From 680 alpha events 22 were misidentified as beta events. This means, that for 96.2 % beta identification efficiency, 96.7 % of the alpha events are rejected.

For a comparison I tested the pulse shape discrimination using the tail-to-total ratio (with the tail starting after 48 ns) on the same data sample. For a beta identification efficiency of 96 %, an alpha rejection efficiency of 84.9 % is obtained (see fig. 5.11).

In this case, the neural network is clearly better than the simple tail-to-total ratio. These results are encouraging for BOREXINO, but data samples with a higher statistics and further systematic tests are needed.

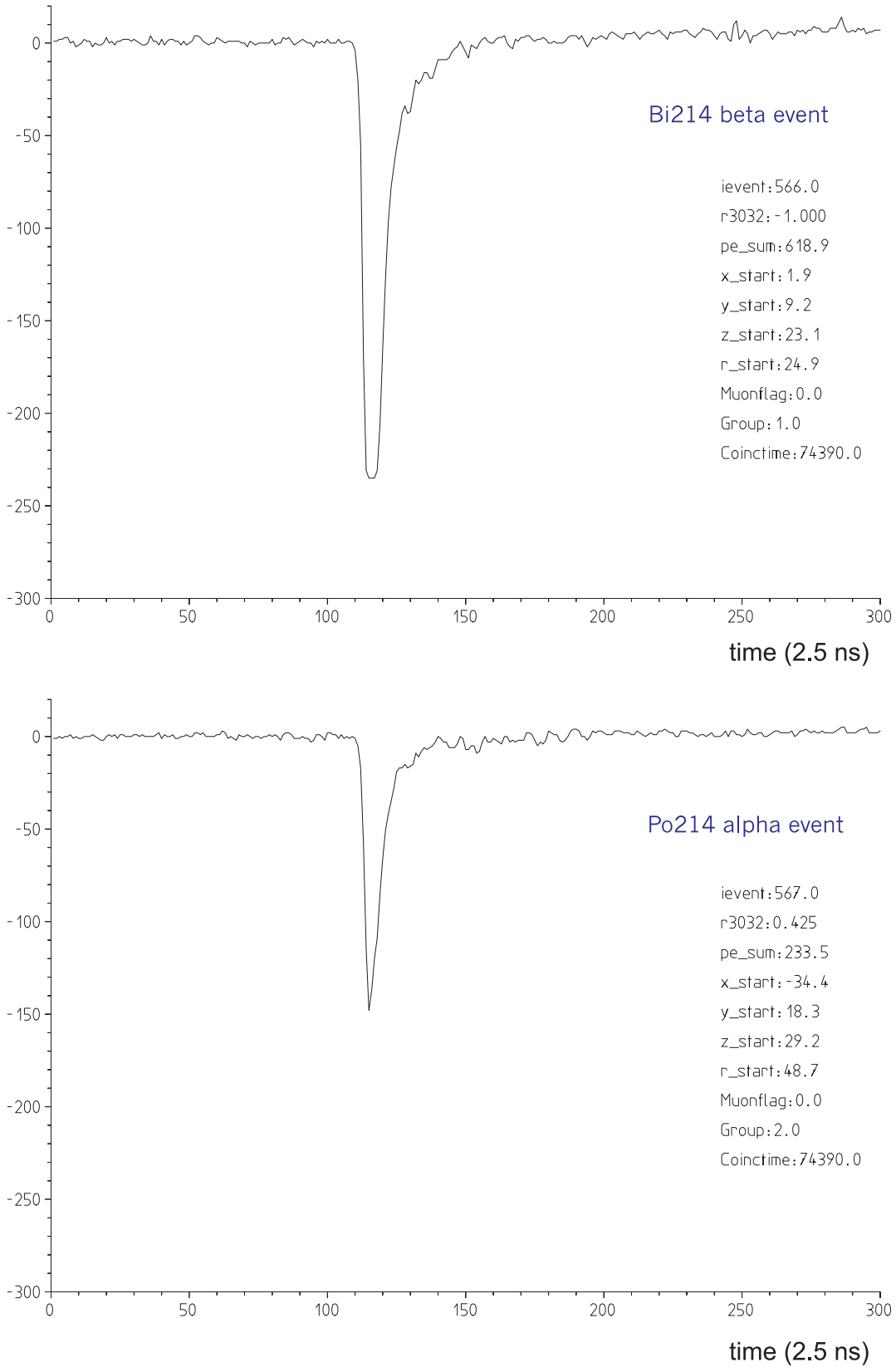

Figure 5.9: The flash ADC spectra of a typical ^{214}Bi beta and a ^{214}Po alpha pulse from run 793 (^{222}Rn source in the center).

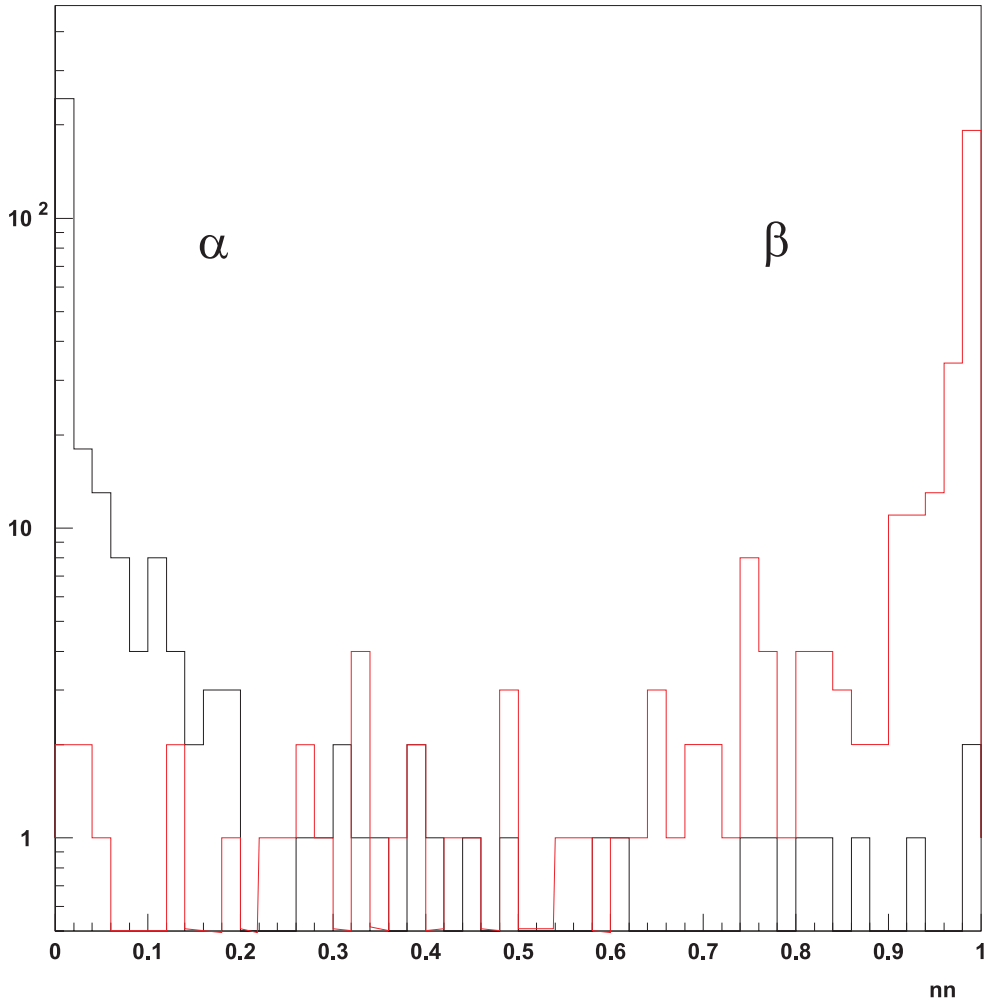

Figure 5.10: The result of the NN for run 793. The program was learning with only 1000 Bi-Po-events (due to limited statistics). The distribution of alpha events (solid line) and beta events (dashed line) is plotted versus the discrimination parameter nn.

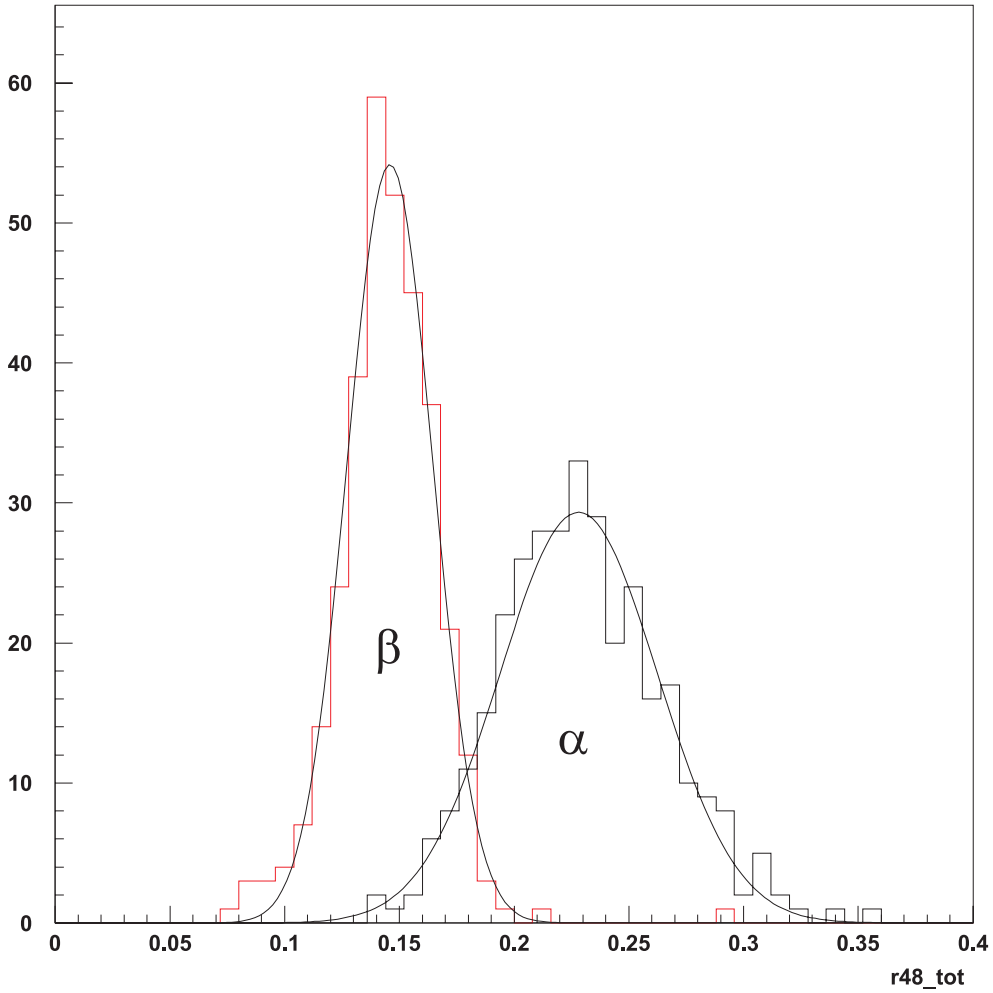

Figure 5.11: Pulse shape discrimination with the tail-to-total ratio (tail starting after 48 ns) for ^{214}Bi and ^{214}Po events from the source run 793. The distribution of alpha events (solid line) and beta events (dashed line) is plotted versus the tail-to-total ratio r_{48_tot}.

6 Test of a PXE based scintillator for Borexino

6.1 Motivation for an alternative scintillator

Initially, BOREXINO was going to use a PC based liquid scintillator ($\rho = 0.88\,\mathrm{g/cm}$) and a surrounding water buffer ($\rho = 1.0\,\mathrm{g/cm}$) [Bel91]. It turned out that the solution adopted for the scintillator containment vessel, namely a thin nylon membrane with 0.1 mm thickness, cannot hold a buoyancy force bigger than a few tons. Thus it became necessary to match the density of the scintillator and the buffer liquid within 1 %. There are two possible solutions to this problem:

- find a buffer medium whose density matches the density of PC and which is optical transparent, non-fluorescing and chemically inert (not attacking the nylon, steel, the concentrators or the PMTs);
- find a liquid scintillator with optical properties similar to PC and a density close to 1.0 g/cm, so that water can be used as buffer medium.

Considering the second strategy, a new scintillator based on PXE ($\rho = 0.985\,\mathrm{g/cm^3}$) was suggested by R. Raghavan [Rag95] and subsequently tested in laboratory measurements as well as in the CTF.

The main advantage of PXE compared to PC is its higher density. Taking a fixed detector geometry, a higher density means more target mass in the same volume, and, as the shielding against the external background is more efficient in a medium with higher density, the fiducial volume can be further increased, which additionally increases the target mass. Assuming the fixed volume of 321 m^3 for the scintillator, the mass of the PXE would be 316 t compared to 281 t for PC. Taking into account the electron densities, the signal rate would increase from 55 events per day to about 61 events per day in the same volume. For the shielding against the external background the higher density of the water buffer is also advantageous. For comparison, a simulation of the external gamma ray background induced by the radioactivity of the PMTs and concentrators was performed for the two scenarios: PC scintillator/PC buffer and PXE scintillator/water buffer. The contamination of the PMTs is: ^{232}Th 43,6 μg/piece, ^{238}U 127,9 μg/piece, ^{40}K 6,1 μg/piece. The contamination of the concentrators is: ^{232}Th 0.25 μg/g,

^{238}U and ^{40}K negligible. Table 6.1 shows the results of the simulation. Even without any radial cuts, the background is a factor of 3 - 4 lower for PXE/water than for PC/PC. Increasing the radius of the fiducial volume from 300 to 320 cm, which would give for PXE/water about the same background contribution than for PC/PC, would yield a 20 % higher target volume, or a 35 % higher target mass, which means that the ^{7}Be neutrino signal rate would increase from 55 events per day to about 75 events per day.

	250 - 800 keV		800 - 1400 keV	
Radius (cm)	**PC/PC counts/day**	**PXE/Water counts/day**	**PC/PC counts/day**	**PXE/Water counts/day**
< 300	0.22	0.05	1.1	0.13
< 325	1.15	0.30	4.9	0.71
< 350	8.5	1.8	23	4.8
< 375	66	14	103	25
< 400	434	109	386	105
< 425	1248	345	844	243
all	1921	455	1023	298

Table 6.1: Contribution of the PMTs and concentrators to the background in BOREXINO, placing the fiducial volume cut at different radii. From a Monte Carlo simulation for the two different scenarios: PC scintillator/ PC buffer, and PXE scintillator/ water buffer [Gri01].

6.2 Laboratory Measurements with PXE

6.2.1 Basic properties of PXE

For the use in a large scale low background experiment not only the optical properties and the radiopurity (which will be discussed in more detail later), but also other physical properties have an impact on the choice of the material. These are e.g. density (target mass, background shielding), flammability (safety) and viscosity (liquid handling). Also the cost, availability and legal classification of the material play an important role.

PXE and PC are both aromatic hydrocarbons, made up of similar molecular structures and with generally similar chemical properties. The molecular structure of the solvent and the fluor molecules of the scintillator mixtures under discussion are shown in fig. 6.1. The basic physical properties of PC and PXE are compared in table 6.2. PXE has a 10 % higher density than PC, whose advantages were already explained. PC is legally a hazardous material because of its flammability code (flammability class III). The transportation requirements are those of UN code 1993. PXE is not hazardous, and has no special UN hazard code or related transportation

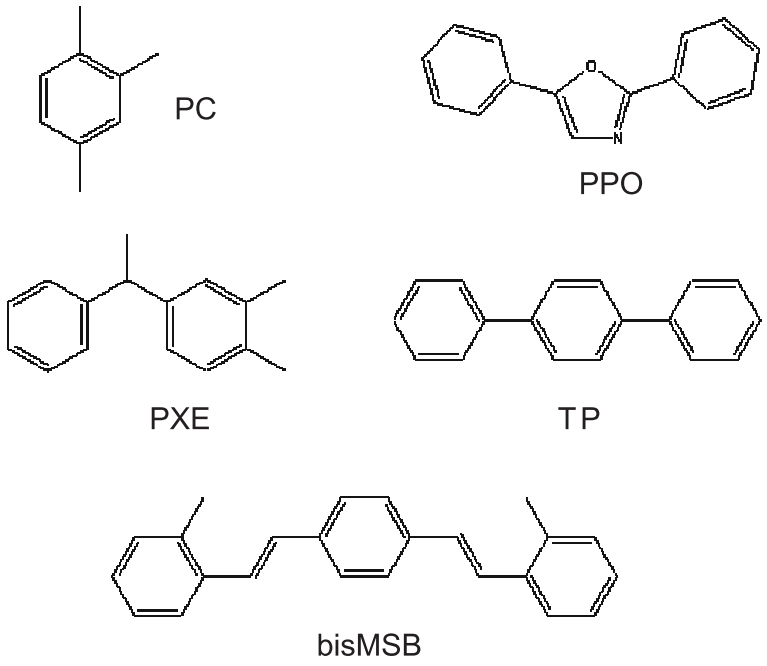

Figure 6.1: The molecular structure of the scintillator solvents (PC and PXE), fluors (TP and PPO) and wavelength shifter (bisMSB) under discussion.

restrictions. PXE has an about 20 times higher viscosity than PC resulting in higher demands on the capabilities of the liquid handling system (or lower flow rates).

Property	PC	PXE
sum formula	C_9H_{12}	$C_{16}H_{18}$
molecular weight	120.2	210.3
electrons per molecule	66	114
density	0.876 g/cm^3	0.985 g/cm^3
flash point	48 °C	145 °C
boiling point	169 °C	295 °C
vapor pressure @ 25 °C	2.03 mm Hg	0.01 mm Hg
refractive index n_D	1.505	1.565
viscosity @ 20 °C	0.8 cP	20 cP

Table 6.2: Comparison of the basic properties of the scintillator solvents PC and PXE. From [PXE94, PC999]

6.2.2 Optical Properties

The main characteristics used to describe the properties of an organic scintillator may be summarized as:

- the scintillation emission spectrum and the transmission of this spectrum through the scintillator;
- the variation of response with energy for different types of charged particle;
- the absolute scintillation efficiency, the response resolution and the associated energy resolution;
- the fast timing characteristics, including the time resolution and the parameters which describe the prompt component of the scintillation decay;
- the pulse shape characteristics, including the relative intensities of the prompt and the delayed scintillation components for different types of particle, and the suitability of these characteristics for particle identification by pulse shape discrimination.

Most of these items have been addressed in laboratory measurements [Eli96, Nef96, Lom97]:

- The emission spectrum of TP in PXE is shown in fig. 6.2.
- PXE/TP has a fluorescence lifetime of 3.2 ns, similar to PC/PPO (3.6 ns).
- The attenuation length of PXE/TP was measured to be 4.3 m at 430 nm (PC/PPO 3.3 m at 430 nm).

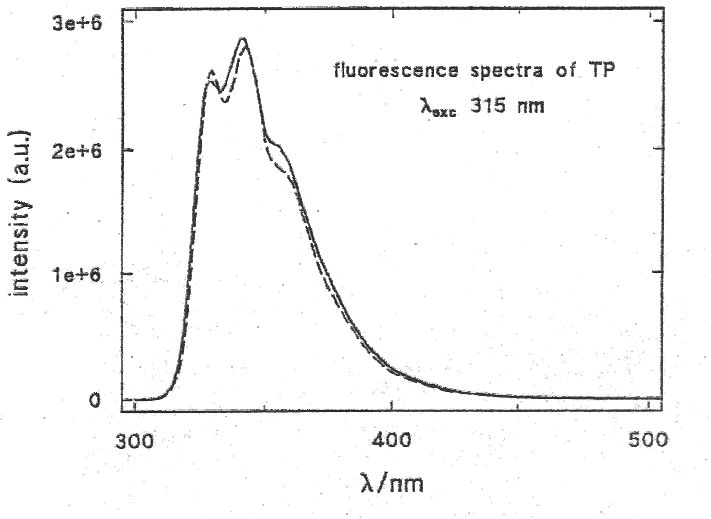

Figure 6.2: Fluorescence spectra of TP in PC (full line) and PXE (dashed line) under excitation at 315 nm. Taken from [Eli96].

- The light yield of PXE/TP is 0.68, slightly less than PC/PPO (0.73).

- The quenching factors of alpha particles were measured in small samples with ^{222}Rn spiked scintillator. These are listed in table 5.1 for PXE/TP and PC/PPO. The effect of alpha quenching is about 20 % weaker in PXE/TP than in PC/PPO, which means that the alpha peaks appear at somewhat higher energies.

- The α/β discrimination efficiencies of PXE/TP and PC/PPO under laboratory conditions are comparable. With the beta identification efficiency fixed at 98 %, the alpha identification efficiency is 99.7 % for PC/PPO and 98.4 % for PXE/TP/bisMSB in the energy range from 80 - 135 pe [Lom97].

6.2.3 Radiopurity

As PXE is a petroleum derivative like PC, similar radiopurity levels may be expected. PC is obtained directly from the fractional distillation of petroleum, while PXE requires further processing: the raw materials styrene and xylene are obtained from the fractional distillation of petroleum, and then react with each other. The product is washed with water and distilled a second time. After the distillation a solid column unit with clay is utilized at the plant, mainly to remove residual water dissolved in the PXE. These further process steps introduce considerable optical and inorganic impurity levels. Therefore, R. Raghavan suggested the implementation of the solid column chromatography (or gel filtration) within BOREXINO, as opposed to using the one at the plant, so that we could control this step by ourselves. In laboratory experiments he found that silica gel would suit this purpose well.

Column chromatography with silica gel is a commonly used technique for the cleaning of liquids. Silica gel is a powder with highly porous grains (grain size several 100 μm, pore size few nm), offering a large contact surface (several $100\mathrm{m}^2/\mathrm{g}$). The surface consists of reactive silanol groups (Si-OH). Ionized and polarizable impurities in the liquid are removed by surface adsorption, while the nonpolar scintillator molecules are unaffected. The fine powder structure of the silica gel also has a filter action on particulates.

Laboratory tests of the column purification with PXE/TP together with neutron activation [Gol97] showed a clear reduction of the concentration of almost all impurities in the liquid scintillator, which are of concern for BOREXINO (see table 6.3). These results made us confident to build a large column (volume ~ 80 l) for the purification of several tons of scintillator, to test this cleaning procedure in the CTF.

Commercially available silica gel has a rather high intrinsic ^{238}U concentration (10^{-8} g/g), so that the Rn emanation from the silica gel itself becomes a problem, as this leads to high concentrations of the long-lived ^{222}Rn daughters in the scintillator. Thus, we were looking for a supplier of high purity silica gel or the possibility to fabricate high purity silica gel by ourselves starting with cleaner raw materials [Ang97]. The ^{226}Ra activity and ^{222}Rn emanation

Element	PXE + TP, concentration in g/g		purification factor
	before purification	after purification	
Cd	$4 \cdot 10^{-12}$	$\leq 1.1 \cdot 10^{-12}$	≥ 4
Cr	$2 \cdot 10^{-9}$	$2.7 \cdot 10^{-12}$	$7 \cdot 10^{2}$
Fe	$1.4 \cdot 10^{-8}$	$\leq 4.0 \cdot 10^{-11}$	$\geq 3.5 \cdot 10^{2}$
In	$\leq 4.7 \cdot 10^{-12}$	$\leq 1.6 \cdot 10^{-12}$	-
K	$6 \cdot 10^{-9}$	$5.9 \cdot 10^{-11}$	$1 \cdot 10^{2}$
La	$1.6 \cdot 10^{-12}$	$7.7 \cdot 10^{-15}$	$2 \cdot 10^{2}$
Lu	$1 \cdot 10^{-15}$	$\leq 8.0 \cdot 10^{-16}$	≥ 1.5
Na	$3 \cdot 10^{-9}$	$3.7 \cdot 10^{-11}$	$8 \cdot 10^{1}$
Rb	$\leq 7.2 \cdot 10^{-12}$	$\leq 7.9 \cdot 10^{-14}$	$\geq 9 \cdot 10^{1}$
U	$5 \cdot 10^{-14}$	$5.0 \cdot 10^{-15}$	$1 \cdot 10^{1}$
Th	$7 \cdot 10^{-14}$	$\leq 8.0 \cdot 10^{-15}$	≥ 8
W	$7 \cdot 10^{-12}$	$\leq 7.9 \cdot 10^{-14}$	$\geq 9 \cdot 10^{1}$
Zn	$4 \cdot 10^{-9}$	$9.3 \cdot 10^{-11}$	$4 \cdot 10^{1}$

Table 6.3: Purification factors for solid column chromatography on PXE/TP, obtained from a laboratory test with a 20 ml column. From [Gol97].

rate of several samples of commercially available silica gel are shown in table 6.4. The ^{222}Rn emanation of the high purity silica gel from Eka Nobel was below the detection limit, and hence it was chosen for the use within BOREXINO. To avoid the contamination of the scintillator with long-lived ^{222}Rn daughters, the scintillator is purged with nitrogen gas directly after the column to remove the ^{222}Rn before it decays in the scintillator (see fig. 6.4).

silica gel sample	^{226}Ra activity (Bq/kg)	^{222}Rn emanation (Bq/kg)
Merck, 0.2 - 0.5 mm, 60 A	2.28 ± 0.11	200 ± 10
Roth, 2 - 4 mm	0.9 ± 0.2	410 ± 60
Eka Nobel, Kromasil, $1 - 20\,\mu$m	< 0.09	< 3.9

Table 6.4: ^{226}Ra activity and ^{222}Rn emanation of different samples of commercially available silica gel [Rau99]. The silica gel from Merck was used in the CTF1. The silica gel from Eka Nobel was used in the CTF2 and will be used for BOREXINO.

6.3 The PXE Tests in the CTF

6.3.1 The liquid handling system Module-0 and the column plant

For the scintillator and fluor preparation and first filling of the CTF1 in 1995 a temporary liquid handling system had been installed by the Munich group. In context with the development of a solid column purification plant the temporary system was replaced by Module-0, the first modular part of the BOREXINO liquid handling system. It was originally constructed in 1996, and upgraded during 1998 and 1999. Module-0 serves as a flexible liquid handling unit for various filling and purification operations for BOREXINO and the CTF:

- volumetric loading and unloading of liquid scintillator to/from the CTF Inner Vessel;
- fluor mixing;
- purification of liquid scintillator with a silica gel column;

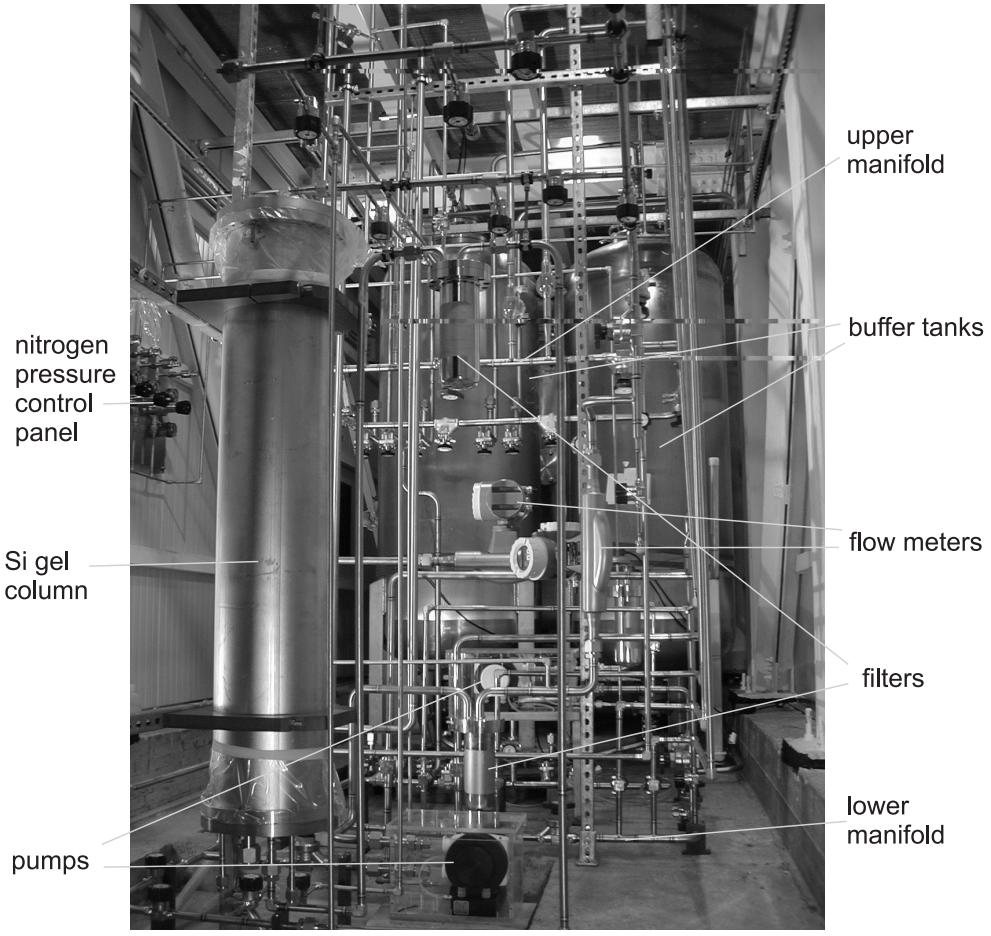

Figure 6.3: View of the module-0.

- Rn degassing of liquid scintillator;
- water extraction of liquid scintillator.

Module-0 comprises two 7 ton storage tanks (EP tanks), two 1 ton process tanks (buffer tanks), equipped with nitrogen spargers at the bottom and spray nozzles at the top (for a turbulent injection of liquid together with nitrogen gas, e.g. for a water extraction), two bellows teflon pumps, two flowmeters, several Millipore filters (0.5, 0.1 and 0.05 micron) and one 70 l column purification unit (see fig. 6.3). For BOREXINO a second column is planned which can be operated in parallel or in line with the existing one. All the parts are connected to the upper and the lower manifold of the Module-0, which are linked by several bridges. This design allows a maximal flexibility of the flow path. All tanks, tubes, valves and filter housings are made up of electropolished stainless steel, the pumps and filters are made from teflon. Connections to the CTF Inner Vessel, the water plant, and the nitrogen plant are provided; foreseen are connections to the BOREXINO storage area, buffer and Inner Vessel. A detailed description of the system can be found in [Sch99c], [Har97].

The column consists of a large electropolished chamber of 1.5 m length and 25 cm diameter. At the bottom is a filter plate with 14 teflon filter elements (47 mm), that are sandwiched between two stainless steel plates with an array of machined holes (0.5 cm diameter). The column has operated with an inlet pressure from 2.5 to 3.5 bar and flow rates of up to 1 ton

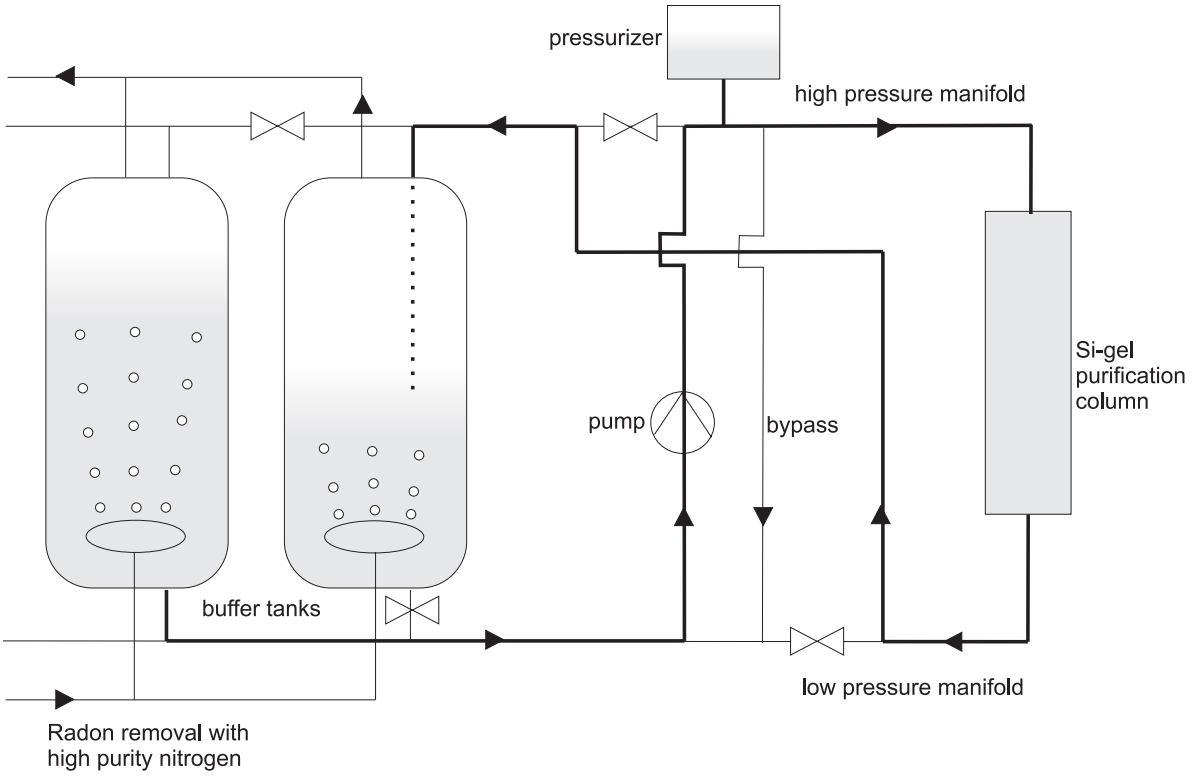

Figure 6.4: Sketch of the column purification process with following ^{222}Rn degassing.

per hour. Column flow control is via a negative feedback arrangement with a pressurizer and a bypass line: as pressure forces fluid into the column, the level in the pressurizer drops and the isolated gas volume above this level expands. The pressure of the upper manifold drops, the pressure-driven pump speeds up, the flow increases and the pressurizer level rises. The column flow is adjusted by the pressure difference between upper and lower manifold, which is set by the bypass flow. Fig. 6.4 shows the flow path for the batch column purification with subsequent nitrogen sparging for a prompt removal of the ^{222}Rn introduced in the scintillator by emanation of the silica gel.

6.3.2 PXE Test in the CTF1 1996 - 1997

The PXE scintillator was bought 1996 from Koch Chemical in Corpus Christi (Texas, USA) and shipped to Italy in three specially modified stainless steel containers, 2 tons each (Hoover transport tanks). At Gran Sasso the transport tanks were connected to the Module-0, and the scintillator was pumped into one 7 ton tank. The fluor para-terphenyl (2 g/l) and the wavelength shifter bisMSB (20 mg/l) were dissolved in the PXE by circulating it over the column, which was loaded with the fluor and wavelength shifter (powder). After this preparation the scintillator mixture was passing once over a 40 l silica gel column, and once over a 25 l silica gel column before it was filled into the CTF. During the CTF1 operation, the scintillator was circulated about two times over a 40 l silica gel column, and about five times through a 0.05 μm teflon filter.

At this time, the CTF had a reduced sensitivity: at the beginning of the PXE test 36 PMTs were working, at the end only 17 PMTs. The ^{238}U and ^{232}Th analysis from the CTF1 data and the corresponding NAA results are summarized in table 6.5. Samples for the NAA were taken at several times during the scintillator preparation and purification process. It has to be noted that in the CTF the coincidences ^{214}Bi-^{214}Po and ^{212}Bi-^{212}Po are measured, which are

period	^{238}U [10^{-15} g/g]		^{232}Th [10^{-15} g/g]	
	CTF	NAA	CTF	NAA
PXE as delivered	–	(32 ± 16)	–	(27 ± 15)
after first column	(1.8 ± 0.1)	(1.4 ± 0.7)	(2.9 ± 0.6)	(5.0 ± 2.5)
after second column	(1.0 ± 0.4)	< 0.6	(2.4 ± 0.5)	< 3
after filtration	(1.2 ± 0.1)	–	(1.7 ± 0.3)	–
after water extr.	–	< 0.25	–	(0.25 ± 0.07)
after third column	–	< 0.01	–	< 0.18

Table 6.5: The ^{238}U and ^{232}Th content in PXE after several purification steps, measured with two independent methods, the CTF and NAA (see text).

in equilibrium with their progenitors ^{226}Ra ($t_{1/2} = 1600$ a) and ^{228}Th ($t_{1/2} = 1.9$ a), while the NAA directly measures the parent isotopes ^{238}U and ^{232}Th. Only in the case of secular equilibrium both methods would yield the same results. The uranium measurement in the CTF could be affected by a significant background coming from ^{222}Rn in the water, that permeates through the nylon barrier (a very precise evaluation of this background is not possible; it might have as well reached a level of $1 \cdot 10^{-15}$ g^{238}U/g). The thorium measurement is not affected by such a kind of background. As can be seen from table 6.5, the values measured in the CTF1 and with NAA are compatible with secular equilibrium in both decay chains.

After the scintillator had been unloaded from the CTF, we continued the purification tests in the Module-0 with a water extraction of the 5 tons of scintillator with 2 tons of deionized water, and subsequently a circulation over a 40 l column (about 6 times the total volume). After each purification step a sample was taken for the NAA. In the end, a new record limit for the ^{238}U and ^{232}Th concentration in PXE was measured [vH99]:

$$\begin{aligned} c(^{238}\mathrm{U}) &< 1 \times 10^{-17}\,\mathrm{g/g} \\ c(^{232}\mathrm{Th}) &< 1.8 \times 10^{-16}\,\mathrm{g/g}\,. \end{aligned}$$

After these operations the scintillator was stored in one of the EP tanks, while the CTF and Module-0 were dismounted and upgraded during the years 1998 and 1999.

6.3.3 The PXE Test in the CTF2 2000

The PXE test in the CTF2 was carried out from May to September 2000. For the filling operations the upgraded Module-0 was used which also allowed to test this system for its performance and leak tightness.

The PXE scintillator, that had been used for the test in CTF1 in 1996, was stored underground in one 7-ton tank of Module-0 during the last years and was used again for the new test in CTF2. The scintillator composition was $\mathrm{PXE} + \mathrm{TP}(2.0\,\mathrm{g/l}) + \mathrm{bisMSB}(20\,\mathrm{mg/l})$. As the exact status of the scintillator was unknown (the tank had been opened several times during the last years to change flanges and sealings, and to connect the new pipes), we decided to clean the whole scintillator by running it in batches over a 40 l Silica gel column. The Silica gel was preconditioned by heating it up to about 100 °C and flushing it continuously with nitrogen for about 15 h to remove adsorbed water. The column operation needed about 1 day per ton scintillator. The scintillator was continuously running over the column with a flow rate of 1.5 - 2.5 l/min and from there into one of the two 1-ton-buffer-tanks, where it was flushed with nitrogen (RN_2) to remove the ^{222}Rn introduced by Rn-emanation from the silica gel (see fig. 6.4). Once one of the buffer tanks was completely filled, the nitrogen flushing was continued for several hours with high purity nitrogen ($< 10\,\mu\mathrm{Bq/m^3}$). For the filling the remaining gas volume at the top of the buffer tank was filled up with deionized water, then the tank was connected to the CTF Inner Vessel and the scintillator was pumped into the Inner Vessel by

volumetric exchange with water from the Inner Vessel. To avoid overpressure of the Inner Vessel, a few 100 l water were pumped out of the Inner Vessel prior to the filling. During the filling the pump was working in a mode, that it pumped water out of the Inner Vessel into the buffer tank, and the scintillator was pushed in a passive mode out of the buffer tank into the Inner Vessel. Once the filling was completed, the Inner Vessel was isolated, and the water was drained from the buffer tank. Then the tank was dried with nitrogen and was then ready to be filled again with the next batch of scintillator. The filling of the total volume of PXE (4 tons) was realized in three batches (1 ton, 2 tons, 1 ton). The data taking with the CTF2 can be divided into 5 different phases:

1. **Water Run**: The data acquisition was first running from March 19 to March 31 (run 706 - 716). At that time, the Inner Vessel was filled with water. These runs were used to calibrate the electronics; and, by measuring the Cerenkov light from muons crossing the detector, to develop criteria to reject these Cerenkov events.

2. **1 Ton Runs**: The first ton of PXE was filled in the CTF on June 3rd 2000. The Inner Vessel used in the CTF2 had several small leaks bearing the risk of enlarging under stress. Therefore we filled only 1 ton of PXE in the beginning in order to keep the buoyancy small. Data was taken from June 4th to June 9th (run 717 - 723). After it turned out that there were no substantial leaks, we continued the filling.

3. **3 Ton Runs**: Another $\sim 2\,\mathrm{m}^3$ were inserted in the IV on June 11th 2000. Data was taken from June 13th until July 15th (run 724 - 757).

4. **4 Ton Runs**: The remaining amount of PXE was inserted on July 15th 2000. The data taking period with 4 tons of PXE, without any scintillator operations, lasted from 16th July 2000 until 6th September 2000, i.e. about 6 weeks in total (run 758 - 789).

5. **Source Test**: From September 12 until September 20 we carried out a number of calibration measurements with a localized source introduced into the Inner Vessel (run 790 -810). The source was placed at various locations inside the Inner Vessel to test the homogeneity of the detector response and the systematic effects of the position reconstruction. The results of these tests will be reported in chapter 7.

At the end of September 2000, the scintillator was unloaded from the Inner Vessel into one EP tank by volumetric exchange with water. Later, the PXE was removed from the Module-0 and placed into storage for later use in another experiment. The water was drained from the CTF tank so that the leaky Inner Vessel could be replaced.

6.3.4 Results concerning the Radiopurity

^{14}C Concentration

In the energy region below 150 keV, the counting rate is dominated by ^{14}C. The ^{14}C concentration in the scintillator can be determined by fitting a convolution of the theoretical beta spectrum and the energy dependent detector response plus a background contribution to the measured spectrum (see fig. 6.5). From this fit, the following ^{14}C concentration was derived [Res01]:

$$\frac{^{14}\mathrm{C}}{^{12}\mathrm{C}} = (11.74 \pm 0.03)\, 10^{-18}\ .$$

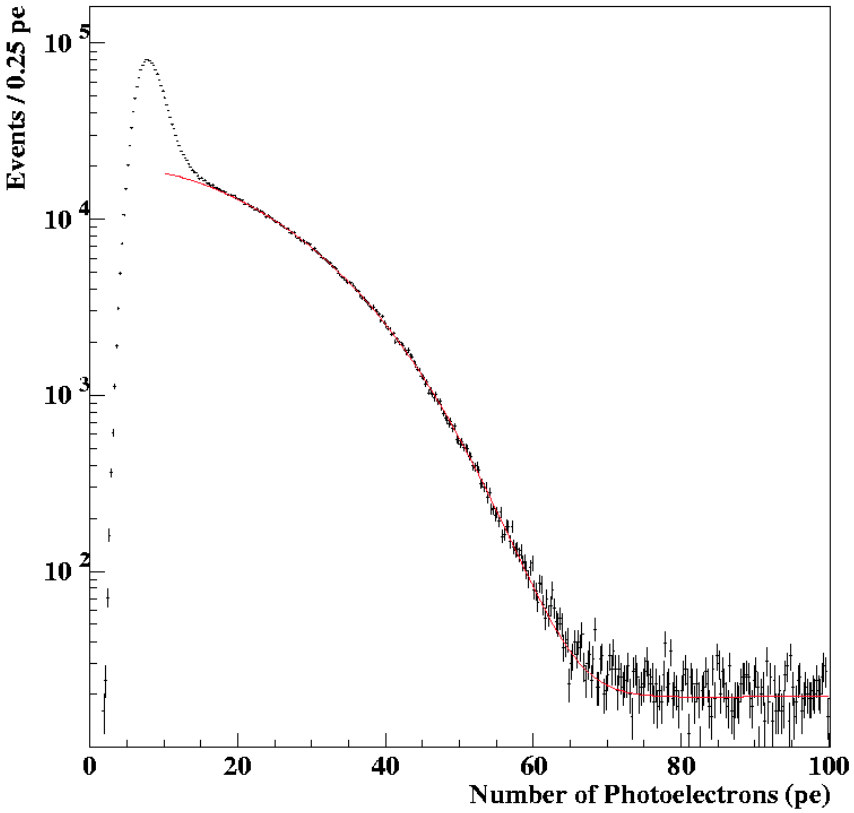

Figure 6.5: PXE data collected in a period of 153 hours with a fit of the ^{14}C spectrum. Taken from [Res01].

Limit on ^{238}U

In the CTF ^{238}U is assayed via the characteristic delayed coincidence between the decays of its daughters ^{214}Bi and ^{214}Po(half life of ^{214}Po: 164 μs). Assuming secular equilibrium of the whole decay chain, the measured decay rate of these daughters can be expressed as uranium-equivalent,

$$\mathrm{A} = 1\,\mathrm{count}/(\mathrm{day}\cdot\mathrm{ton}) \quad \Rightarrow \quad \mathrm{c}(^{238}\mathrm{U}) = \frac{\mathrm{A}\cdot\mathrm{M}}{\lambda\cdot\mathrm{N_A}} \simeq 9.4\cdot 10^{-16}\,\mathrm{g/g}$$

where A is the measured activity, $\lambda = 1.55\cdot 10^{-10}\,\mathrm{a}^{-1}$ is the decay constant of ^{238}U, M = 238 g/mol the molar mass, and $\mathrm{N_A}$ Avogadro's number.

Data taking with 4 tons of PXE lasted 52 days. The initial ^{222}Rn contamination was small (90 counts per day), so that the ^{222}Rn introduced during the filling should have decayed away (to a level of 1 count per day) within 4 weeks. We observed, however, after an initial decrease a constant ^{222}Rn activity of about 1 count per hour (see fig. 6.6). Moreover, this activity was not uniformly distributed, but peaked around the vertical axis (see fig. 6.7). Along the vertical axis, the distribution was not homogeneous in time, but seemed to be slowly moving downwards, while twice some new activity was introduced from the top (fig. 6.8). One possible explanation could be, that at the end of the volumetric filling, we reintroduced some water at the top of the Inner Vessel. As the densities of PXE and water are very close, the water droplets would move downwards only very slowly. Some droplets could stay attached to the tube walls and detach only occasionally, e.g. because of vibrations. As the activity in this 'column' around the z-axis was almost 1 count per hour, the specific activity of a ~ 0.01 l water droplet accounting for the whole ^{222}Rn activity would have to be $\sim 30\,\mathrm{Bq/m^3}$. However, the ^{222}Rn and ^{226}Ra activity in the CTF water were measured to be $\sim$30 mBq/m^3 and $\sim$3 mBq/m^3 respectively [Sim00], so that this theory can be ruled out. The nature of the ^{222}Rn contamination is still unknown. A systematic effect of the position reconstruction could be excluded by the source

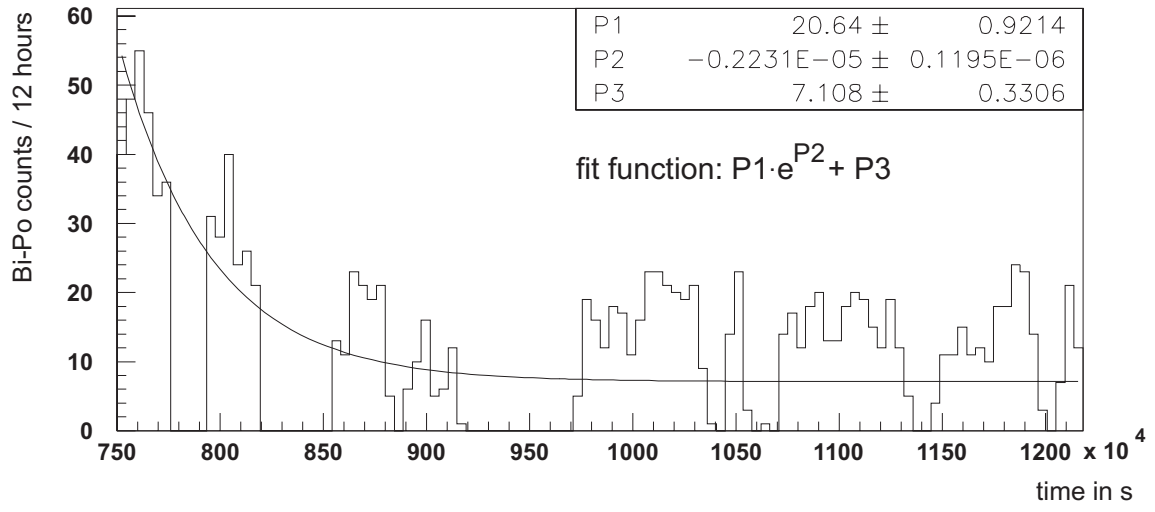

Figure 6.6: ^{222}Rn activity versus time for the runs 758 - 789.

measurements, as will be shown in chapter 7.
Applying a radial cut on the ^{214}Bi-^{214}Po event distribution, we could derive an upper limit for the intrinsic ^{238}U contamination. For the analysis, I took two periods at the end of the 4 ton runs: run 773 - 780 (7.32 days, August 21 - 29), and run 783 - 789 (6.98 days, August 31 - September 8).
The following cuts were applied to select the ^{214}Bi-^{214}Po events:

- energy of the group 1 event: more than 100 pe (efficiency > 95 %);
- energy of the group 2 event: between 200 pe and 400 pe (efficiency >99 %);
- coincidence time between 5 μs and 800 μs (efficiency 94%).

Two further cuts served to reject events originating from cosmic ray muons:

- the muon veto must not have triggered (no muonflag);
- the meantime (i.e. the average time of all hit PMTs) must be below 25 ns.

With these two cuts, muon events can be discriminated with a high efficiency while scintillation events are not affected.

A varying radial cut around the z-axis was applied to reject the events inside the column. The efficiency of this cut together with the results obtained are listed in table 6.6. The best value obtained is

$$\mathrm{c}(^{238}\mathrm{U}) = (1.7 \pm 0.4) \cdot 10^{-15}\,\mathrm{g/g}$$

for a cylindrical cut around the z-axis $\mathrm{R} > 0.6\,\mathrm{m}$.

radius (m)	mass (t)	run773 - 780		run 783 - 789	
		no. of events	^{238}U equiv. (10^{-15} g/g)	no. of events	^{238}U equiv. (10^{-15} g/g)
> 0.2	3.94	121	4.4 ± 0.4	101	4.1 ± 0.4
> 0.3	3.64	79	3.1 ± 0.3	59	2.4 ± 0.3
> 0.4	3.22	55	2.4 ± 0.3	41	1.9 ± 0.3
> 0.5	2.72	42	2.3 ± 0.4	32	1.8 ± 0.3
> 0.6	2.14	31	2.1 ± 0.4	24	1.7 ± 0.4
> 0.7	1.53	26	2.4 ± 0.5	17	1.7 ± 0.4

Table 6.6: Result of the ^{238}U analysis after the application of different cylindrical cuts around the z-axis. The errors given are statistical errors only.

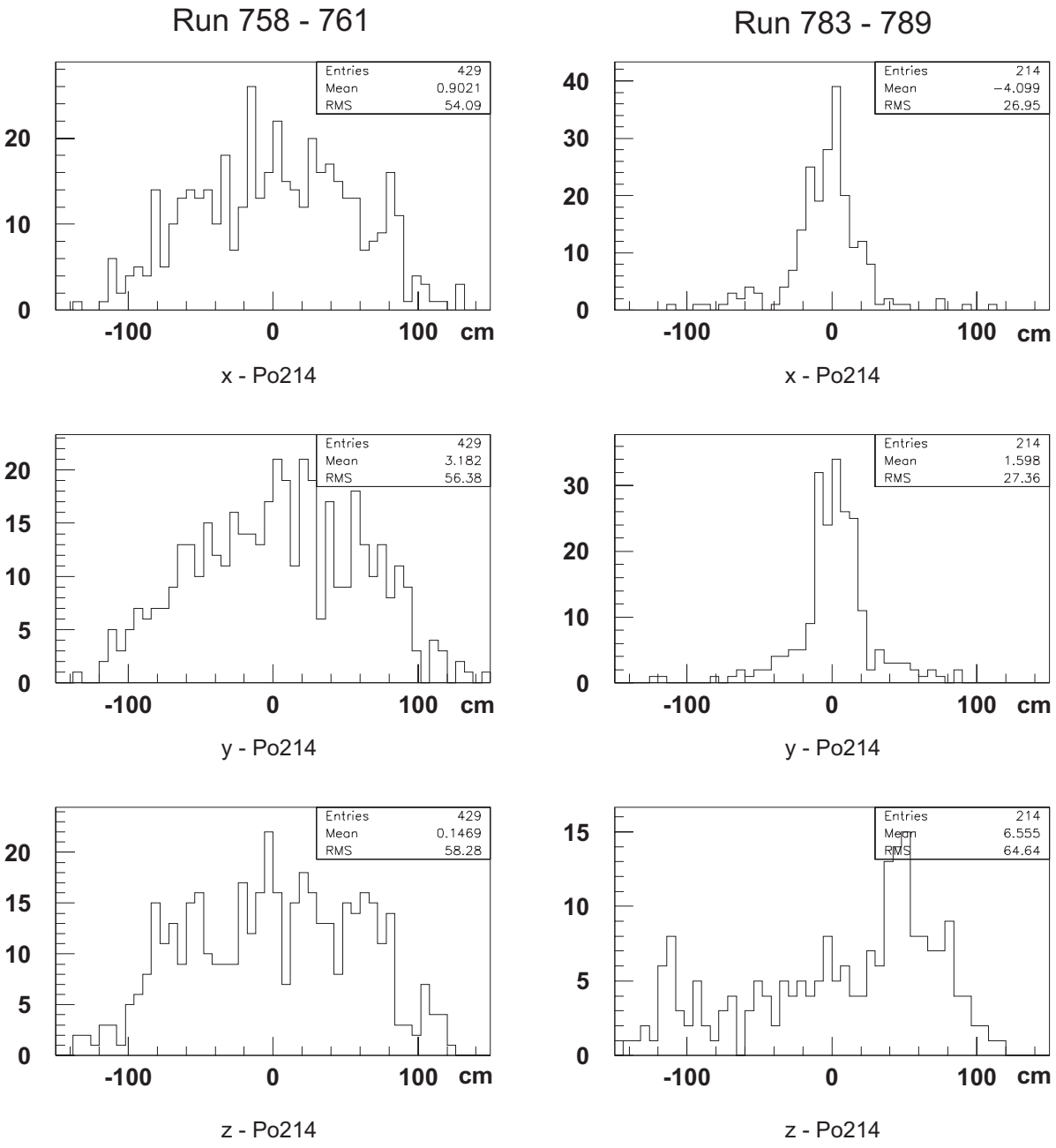

Figure 6.7: Reconstructed position of the ^{214}Po events for the runs 758 - 761 and 783 - 789. During run 758 - 761 the ^{222}Rn was distributed uniformly in the Inner Vessel, whereas during the later runs, it appears to be centered around the z-axis.

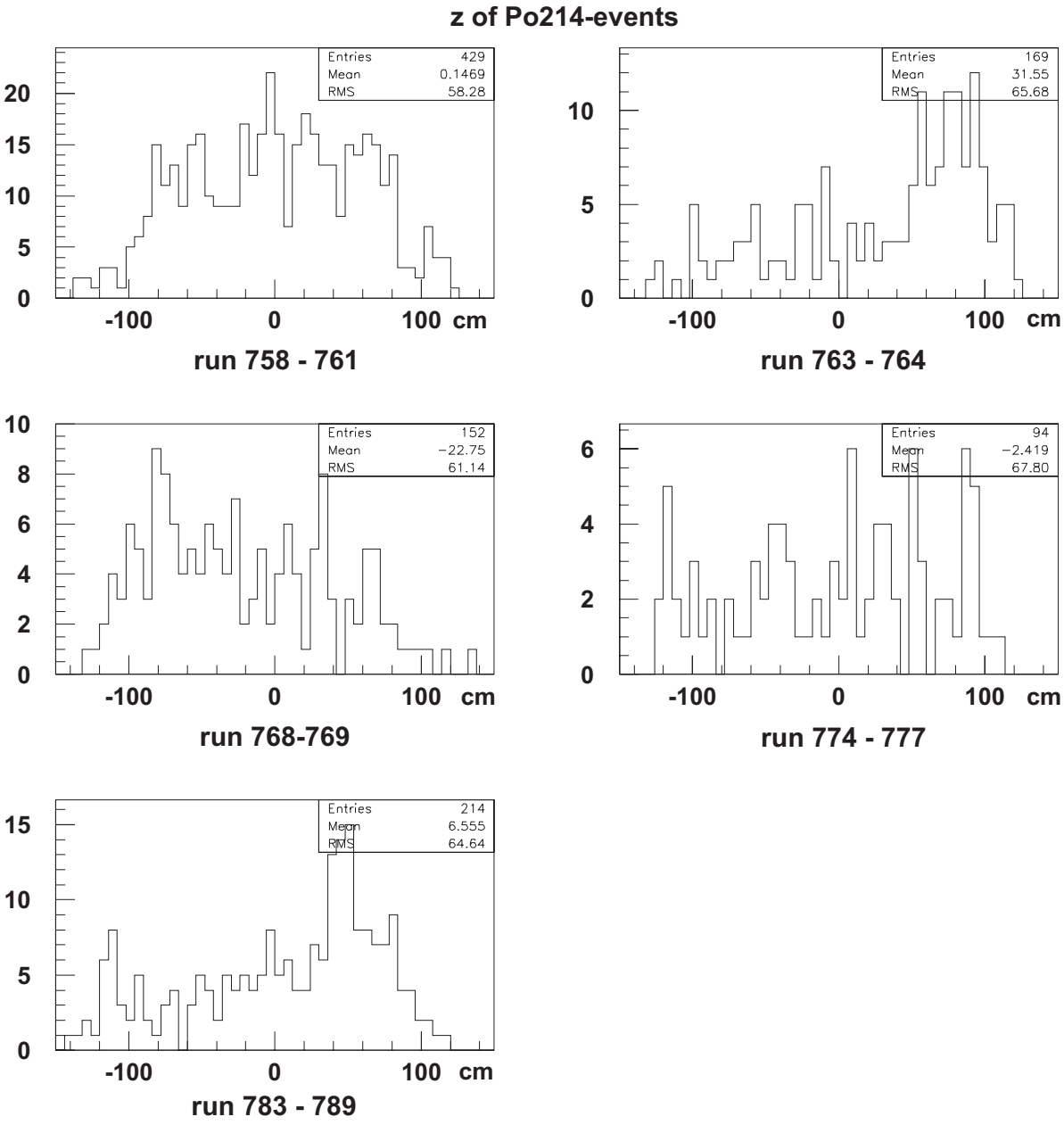

Figure 6.8: Reconstructed z of the ^{214}Po events for different periods. At the beginning, the ^{222}Rn activity is distributed homogeneously. Later some new ^{222}Rn activity is introduced from the top that slowly sinks to the bottom, while again new activity is introduced from the top.

Limit on ^{232}Th

A limit for the intrinsic ^{232}Th contamination can be derived in a similar way as for ^{238}U, as in the ^{232}Th chain there is also a delayed β-α coincidence ^{212}Bi-^{212}Po with a lifetime of 432 ns. It can be distinguished from the ^{214}Bi-^{214}Po coincidence by the higher energy of the α decay and the shorter coincidence time. The endpoint of the ^{212}Bi β decay is 2.25 MeV. The energy of the ^{212}Po α decay is 8.78 MeV, which corresponds to 1150 keV β equivalent energy (due to the quenching), yielding a pulse height of ~ 350 photoelectrons in the scintillator. This is only $2\,\sigma$ distance from the ^{214}Po peak. The background from the ^{238}U decay chain therfore has to be considered. However, due to the much longer lifetime of the ^{214}Po, the background contribution is small (see below).
The following cuts were applied to select the ^{212}Bi-^{212}Po events:

- energy of the group 1 event: more than 100 pe (efficiency 85 %);
- energy of the group 2 event: greater than 350 pe (efficiency 50 %);
- coincidence time between 50 and 3000 ns (efficiency 89 %).

Again, the two muon rejection cuts were used:

- the muon veto must not have triggered (no muonflag);
- the meantime (i.e. the average time of all hit PMTs) must be below 25 ns.

The cut on the energy of the group 2 event was chosen so high in order to minimize the contribution from ^{214}Po. The overall efficiency of the cuts for the selection of the ^{212}Bi-^{212}Po events is 38 %. Applying the same cuts to the ^{214}Bi-^{214}Po coincidence events, yields an efficiency of 0.03 %.

I analyzed the last two periods of the 4 ton runs: run 773 - 780 with a total counting period of 7.32 days, and run 783 - 789 with a total period of 6.98 days. In each period, 1 candidate event survived the cuts, corresponding to 0.137 c/d (0.143 c/d). The expected background contribution from the ^{238}U chain is about 0.01 c/d (almost 10 %).

Taking into account the 38 % efficiency of the cuts leads to a ^{212}Bi-^{212}Po decay rate of $0.086\,\mathrm{d}^{-1}\mathrm{t}^{-1}$ ($0.090\,\mathrm{d}^{-1}\mathrm{t}^{-1}$). Assuming secular equilibrium in the ^{232}Th chain, and considering the branching ratio of ^{212}Bi(β)-^{212}Po(α) of 64 %, an activity of $1\,^{212}\mathrm{Bi\,decay}/(\mathrm{day}\cdot\mathrm{ton})$ corresponds to a ^{232}Th contamination of $4.5\cdot 10^{-15}$ g/g. The ^{212}Bi-^{212}Po-rate measured in the CTF gives a ^{232}Th equivalent of

$$\begin{aligned} \mathrm{c}(^{232}\mathrm{Th}) &= (3.9 \pm 4.3)\cdot 10^{-16}\,\mathrm{g/g} \quad \text{(run 773 - 780)} \\ &= (4.0 \pm 4.4)\cdot 10^{-16}\,\mathrm{g/g} \quad \text{(run 783 - 789)} \end{aligned}$$

6.3.5 Optical Properties

Light yield

Using for the quenching factor the value measured in laboratory, the absolute energy calibration is provided by the ^{214}Po alpha peak, which corresponds to an energy of (950 ± 12) keV. This peak appears in the CTF2 at (302 ± 3) photoelectrons (see fig.
refpopeak) which leads to a light yield of

$$(318 \pm 8) \text{ photoelectrons/MeV} .$$

By fitting to the spectrum in the low energy range a ^{14}C beta spectrum folded with the detector response plus a background contribution, a light yield of

$$(311.0 \pm 0.3) \text{ photoelectrons/MeV}$$

is obtained [Res01]. Both values are in good agreement.

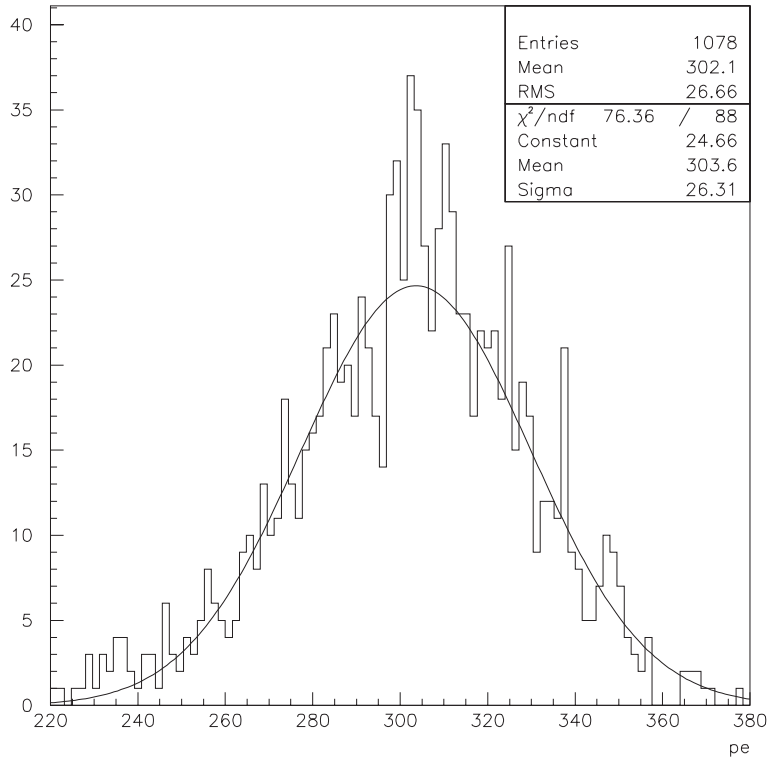

Figure 6.9: The ^{214}Po alpha peak measured in the CTF2 during the runs 758 - 785.

Energy Resolution

The energy resolution can be derived from the width of the ^{214}Po alpha peak (see fig. 6.9):

$$\frac{\Delta E}{E} = \frac{26.3}{303.6} = 8.7\,\%$$

Ideally, the relative energy resolution should be directly proportional to $1/\sqrt{n_{pe}}$, where n_{pe} is the number of photoelectrons. This leads to

$$\begin{aligned} \frac{\Delta E}{E} &= \frac{151}{\sqrt{n_{pe}}}\,\%, \\ \text{or} \quad \frac{\Delta E}{\sqrt{E}} &= 2.6\,\mathrm{keV}^{1/2}\,. \end{aligned}$$

The energy resolution can also be obtained by the fit to the ^{14}C spectrum, which gives

$$\frac{\Delta E}{\sqrt{E}} = (2.50 \pm 0.01)\,\mathrm{keV}^{1/2}\ [\text{Res01}].$$

Again, the values obtained in two different energy regions are in good agreement.

Spatial Resolution

The spatial resolution can be derived without introducing a radioactive source using the correlated decays of ^{214}Bi and ^{214}Po, which due to the short lifetime of the ^{214}Po must occur at the same place. Plotting the distance between the x-coordinates of the reconstructed positions of the ^{214}Bi and the following ^{214}Po event gives a distribution with a resolution of $\sigma_x \cdot \sqrt{2}$. This resolution is averaged over the energy range of the ^{214}Bi β events (0 - 3.2 MeV) and the ^{214}Po α events (0.7 - 1.2 MeV). The result is shown in fig. 6.10. As the ^{222}Rn is distributed homogeneously inside the scintillator, this method gives the position resolution averaged over the whole scintillator volume. The results are

$$\begin{aligned} \sigma_x &= (13.8 \pm 0.2)\,\mathrm{cm} \\ \sigma_y &= (13.6 \pm 0.2)\,\mathrm{cm} \\ \sigma_z &= (14.1 \pm 0.2)\,\mathrm{cm} \end{aligned}$$

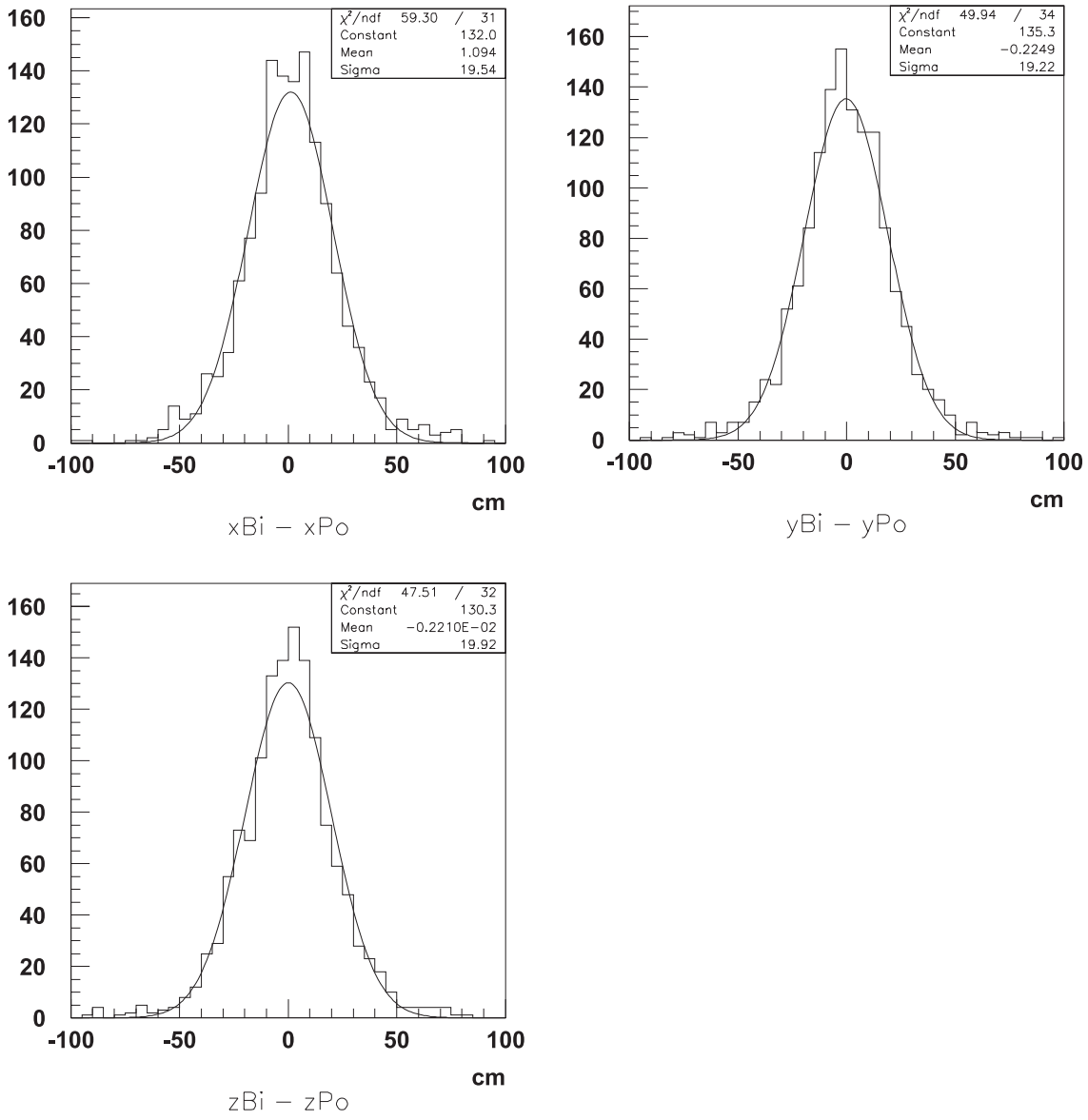

Figure 6.10: Distance between the reconstructed positions of successive ^{214}Bi and ^{214}Po events during Runs 758 - 789.

Alpha Beta Discrimination Efficiency of PXE

The pulse shape discrimination (PSD) in the CTF2 is done using the charge integration technique. The analog sum of the charge signal from all PMTs is split up into three identical signals which are fed into an integrating ADC with different time delays: from 0 - 500 ns (total), from 32 - 500 ns and from 48 - 500 ns (two different tails). The tail-to-total ratio $r_{32/tot}$ or $r_{48/tot}$ can then be used as discrimination parameter [Ran98]. In addition, a prototype of the BOREXINO

flash ADC board with the analog sum of all PMT signals was tested during some runs of the CTF2 (see chapter 5).

In order to determine the efficiency of the α/β discrimination a clean sample of α and β events in the same energy range are needed. The only events that can be unambiguously identified as α or β decays are the delayed coincidences from the ^{214}Bi(β)-^{214}Po(α) decay. I selected these events from all the 4 ton runs with the same selection criteria as for the determination of the ^{238}U contamination. Further I restricted the sample to ^{214}Bi events having energies in the same range as the ^{214}Po alpha events: 200 - 400 photoelectrons for the ^{214}Po alpha events and 100 - 500 photoelectrons for the ^{214}Bi beta events.

The efficiency of the α/β discrimination was determined by fitting a gaussian to the distribution of $r_{48/tot}$ for α and β events (see fig. 6.11). The β identification efficiency was then fixed at 98 % and the corresponding α identification efficiency was calculated to be 84.6 %. Applying a radial cut on the ^{214}Bi and ^{214}Po events of $r < 90$ cm, yields for an α identification efficiency of 92.4 %. This improvement is due to the fact, that for events in the outermost region of the Inner Vessel, where total internal reflection plays an important role, the fraction of light registered at late times, is higher than in the inner regions of the Inner Vessel.

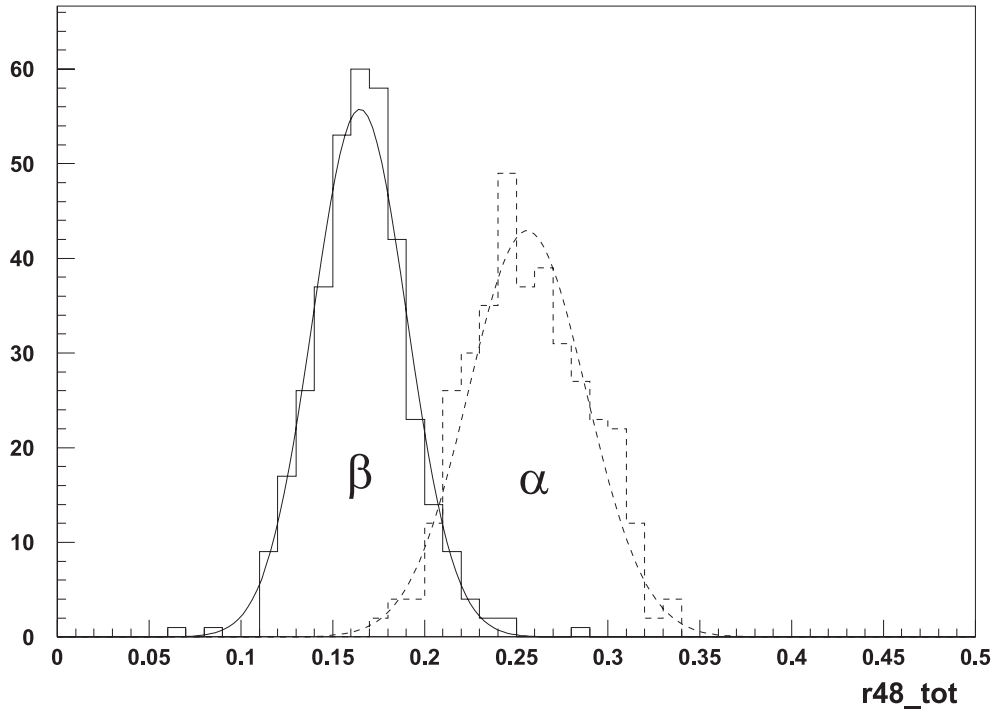

Figure 6.11: α/β discrimination capability of PXE. Plotted is the tail-to-total ratio $r_{48/tot}$ of ^{214}Bi beta events (solid line) and ^{214}Po alpha events (dashed line). For a β identification efficiency of 98.0 %, the fit yields an α identification efficiency of 84.6 %.

7 The Source Runs in CTF2

7.1 Motivation

At the end of the PXE campaign in CTF2, in September 2000, a series of calibration measurements was performed using a ^{222}Rn-source. The source consisted of a small quartz vial filled with ^{222}Rn spiked scintillator. Positioning the ^{222}Rn-source at various locations in the Inner Vessel, the homogeneity of the energy response of the detector and systematic shifts of the position reconstruction could be tested as well as the dependence of the energy and position resolution on position, energy and kind of decay.

^{222}Rn offers several advantages as a radioactive source material, including the ease with which it can be detected. The decay of the short lived ^{222}Rn-daughters ^{214}Bi (β) and ^{214}Po (α) occurs with a half life of 164 μs, so that these events can be tagged very efficiently using a cut on the energy of the ^{214}Po decay and the coincidence time. The relatively short 3.8 day half life of ^{222}Rn is also advantageous. This would allow its decay in the unfortunate case that a source contaminated the detector.

As introducing a radioactive source bears the risk of contaminating the scintillator these measurements could be done only at the end of the PXE campaign though for a better understanding of the detector performance it would be wishful for BOREXINO to do some calibration measurements with a localized source before the solar neutrino data taking starts. For the planned calibration strategy for BOREXINO see e.g. [Man00].

7.2 Production of the Sources

For the calibration measurements a few ml of liquid scintillator loaded with a ^{222}Rn-activity of 0.1 – 1 Bq are needed. A lower activity would lead to a worse signal/background ratio (background comes from ^{222}Rn homogeneously distributed in the scintillator originating from a ^{238}U/^{226}Ra-contamination of the scintillator itself or introduced with air together with the sources), whereas a higher activity would result in a high deadtime of the detector (the data acquisition of the CTF2 needs 110 ms for the read-out of one event, so that for rates higher than a few Hz there is a significant dead time) and an increase of the background by accidental coincidences. The Rn-loaded scintillator is contained in small quartz vials. Quartz is UV

transparent, so that it doesn't absorb the scintillation light, and has a refractive index similar to that of the scintillator. For the production of the sources (see fig. 7.1) a ^{222}Rn-emanating ^{226}Ra-source was used (emanation rate ~ 40 Bq). Special care was taken that the source never comes in direct contact with the scintillator to avoid a possible ^{226}Ra contamination, as this would contaminate the CTF scintillator in the case of leaking or breaking of the quartz vial. The ^{226}Ra source was placed in a small evacuated gas volume and left there for several days.

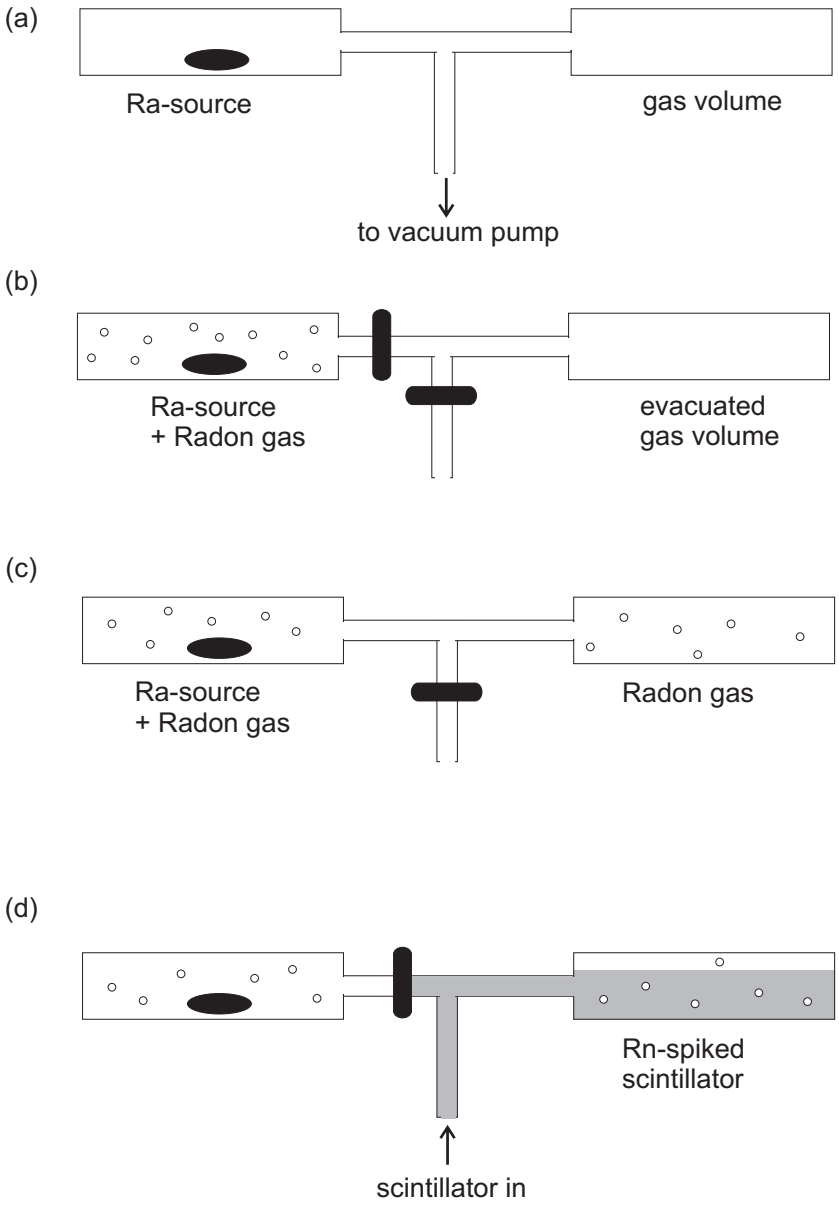

Figure 7.1: Schematic drawing of the production of the sources: (a) all volumes are evacuated; (b) the Ra-source emanates Rn-atoms into the vacuum; (c) both volumes are connected, the Rn-concentration in both volumes equilibrates; (d) the flask containing the Ra-source is isolated, scintillator is sucked into the other flask due to low pressure.

Then the gas volume was decoupled from the source and brought in contact with PXE scintillator (that had been bubbled with nitrogen first to remove dissolved oxygen). As the partition coefficient for Rn in liquid scintillator to Rn in gas is about 10:1, after a short contact time most of the Rn should have been transferred from the gas phase to the scintillator. The Rn-loaded scintillator was finally filled into a small quartz vial and closed with teflon screw caps (see fig. 7.2).

In the transfer of the radon-spiked scintillator to the source vial, it was necessary to minimize oxygen contamination, as oxygen causes quenching of the scintillation light. Hence all the work was carried out in a glove bag under nitrogen atmosphere. Anyhow, the sources showed some evidence of oxygen contamination, as the position of the ^{214}Po peak was shifted to lower energies compared to its position during the 'non-source' runs. The spiked scintillator could not be sparged for oxygen removal, as this would also remove the ^{222}Rn.

The source test in the CTF2 was done with two different Rn-sources:

- Source no. 1 consisted of a cylindrical quartz vial with a diameter of 1.7 cm, 9.5 cm length, filled with Rn-loaded scintillator and closed with teflon screw caps at both ends. This source had a rather low Rn-activity ($\sim$ 0.06 Bq). The scintillator inside the source was quenched (^{214}Po-peak at $\sim$ 200 pe).
- Source no. 2 had a diameter of 1 cm, 5.5 cm length, and only one teflon screw cap at the top. The initial Rn-activity was $\sim$ 0.3 Bq. The scintillator was highly quenched (^{214}Po-peak at $\sim$ 100 pe).

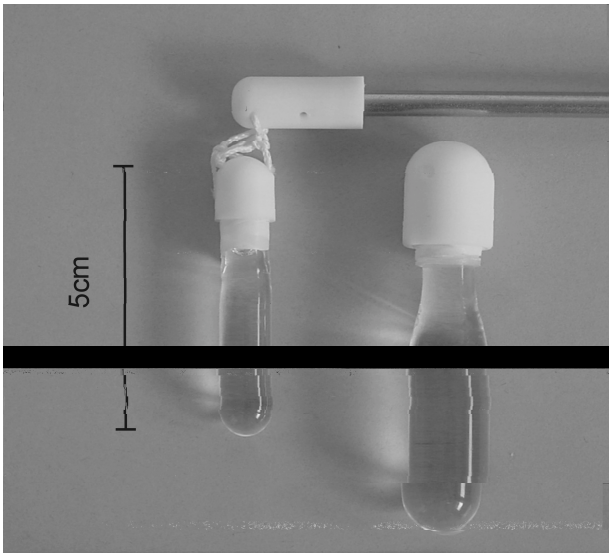

Figure 7.2: Two quartz vials filled with Rn-spiked scintillator, that were used for the calibration runs in CTF2.

7.3 The Source Runs

The sources were inserted into the Inner Vessel from the purification clean room on the top of the CTF tank. They passed through the scintillator inlet tube. Normally the vessel with its plumbing is allowed to move freely relative to the water tank. To stabilize it in a certain position it is counterbalanced by a weight connected over a rope pulley. During the source operations the plumbing-vessel assembly was held in place with clamps. The top flange (normally used as attachment point for the rope to the counterbalance weight) was removed and replaced by a flange with a short 'adapter tube' attached, that has an inner diameter only few mm wider than the diameter of the steel rod to which the source was attached. The sources were inserted through this opening. To prevent air (oxygen and ^{222}Rn) from getting in contact with the scintillator, a continuous nitrogen flow in the outward direction was maintained. The nitrogen was introduced into the plumbing at a tee below the top opening and it exited through this opening (see fig. 7.3).

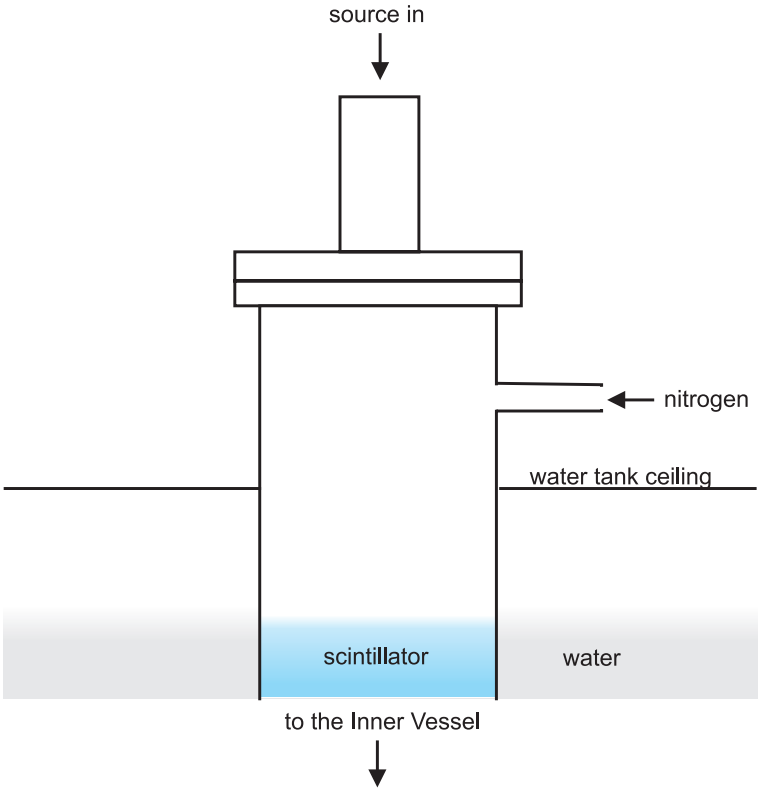

Figure 7.3: Setup for the source insertion.

For the positioning of the sources we used a stainless steel rod with a hinge so that positions on the z-axis as well as positions off-axis could be measured. The rod was divided into 8 sections, each 1 m long, that could be screwed together while lowering the source into the IV. This was necessary because of the height limitations imposed by the cleanroom ceiling.

Source no. 1 was mounted with a short nylon cord directly to the steel rod. With this source we could measure only positions on the z-axis. With source no. 2 we used a short coupling to a hinge and a 48 cm lever arm that could be lifted up to a horizontal position using a nylon pull-string (see fig. 7.4). The source was mounted with a short cord at the end of the lever arm. With this source we measured points on the z-axis as well as points with a horizontal distance of 48 cm from the z-axis.

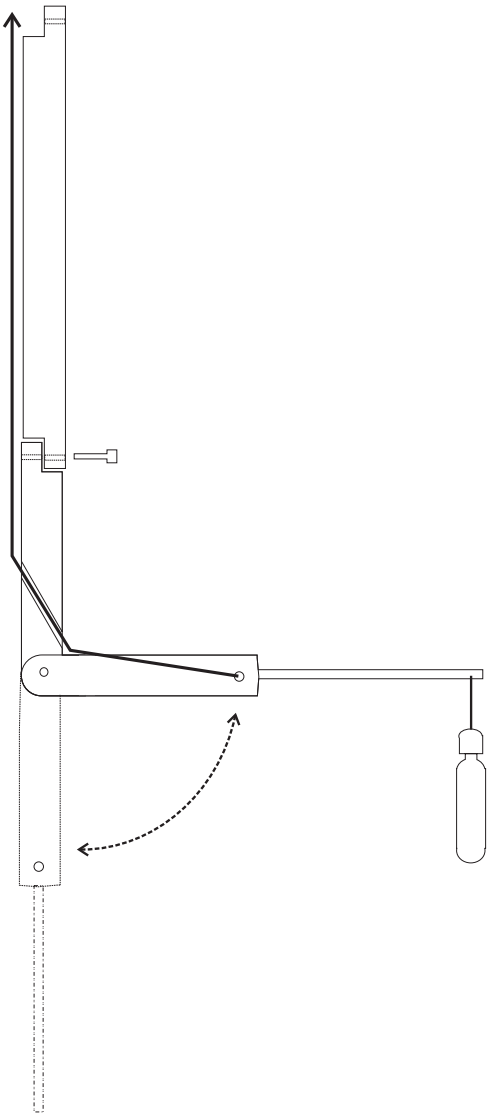

Figure 7.4: Stainless steel rod with hinge for the positioning of the sources inside the Inner Vessel. If the nylon string is loose, the lever arm hangs vertically down. If the nylon string is pulled upwards, the lever arm is brought into a horizontal position.

The nominal source positions have a rather big uncertainty:

- As the source was mounted on a steel rod in principle the position on the z-axis should be known very accurately. The measurement was always done relative to the top flange

of the tube that connects the Inner Vessel, but this tube can move relative to the CTF water tank. The Inner Vessel is counterbalanced by a weight to stabilize it in a certain position. As during the water filling of the CTF2 the counterweight wasn't changed, the tube was shifted upwards compared to the original position by about 8 cm (see fig. 7.5). The tube is connected directly to the Inner Vessel, but it is not clear whether the whole system Inner Vessel plus tubes moved upwards by ~ 8 cm, or the Inner Vessel changed its shape. This leads to a rather high uncertainty in the z-direction.

- The measurement of the angle φ (in the x,y-plane) couldn't be done very accurately. When lowering the steel rod with the hinge we marked the direction of the lever arm, but the alignment of the pieces was not always perfect. After positioning of the source, the upper end of the steel rod was fixed to the PC inlet tube and wrapped with several

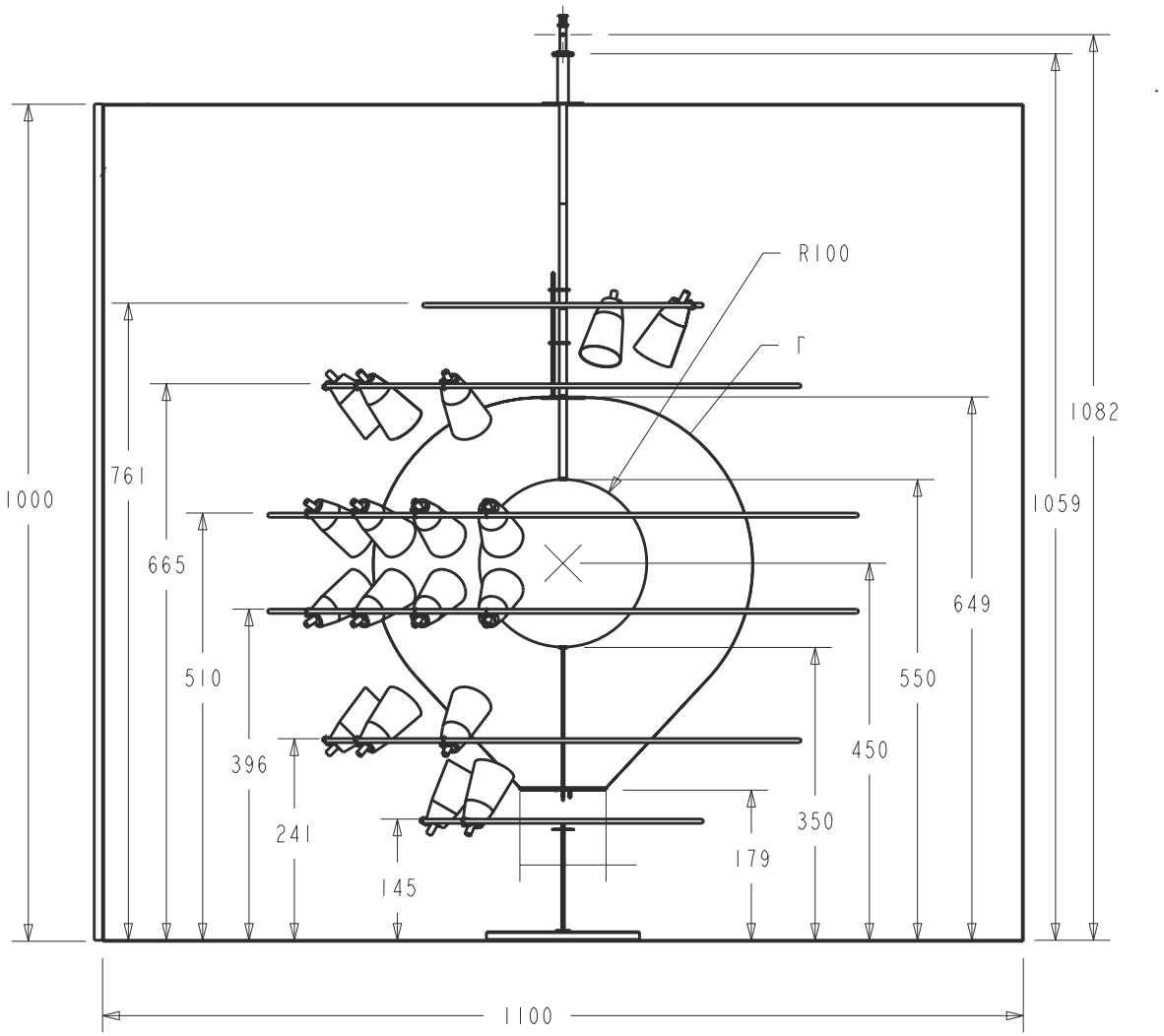

Figure 7.5: Drawing of CTF2 dimensions. The position of the PC-inlet-valve is marked to be 1082 cm above floor of the hall C. We actually measured about 1090 cm above floor. This 8 cm shift gives the main uncertainty in the z-direction.

layers of plastic bags and black felt to prevent light from entering. It cannot be excluded that the direction was turned a little bit during this procedure.

- When pulling up the lever arm to measure off-axis-points, the vertical part of the steel rod was no longer perfectly vertical, but slightly tilted. This introduces an additional uncertainty in the position.

Due to these effects, the relative error in the nominal position is estimated to be

$$\begin{aligned} \Delta x,\, \Delta y &= \pm\, 10\,\mathrm{cm} \qquad \text{for off-axis-points} \\ \Delta x,\, \Delta y &= \pm\, 5\,\mathrm{cm} \qquad \text{for points on z-axis} \\ \Delta z &= \pm\, 5\,\mathrm{cm} \end{aligned}$$

Nominal source positions

	Run	x (cm)	y (cm)	z (cm)	r_{xy} (cm)	r_{xyz} (cm)
source 1	791	0	0	+32	0	32
	793	0	0	0	0	0
	795	0	0	+100	0	100
source 2	797	0	+48	0	48	48
	798	-48	0	0	48	48
	799	+27	-40	0	48	48
	800	+40	-27	-30	48	57
	801	-40	+27	-30	48	57
	802	0	0	-78	0	78
	803	0	0	-83	0	83
	804	0	0	-75	0	75
	805	0	0	-62	0	62
	807	-40	+27	-56	48	74
	809	-40	-27	-56	48	74
	810	27	-40	+11	48	49

Table 7.1: The source positions during the different runs (the runs not mentioned here were only very short runs to verify the source position). The coordinates x, y, z are given in cm, relative to the ‘nominal center’ of the IV.

7.4 Analysis of the Source Runs

7.4.1 Event Selection

To select the ^{214}Po alpha decay events, which originated from the ^{222}Rn source, the following cuts were applied:

- they are detected by the second electronic group;
- they have a coincidence time delay of 10 μs - 1 ms;
- they have a pulse height in the range $140\,\mathrm{pe} \leq \mathrm{q} \leq 260\,\mathrm{pe}$ ($70\,\mathrm{pe} \leq \mathrm{q} \leq 140\,\mathrm{pe}$ for source no. 2);
- the preceding group 1 event (^{214}Bi) has a pulse height between 100 and 1200 pe (the lower energy threshold is set to reject accidental coincidences involving ^{14}C events);
- there is no muon flag on this event or the preceding group 1 event.

With these cuts, the ^{214}Po alphas and the preceding ^{214}Bi betas can be tagged very efficiently with negligible background. Their energy spectra are shown in fig. 7.6. Fitting an exponential to the coincidence time distribution reproduces very well the decay time of ^{214}Po,

$$\mathrm{t}_{1/2} = 164\,\mu\mathrm{s} \quad \Rightarrow \quad \lambda = \frac{\ln 2}{\mathrm{t}_{1/2}} = 4.23 \cdot 10^3\,\mathrm{s}^{-1}\,,$$

while the fit gives $\lambda = 4.26 \cdot 10^3\,\mathrm{s}^{-1}$ (see fig. 7.6, lower plot).

Background

The two sources of potential background events are ^{214}Bi-^{214}Po events in the bulk scintillator volume and accidental coincidences:

- The background due to ^{222}Rn present in the scintillator containment vessel can be estimated to be at about the same level as in the previous runs before the source insertion, $\sim$ 2 counts per hour. Due to the fact that the scintillator inside the source vial was quenched and the energy of the ^{214}Po alpha peak shifted towards lower energies, the actual background contribution is even smaller.
- The accidental background can be estimated by applying the energy cuts mentioned above for the group 1 and group 2 events, but taking a coincidence time window shifted to much greater delay times (7010 - 8000 μs). For run 797 this gives an accidental background rate of ~ 2.5 counts per hour.

Compared to the source activity of 200 - 800 counts per hour (for source 1 and 2 respectively) both background contributions are negligible.

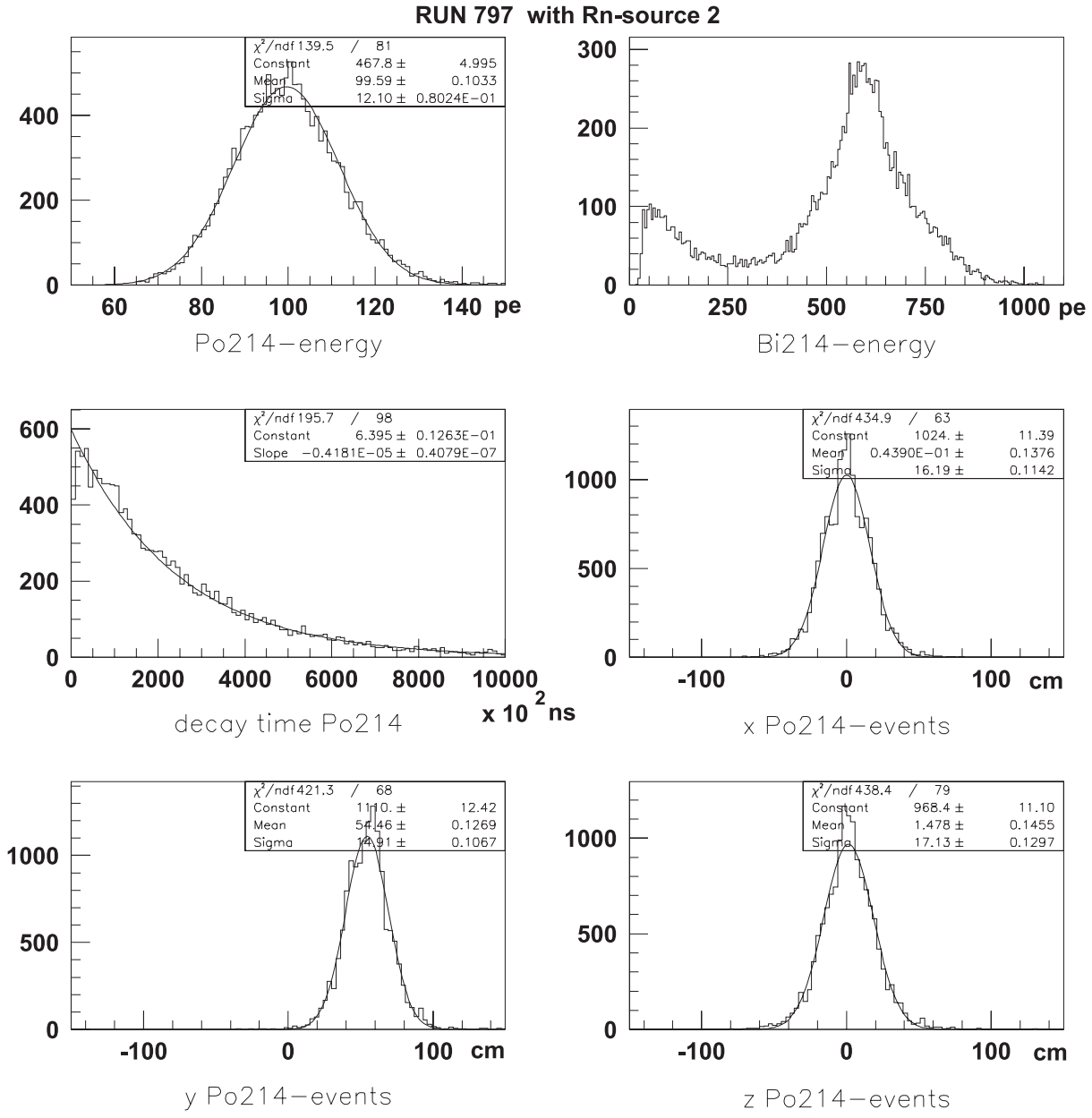

Figure 7.6: ^{214}Bi and ^{214}Po events from source run 797. The energy of the ^{214}Bi β and the ^{214}Po α events are shown, their coincidence time which corresponds to the ^{214}Po lifetime, and the reconstructed position (x,y,z) of the ^{214}Po events.

7.4.2 Reconstructed Source Positions

The reconstructed positions of the ^{214}Po alpha events are given in table 7.2. The reconstruction was done with the 'Milano' standard reconstruction code as well as with the 'Munich' code developed in this work. These two codes use different methods for the position reconstruction: the Milano code uses an analytical approach, which includes only the direct time of flight of the photons assuming an effective index of refraction throughout the whole detector (for a detailed description see [Man94]). The Munich code is based on a comparison to Monte Carlo events taking into account the effects of absorption/reemission and light scattering as well as the refraction and reflections at the border scintillator-water (see chapter 4). Both codes were not adjusted for the PXE, but use the timing behaviour of the PC scintillator.

Position of Po 214 alpha events							
		Milano Code			Munich Code		
Run	nom. position	x (cm)	y (cm)	z (cm)	x (cm)	y (cm)	z (cm)
791	0,0,32	3.4	4.4	28.4	0.0	3.8	35.7
793	0,0,0	3.7	0.3	-4.9	0.3	0.1	-1.4
797	0,48,0	4.1	52.2	-3.4	-0.1	54.0	1.9
798	-48,0,0	-47.2	4.7	0.9	-52.3	5.7	4.2
799	27,-40,0	26.7	-41.3	-2.1	22.4	-43.8	2.7
800	40,-27,-30	46.7	-25.5	-37.1	40.7	-27.9	-32.3
801	-40,27,-30	-41.6	22.8	-33.4	-47.1	23.4	-32.1
802	0,0,-78	9.0	-1.1	-87.5	0.4	-1.7	-88.2
803	0,0,-83	8.0	-1.5	-94.2	-1.0	-2.1	-95.7
804	0,0,-75	6.1	2.9	-81.9	0.0	3.0	-82.6
805	0,0,-62	6.1	-1.1	-68.4	1.4	-1.7	-69.1
807	-40,27,-56	-42.3	28.1	-63.1	-47.6	30.0	-65.1
809	-40,-27,-56	-41.5	-18.3	-62.2	-49.6	-19.3	-63.6
810	27,-40,11	31.0	-38.4	10.6	26.3	-40.7	17.4

Table 7.2: The reconstructed source position using the ^{214}Po alpha events. Shown is the mean value of a Gaussian fit to the distribution of the reconstructed events. For the position resolution see table 7.3.

The two codes do not agree perfectly, but the difference in the reconstructed positions is for most locations still within the error of the nominal position. The Milano reconstruction exhibits a systematic shift in the positive x-direction for large negative z-values (run 802 - 805). This could be a hint that in this reconstruction code the mapping between PMT position and electronic channel is done in the wrong way for some PMTs on the lower rings. The Munich code doesn't show this systematic drift.

The spatial resolution for the ^{214}Po alpha events for the two different reconstruction methods is given in table 7.3 for the individual source positions. They are also compatible.

Spatial resolution of ^{214}Po alpha events							
		Milano Code			**Munich Code**		
Run	nom. position	σ_x (cm)	σ_y (cm)	σ_z (cm)	σ_x (cm)	σ_y (cm)	σ_z (cm)
791	0, 0, 32	12.8	10.3	13.0	12.5	11.3	13.4
793	0, 0, 0	12.6	10.7	13.6	12.2	11.5	13.3
797	0,48,0	16.9	13.9	17.1	16.1	14.9	16.7
798	-48,0,0	15.3	13.4	16.3	14.9	14.5	17.5
799	27,-40,0	17.1	13.4	17.3	16.6	14.6	17.3
800	40,-27,-30	17.3	13.3	18.0	16.0	14.4	17.4
801	-40,27,-30	16.0	13.2	16.0	15.6	14.6	17.1
802	0,0,-78	18.7	14.5	17.1	17.3	16.4	18.2
803	0,0,-83	18.4	14.1	16.1	17.6	15.8	18.7
804	0,0,-75	18.4	14.7	17.0	18.0	16.7	17.8
805	0, 0,-62	16.6	14.1	16.9	15.9	15.8	17.3
807	-40,27,-56	16.5	13.9	16.3	17.0	15.9	18.8
809	-40,-27,-56	16.8	13.7	16.6	17.7	15.5	18.5
810	27,-40,11	16.8	13.5	17.4	16.3	14.9	17.2

Table 7.3: Comparison of the spatial resolution of the Milano and Munich reconstruction program for different source positions. Given is the standard deviation of a Gaussian fit to the distribution of the reconstructed events.

7.4.3 Energy Dependence of the Spatial Resolution

The approximation of the resolution of the spatial reconstruction for a point-like event is given by

$$\Delta r \sim \frac{c\,\sigma_t}{\sqrt{n_{pe}}}$$

where c is the speed of light, σ_t is the error of one time measurement and n_{pe} is the number of measurements (= number of detected photons). For beta events the Monte Carlo for CTF gives an energy dependence of the spatial resolution as:

$$\Delta x \simeq \frac{104}{\sqrt{n_{pe}}}\,\mathrm{cm}$$

For gamma events the situation is more complicated: gammas interact in the scintillator mainly due to Compton scattering. Thus they deposit energy at various points in the scintillator in a

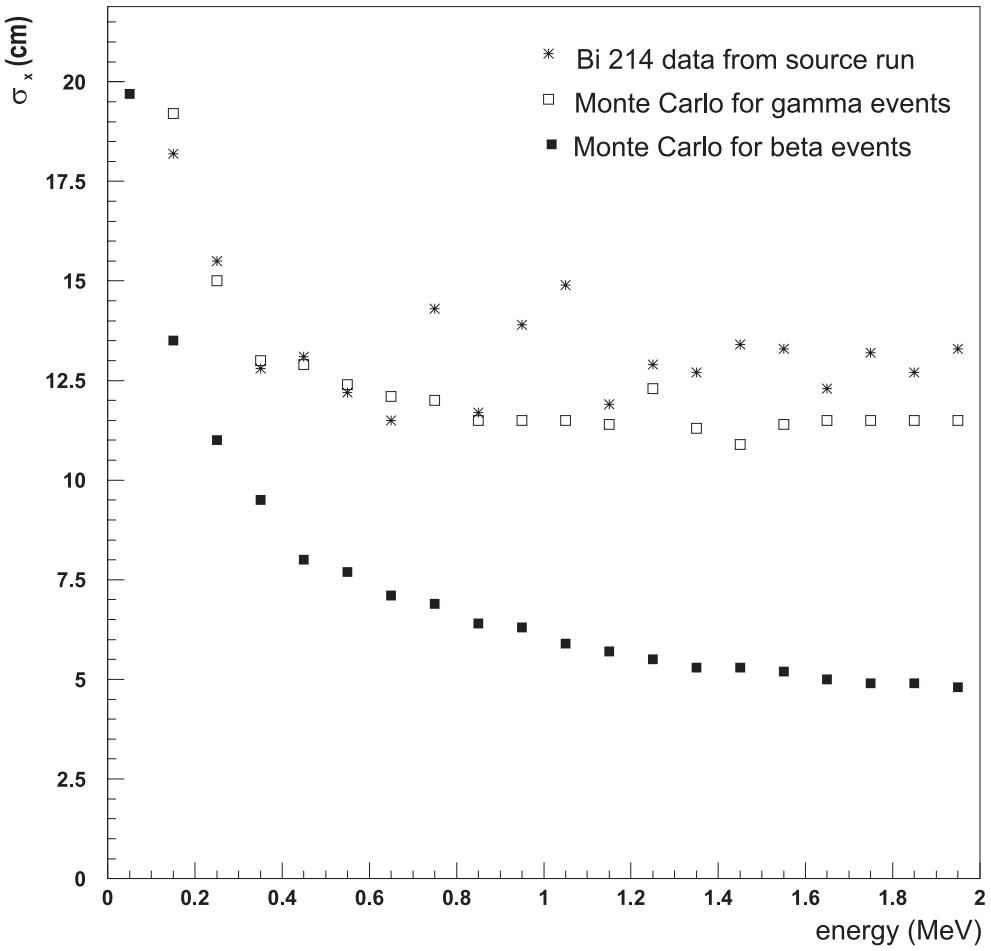

Figure 7.7: The energy dependence of the spatial resolution. Shown is a Monte Carlo simulation for beta and gamma events, and the data from ^{214}Bi events from the source run 797. The simulated resolution for beta events follows the expected dependence on $1/\sqrt{n_{pe}}$.

short period of time. The event registered by the detector consists of an overlap of these single interactions. The effective position of such an event is the 'center of light' of the various energy deposits. A gamma event is hence called an 'extended event'. The higher the energy of the gamma, the larger the extension of the event. The Monte Carlo for the CTF gives for the energy dependence of the spatial resolution a rather flat curve, after an initial decrease at low energies.

The ^{214}Bi-decay consists of a beta decay to an excited state of ^{214}Po, followed by the emission of one or more γ-rays. The energy dependence of the position resolution for these events is shown in fig. 7.7 and compared to the Monte Carlo resolutions for beta and gamma events. The resolution as measured in the CTF2 is worse than predicted by the Monte Carlo, indicating that some effects on the timing are not fully accounted for in the Monte Carlo.

7.4.4 Energy Resolution

Ideally, the relative energy resolution should be directly proportional to $1/\sqrt{n_{pe}}$, where n_{pe} is the number of photoelectrons. The ^{214}Po alpha events correspond to 950 keV beta equivalent energy, if the scintillator is not quenched. The measured pulse height during the runs 758 - 789 is (304 ± 23) photoelectrons (see fig. 7.8). This gives a relative energy resolution of

$$\frac{\Delta E}{E} = \frac{132}{\sqrt{n_{pe}}}\,\% \,.$$

For source no. 1 the measured pulse height is (201 ± 17) photoelectrons, leading to

$$\frac{\Delta E}{E} = \frac{120}{\sqrt{n_{pe}}}\,\% \,.$$

For source no. 2 the measured pulse height is (104 ± 13) photoelectrons, giving

$$\frac{\Delta E}{E} = \frac{127}{\sqrt{n_{pe}}}\,\% \,.$$

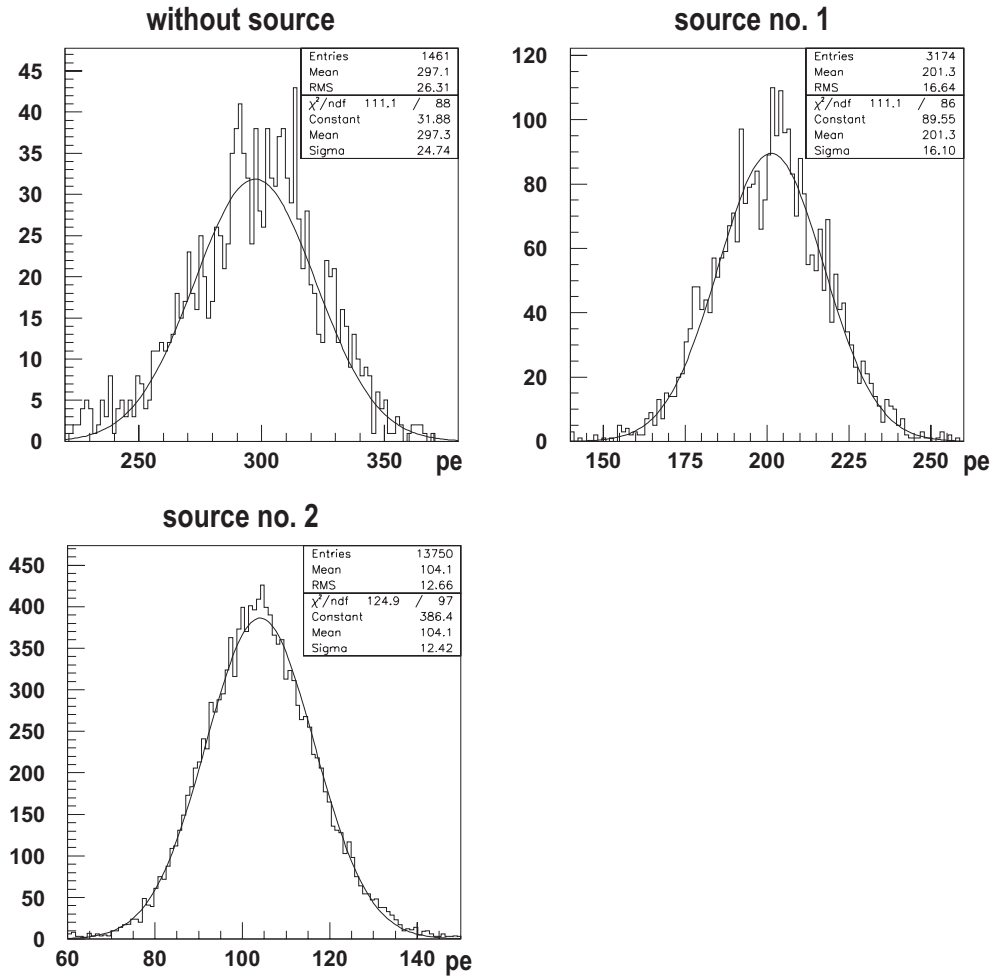

Figure 7.8: The energy of the ^{214}Po alpha peak is shown for the three cases: without source (run 758 - 789), with source no. 1 (run 793), with source no. 2 (run 797). In the first case - without source - the ^{214}Po events are distributed homogeneously in the Inner Vessel, while the source was localized in (0,0,0) for run 793, and (0,48,0) for run 797.

7.4.5 Homogeneity of the Detector Response

The pulse height of the ^{214}Po signal at various source positions is a test for the homogeneity of the detector response. The pulse height of the ^{214}Po peak varies $\pm$ 5 % within the Inner Vessel volume (see table 7.4). It was not possible to predict the detected pulse height at the individual source positions with the Monte Carlo simulation, indicating that the exact position and/or the shape of the Inner Vessel were not known precisely enough.

Run	Position (x,y,z in cm)	Radius (in cm)	^{214}Po Energy (in pe)
797	0,48,0	48	105.7 ± 12.6
798	-48,0,0	48	106.2 ± 12.3
799	27,-40,0	48	103.9 ± 12.0
800	40,-27,-30	57	104.9 ± 12.5
801	-40,27,-30	57	108.1 ± 12.5
802	0,0,-78	78	103.4 ± 12.3
803	0,0,-83	83	106.7 ± 12.5
804	0,0,-75	75	97.9 ± 12.0
805	0,0,-62	62	98.1 ± 12.0
807	-40,27,-56	74	104.8 ± 12.5
809	-40,-27,-56	74	104.6 ± 12.4
810	27,-40,11	49	103.2 ± 12.3

Table 7.4: The beta equivalent energy of the ^{214}Po peak for the individual source runs.

7.4.6 Time Response

With the source being at the detector's center, the time response of the PMTs can be tested. As the distance to all the PMTs is the same, all signals can be used, allowing a higher statistics of the collected data. The true single photoelectron probability density can not be measured in the CTF, as the mean number of photoelectrons per PMT is too high for events with an energy above the threshold. To correctly measure the single photoelectron response curve, the mean number of photoelectrons per channel shouldn't exceed 0.02, corresponding to events with a total pulse height of 2 photoelectrons. The trigger threshold in the CTF2 was about 20 photoelectrons.

From all the ^{214}Po alpha events in run 793 (source in the center) I selected the PMTs which had measured a pulse height between 0.5 and 1.5 pe, and stored the corresponding TDC values. I repeated the same procedure with Monte Carlo simulated alpha events of the same energy. The resulting time spectra are plotted in fig. 7.9.

It can be seen that the real data curve deviates from the simulated one at small and large times:

- The behaviour between 8 and 25 ns is reproduced very well by the Monte Carlo. Both curves drop with the same slope, corresponding to a decay time of 7.19 ns. This is much higher than the fast scintillation decay time (3.2 ns) measured in laboratory experiments, as in the large scintillator volume of the CTF the effects of scattering and absorption and

reemission play an important role. The fact, that both curves have the same slope, is an indication that these effects are well accounted for in the simulation.

- The experimentally derived curve has a much broader peak at small times. This peak is mainly due to the time jitter of the PMTs (+ electronics) indicating that the real time jitter is larger than the 1 ns included in the simulation.

- For $t > 25$ ns, the experimentally derived curve is not decreasing as fast as the simulated one. This may be an indication for some effects that are not included in the Monte Carlo, e.g. the relative fraction of photons emitted at large decay times could be higher in PXE than in PC (the Monte-Carlo uses the scintillation decay times for PC) or simply dark noise of the PMTs.

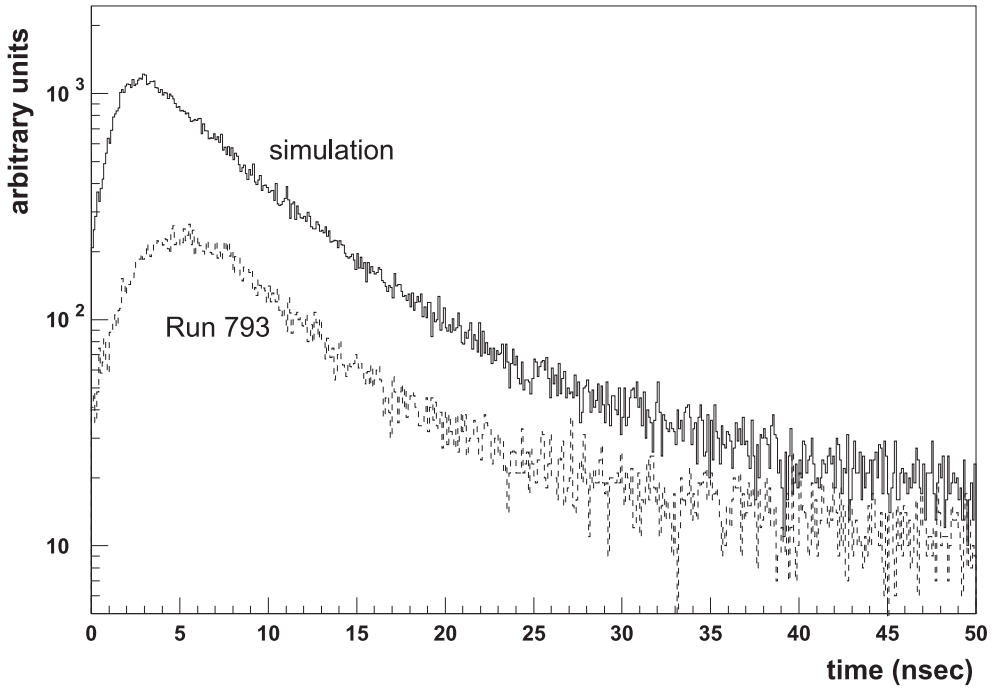

Figure 7.9: Time response curve for ^{214}Po alpha events from the source in the center of the CTF2, considering only PMTs which have recorded ~ 1 pe. The upper curve is derived from a Monte Carlo simulation, the lower curve from the data of run 793. The Monte Carlo spectrum was calculated with a better statistics.

Summary and Outlook

The solar neutrino problem, which has puzzled physicists during the past 30 years, is on the verge of being solved by the next generation of solar neutrino experiments. Taking together the results from the 6 solar neutrino experiments that have been operating to date, evidence for neutrino oscillations is provided. Astrophysical or nuclear physics solutions to the solar neutrino problem can be largely excluded nowadays.

A global analysis of the results of all solar neutrino experiments under the assumption of neutrino oscillations, yields several allowed combinations of neutrino mass and mixing parameters, including vacuum oscillations (VAC) and matter enhanced oscillations (SMA, LMA, LOW). By measuring the energy dependent suppression of the solar electron neutrino flux over the whole energy range, an accurate determination of these parameters should become possible. Therefore the goal of the second generation solar neutrino experiments must be to perform a full spectroscopy of solar neutrinos in both charged and neutral current.

In the high energy range (above 8 MeV) this is already being realized by the SNO and Super-Kamiokande experiment: Super-Kamiokande measures the total flux of the solar ^{8}B neutrinos via ν-e^- scattering (CC + NC), while SNO measures the electron neutrinos (CC) separately. Both experiments detect the neutrinos in real-time and energy resolved. Comparing the results of the two experiments revealed that about 2/3 of the ^{8}B neutrinos oscillate to another flavour before reaching the earth.

However, the currently allowed solutions show only a modest energy dependence of the survival probability in the high energy range (above 5 MeV), while in the low energy range (< 1 MeV) they have a strong energy dependence and characteristic time variability. Besides, more than 98 % of the solar neutrino flux (SSM) lies below 1 MeV, while the high energetic ^{8}B neutrinos constitute less than 10^{-4}. It is therefore crucial to measure directly the low energetic pp and ^{7}Be neutrinos.

The gallium experiments are still the only experiments that are sensitive to pp neutrinos, which constitute the vast majority of the solar neutrino flux, and their continuation is therefore very important to uncover an eventual time variability of the solar neutrino flux. However as radiochemical experiments they can measure only the integrated electron neutrino flux above the energy threshold of 233 keV.

BOREXINO, which will start data taking within one year from now, will measure for the first time directly and in real-time the flux of the monoenergetic solar ^{7}Be neutrinos (862 keV). With the measurement of the total rate and the time variability of the ^{7}Be neutrinos, it will be

possible to distinguish clearly between the different currently allowed oscillation scenarios.

The LENS experiment aims at a real-time charged current detection of the ^{7}Be and, eventually the pp neutrinos. By measuring the CC and the neutrino-electron scattering (CC + NC) rate of the ^{7}Be neutrinos, their total flux can be determined and compared with solar model predictions. The comparison of the results from BOREXINO and LENS can then give an unambiguous proof for oscillations of the ^{7}Be neutrinos.

The identification of the neutrino signal in BOREXINO relies on the distinction of a Compton-like edge in the electron energy spectrum, due to the monoenergetic (862 keV) ^{7}Be neutrinos scattered off electrons. Since the neutrino signal does not have any event-by-event signature, reduction and rejection of the background signals from radioactive decays are essential. As the expected signal rate in BOREXINO is less than $0.5\,\mathrm{counts}/(\mathrm{ton}\cdot\mathrm{day})$ in the energy range from 0.25 - 0.8 MeV, the requirements on the radiopurity of the detector components are extremely challenging: for the liquid scintillator, a maximum concentration of ^{238}U and ^{232}Th of 10^{-16} g/g and of ^{40}K of 10^{-14} g/g is allowed in order to achieve a signal/background ratio ≥ 1 even in the case of total conversion of ν_e into $\nu_{\mu,\tau}$. The necessary background suppression can be achieved only if a large fraction of the background events can be rejected by their pulse shape characteristics (alpha decays) and by spatial cuts (discrimination of external background by fiducial volume cut). It is therefore crucial to provide several independent analysis methods which can be used for cross checks of the efficiency and systematic uncertainty of the applied cuts.

In this work, a new method for the spatial reconstruction of scintillation events for BOREXINO and the CTF was developed and successfully tested with Monte Carlo simulations and CTF2 data. From laboratory measurements and source tests in the CTF1, the parameters for an optical model of the light propagation in the liquid scintillator have been evaluated and applied in a tracking program developed for BOREXINO and the CTF. The reconstruction compares the ADC and TDC data from a real event with values from simulations on a spatial grid. The resolution of this reconstruction method therefore depends strongly on the understanding of the light propagation mechanisms. Calibration measurements with localized sources in the CTF2 were performed in order to study the systematic behaviour of the reconstruction code.

A new liquid scintillator based on phenyl-o-xylylethane (PXE) was tested as an alternative choice for BOREXINO. Its physical and chemical properties make it superior to pseudocumene (PC) in some respects, e.g. the higher density (target mass) and the higher flash point (safety), but there are also some limitations which need further investigation. In particular, the ^{14}C concentration was about 6 times higher than in the PC measured in the CTF1 ($^{14}\mathrm{C}/^{12}\mathrm{C} \approx 2 \cdot 10^{-18}$). The ^{14}C level may vary, though, depending on the petroleum source, and also for the PC a new batch of scintillator from another source could have a higher $^{14}\mathrm{C}/^{12}\mathrm{C}$ ratio. The very low ^{238}U concentration that was measured in PXE by NAA ($< 1 \cdot 10^{-17}$ g/g) could not be confirmed by CTF measurements, as in the CTF1 the sensitivity of the detector was substantially reduced due to the failure of a large fraction of the PMTs, and in the CTF2 a ^{222}Rn background of the order of several 10^{-15} g/g from an unidentified source was present. The ^{232}Th concentration measured in the CTF2 ($4.0 \pm 4.4 \cdot 10^{-16}$ g/g) is compatible with the limit of $< 2 \cdot 10^{-16}$ g/g that was measured with NAA, confirming the high intrinsic radiopurity

of this scintillator. The α/β discrimination efficiency in PXE was found to be within the requirements for BOREXINO. The calibration measurements performed in the CTF2 showed that the optical properties of the PXE are generally comparable to those of PC, but more detailed studies of the exact timing behaviour and absorption/reemission probabilities of PXE would be needed.

The development of large volume low background scintillation detectors, that was successfully demonstrated with the CTF, opens new perspectives for low energy neutrino detection: with future solar neutrino experiments using the liquid scintillation technique (BOREXINO, LENS ...) it will be possible to determine the flux of the solar ^{7}Be neutrinos in both charged and neutral current, which is needed in order to settle the neutrino mass and mixing parameters. If a liquid scintillator with an extremely low ^{14}C content could be found, even the ultimate challenge of a real-time detection of the low energetic pp neutrinos could be met by BOREXINO.

Bibliography

[Ade98] E. G. Adelberger et al., *Solar fusion cross sections,* Rev. Mod. Phys. **70** (1998), 1265–1292.

[Ahm01] Q. Ahmad et al., *Measurement of charged current interactions produced by ^8B solar neutrinos at the Sudbury Neutrino Observatory*, Phys. Rev. Lett. **87** (2001), no. 071301, 1–6.

[Ali98a] G. Alimonti et al., *A large-scale low-background liquid scintillation detector: The Counting Test Facility at Gran Sasso,* Nucl. Instrum. Meth. **A 406** (1998), 411–426.

[Ali98b] G. Alimonti et al., *Measurement of the C-14 abundance in a low-background liquid scintillator*, Phys. Lett. **B 422** (1998), 349–358.

[Ali98c] G. Alimonti et al., *Ultra-low background measurements in a large volume underground detector*, Astroparticle Physics **8** (1998), 141–157.

[Ali99] G. Alimonti et al., *Physics beyond solar neutrinos,* Addendum to the Borexino Proposal (1999).

[Ali00] G. Alimonti et al., *Light propagation in a large volume liquid scintillator*, Nucl. Instrum. Meth. **A 440** (2000), 360–371.

[Ali01] G. Alimonti et al., *Science and technology of borexino: A real time detector for low energy solar neutrinos*, accepted for publication in Astroparticle Physics (2001).

[Alt00] M. Altmann et al., *GNO solar neutrino observations: Results for GNO I*, Phys. Lett. **B 490** (2000), 16–26.

[Alt01] M. Altmann, R. Mößbauer, and L. Oberauer, *Solar Neutrinos*, Reports on progress in physics **64** (2001), 97–146.

[Ang97] G. Angloher, *Untersuchungen zur Reinheit von Komponenten des Borexino-Detektors (in German)*, Diploma thesis, Technische Universität München, 1997.

[Arp01] C. Arpesella et al., *Measurements of extremely low radioactivity levels in BOREXINO*, to be published (2001).

[Bah64] J. N. Bahcall, *Solar neutrinos. I. Theoretical*, Phys. Rev. Letters **12** (1964), 300–302.

[Bah89] J. N. Bahcall, *Neutrino Astrophysics*, Cambridge University Press, 1989.

[Bah96] J. N. Bahcall and A. Ulmer, *The temperature dependence of solar neutrino fluxes*, Phys. Rev. **D 53** (1996), 4202–4225.

[Bah98] J. N. Bahcall, S. Basu, and M. H. Pinsonneault, *How uncertain are solar neutrino predictions?*, Phys. Lett. **B 433** (1998), 1–8.

[Bah00] J.N. Bahcall, P.I. Krastev, and A. Yu.Smirnov, *What will the first year of SNO show?*, Phys.Lett. **B 477** (2000), 401–409.

[Bah01a] J. N. Bahcall, S. Basu, and M. H. Pinsonneault, *Solar Models: current epoch and time dependences, neutrinos, and helioseismological properties*, Astrophysical Journal **555** (2001), 990–1012.

[Bah01b] J. N. Bahcall, M. C. Gonzalez-Garcia, and C. Pena-Garay, *Global analysis of solar neutrino oscillations including SNO CC measurement*, hep-ph/0106258 (2001).

[Bal96] M. Balata et al., *The water purification system for the low background counting test facility of the Borexino experiment at Gran Sasso*, Nucl. Instrum. Meth. **A 370** (1996), 605–608.

[Bel91] G. Bellini, M. Campanella, D. Giugni, and R. Raghavan (eds.), *Borexino at Gran Sasso, proposal for a real time detector for low energy solar neutrinos*, Milano, August 1991.

[Bel00] G. Bellini et al., *High sensitivity quest for Majorana neutrino mass with the BOREXINO counting test facility*, Phys. Lett. **B 493** (2000), 216 – 228.

[Bel01] G. Bellini et al., *High sensitivity 2beta decay study of Cd-116 and Mo-100 with the BOREXINO counting test facility (CAMEO project)*, Eur. Phys. J. **C 19** (2001), 43–55.

[Ben98] J. Benziger et al., *A scintillator purification system for a large scale neutrino experiment*, Nucl. Instr. Methods **A 417** (1998), 278–296.

[Bet39] H. A. Bethe, *Energy production in stars*, Phys. Rev. **55** (1939), 434–456.

[Bil99] S. M. Bilenky, C. Giunti, and W. Grimus, *Phenomenology of Neutrino Oscillations*, Prog. Part. Nucl. Phys. **43** (1999), 1–86.

[Bir64] J. Birks, *The theory and practice of scintillation counting*, Pergamon Press, 1964.

[Bon99] R. Bonetti et al., *First measurement of the He3+He3→He4+2p cross section down to the lower edge of the solar Gamow peak*, Phys. Rev. Lett. **82** (1999), 5205–5208.

[Bra00] L. De Braeckeleer, *Neutrino physics with the KamLAND detector*, Nucl. Phys. Proc. Suppl. **87** (2000), 312–314.

[Bro79] F. D. Brooks, *Development of organic scintillators*, Nucl. Instr. Meth. **162** (1979), 477–505.

[Cac00] B. Caccianiga and M. Giammarchi, *Neutrinoless double beta decay with Xe-136 in BOREXINO and the BOREXINO Counting Test Facility (CTF)*, Astroparticle Physics **14** (2000), 15–31.

[Cad00] L. Cadonati, F. Calaprice, and M. Chen, *Supernova neutrino detection in Borexino*, hep-ph0012082 (2000).

[Che99] M. Chen et al., *Quenching of undesired fluorescence in a liquid scintillator particle detector*, Nucl. Instrum. Meth. **A 420** (1999), 189–201.

[Cri00] M. Cribier, *The LENS experiment*, Nucl. Phys. Proc. Suppl. **87** (2000), 195–197.

[Dav68] R. Davis et al., *Search for neutrinos from the Sun*, Phys. Rev. Lett. **20** (1968), 1205–1209.

[Dav98] R. Davis et al., *Measurement of the solar electron neutrino flux with the Homestake chlorine detector*, Astrophys. J. **496** (1998), 505 – 526.

[Eli96] F. Elisei, F. Masetti, and U. Mazzucato, Borexino Internal Report Nr. 10, 1996.

[Fog01] G. L. Fogli, E. Lisi, D. Montanino, and A. Palazzo, *Model-dependent and independent implications of the first Sudbury Neutrino Observatory results*, hep-ph/0106247 (2001).

[Fuk98] Y. Fukuda et al., *Evidence for oscillation of atmospheric neutrinos*, Phys. Rev. Lett. **81** (1998), 1562–1567.

[Fuk01] S. Fukuda et al., *Constraints on neutrino oscillations using 1258 days of Super-Kamiokande solar neutrino data*, hep-ex/0103033 (2001).

[Gat99] F. Gatti et al., *DAQ electronics for the Borexino experiment*, Nucl. Phys. Proc. Suppl. **78** (1999), 111–114.

[Gat01] F. Gatti et al., *The Borexino read out electronics and trigger system*, submitted to Nucl. Instr. Meth. A (2001).

[Gav01] V. N. Gavrin, *Solar neutrino results from SAGE*, Nucl. Phys. B (Proc. Suppl.) **91** (2001), 36–43.

[Gol97] T. Goldbrunner, *Messung niedrigster Aktivitäten für das solare Neutrinoexperiment Borexino (in German)*, Ph.D. thesis, Technische Universität München, 1997.

[Gol98] T. Goldbrunner et al., *New records on low activity measurements with neutron activation analysis*, Nucl. Phys. (Proc. Suppl.) **B 61** (1998), 176–179.

[Gri00] C. Grieb, *Untersuchungen zur Szintillatorreinigung mit Kieselgel, Studien zum Untergrund und Vakuum-Neutrinooszillationen in Borexino (in German)*, Diploma thesis, Technische Universität München, 2000.

[Gri01] C. Grieb, private communication, 2001.

[Hag00a] T. Hagner, *Kosmogener Untergrund für das solare Neutrinoexperiment Borexino (in German)*, Ph.D. thesis, Technische Universität München, 2000.

[Hag00b] T. Hagner et al., *Muon-induced production of radioactive isotopes in scintillation detectors*, Astropart. Phys. **14** (2000), 33–47.

[Ham99] W. Hampel et al., *GALLEX solar neutrino observations: Results for GALLEX IV*, Phys. Lett. **B 447** (1999), 127–133.

[Har97] F. Hartmann, *Results for preparations of the low-level scintillator in BOREXINO*, Proceedings of the fourth internatonal Solar Neutrino Conference, Max-Planck-Institut für Kernphysik Heidelberg (1997).

[Hat97] N. Hata and P. Langacker, *Solutions to the solar neutrino anomaly*, Phys. Rev. **D 56** (1997), 6107–6116.

[Heu00] G. Heusser et al., *^{222}Rn-detection at the μBq/m^3 range in nitrogen gas and a new Rn purification technique for liquid nitrogen*, Appl. Rad. Isot. **52** (2000), 691–695.

[Hor74] Donald L. Horrocks, *Applications of liquid scintillation counting*, Academic Press, 1974.

[Ian98] A. Ianni, *Studio di proprieta non convenzionali per il neutrino mediante sorgenti artificiali di alta intensita in BOREXINO (in Italian)*, Ph.D. thesis, Universita di L'Aquila, 1998.

[Ian99a] A. Ianni and D. Montanino, *The Cr-51 and Sr-90 sources in BOREXINO as tools for neutrino magnetic moment searches*, Astroparticle Physics **10** (1999), 331–338.

[Ian99b] A. Ianni, D. Montanino, and G. Scioscia, *Test of non-standard neutrino properties with the BOREXINO source experiments*, Eur. Phys. J. **C8** (1999), 609–617.

[Kno79] G. Knoll, *Radiation detection and measurement*, J. Wiley and sons, 1979.

[Kuz66] V. A. Kuzmin, *Detection of solar neutrinos by means of the $^{71}Ga(\nu, e^-)^{71}Ge$ reaction*, Soviet Physics JETP **22** (1966), 1051–1052.

[Len01] C. Lendvai, *Photomultiplier-Einkapselung für das Myon-Veto des Borexino-Experiments und Messung myoninduzierter Neutronen in der CTFII (in German)*, Diploma thesis, Technische Universität München, 2001.

[Lom97] P. Lombardi, Diploma thesis, Politecnico di Milano, 1997.

[Man94] I. Manno, *Reconstruction of scintillation events*, Borexino Internal Report, 1994.

[Man00] J. Maneira, *The calibration and monitoring systems for Borexino*, III International Meeting on New Worlds in Astroparticle Physics, University of the Algarve, Faro (Portugal) (2000).

[McD01] A. McDonald, *First neutrino observations from the Sudbury Neutrino Observatory*, Nucl. Phys. B (Proc. Suppl.) **91** (2001), 21–28.

[Mik85] S. P. Mikheev and A. Yu. Smirnov, *Resonance enhancement of oscillations in matter and solar neutrino spectroscopy*, Sov. J. Nucl. Physics **42** (1985), 913 – 917.

[Nef96] M. Neff, *Untersuchungen zum Untergrund durch Radioaktivität und kosmische Strahlung für das solare Neutrinoexperiment Borexino (in German)*, Diploma thesis, Technische Universität München, 1996.

[Nie00] L. Niedermeier, *Untersuchungen zur Reinheit von Szintillatorkomponenten im Rahmen des solaren Neutrinoexperiments BOREXINO (in German)*, Diploma thesis, Technische Universität München, 2000.

[Obe98] L. Oberauer and S. Schönert, *Status report of the Borexino muon identification system*, Borexino Internal Report, 1998.

[Obe01] L. Oberauer, private communication, 2001.

[Pal00] M. Pallavicini, *Handbook for Borexino electronics*, Borexino Internal Report, Nov. 2000.

[PC999] *Handbuch der gefährlichen Güter: 1,2,4-Trimethylbenzol*, Springer Verlag Berlin Heidelberg, 1999.

[Pet93] C. Peterson, T. Rögnvaldsson, and L. Lönnblad, *JetNet - a versatile artificial neural network package*, CERN-TH 7135/94 (1993).

[Pie01] A. Piepke, *KamLAND, a reactor neutrino experiment testing the solar neutrino anomaly*, Nucl. Phys. B (Proc. Suppl.) **91** (2001), 99–104.

[Pon58a] B. Pontecorvo, *Inverse beta processes and nonconservation of lepton charge*, Sov. Phys. JETP **7** (1958), 172–173.

[Pon58b] B. Pontecorvo, *Mesonium and antimesonium*, Sov. Phys. JETP **6** (1958), 429–431.

[Pon68] B. Pontecorvo, *Neutrino experiments and the problem of conservation of leptonic charge*, Sov. Phys. JETP **26** (1968), 984–988.

[PXE94] *Material safety data sheet: PXE*, Koch Chemical Company, 1994.

[Rag95] R. Raghavan, *A new liquid scintillator for massive neutrino detectors*, Borexino internal report, March 1995.

[Rag97] R. Raghavan, *New prospects for real-time spectroscopy of low energy electron neutrinos from the sun*, Phys. Rev. Lett. **78** (1997), 3618–3621.

[Rag98] R. Raghavan et al., *Measuring the global radioactivity in the earth by multidetector anti-neutrino spectroscopy*, Phys. Rev. Lett. **80** (1998), 635–638.

[Ran98] G. Ranucci et al., *Pulse-shape discrimination of liquid scintillators*, Nuclear Instruments and Methods **A 412** (1998), 374–386.

[Rau99] W. Rau, *Low-Level-Radonmessungen für das Sonnenneutrinoexperiment Borexino (in German)*, Ph.D. thesis, Universität Heidelberg und Max-Planck-Institut für Kernphysik Heidelberg, 1999.

[Rau00] W. Rau and G. Heusser, *^{222}Rn-emanation measurements at extremely low activities*, Appl. Rad. Isot. **53** (2000), 371–375.

[Res01] E. Resconi, *Measurements with the upgraded Counting Test Facility of the solar neutrino experiment Borexino*, Ph.D. thesis, Universita di Genova, 2001.

[Rie99] T. Riedel, *Spektroskopische Untersuchungen der Reinheit verwendeter Materialien im Sonnenneutrinoexperiment BOREXINO*, Diploma thesis, Technische Universität München, 1999.

[Sch99a] H. Schlattl, *The Sun, a Laboratory for Neutrino- and Astrophysics*, Ph.D. thesis, Max-Planck-Institut für Astrophysik, 1999.

[Sch99b] S. Schönert, *Probing the solar MSW large mixing angle solution with terrestrial $\bar{\nu}_e$ from European nuclear reactors with BOREXINO*, Nucl. Phys. Proc. Suppl. **70** (1999), 195–198.

[Sch99c] S. Schönert and K. Schuhbeck, *Module-0*, Borexino Internal Report, 1999.

[Sei00] H. Seidl, *Developments for the muon vetoes for Borexino and the CTF*, Diploma thesis, Technische Universität München, 2000.

[Sim00] H. Simgen, personal communication, 2000.

[Suz01] Y. Suzuki, *Solar neutrino results from Super-Kamiokande*, Nucl. Phys. B (Proc. Suppl.) **91** (2001), 29–35.

[t'H71] G. t'Hooft, *Prediction for neutrino-electron cross sections in Weinberg's model of weak interaction*, Phys. Lett. **B 37** (1971), 195.

[vH99] R. von Hentig, *Spurenanalyse primordialer Radionuklide für das solare Neutrinoexperiment Borexino (in German)*, Ph.D. thesis, Technische Universität München, 1999.

[Vog96] R. B. Vogelaar et al., *Removal of cosmogenic ^{7}Be from scintillators*, Nucl. Instr. Meth. **A 372** (1996), 59–62.

[Woj00] M. Wojcik et al., *Radon diffusion through polymer membranes used in the solar neutrino experiment Borexino*, Nucl. Instrum. Meth. **A 449** (2000), 158–171.

[Wol78] L. Wolfenstein, *Neutrino Oscillations in Matter*, Phys. Rev. D **17** (1978), 2369–2374.

Abbreviations

ADC	Analog to Digital Converter
AU	Astronomical Unit = 149 600 000 km
bis-MSB	p-bis(o-methylstyryl)benzene ($C_{24}H_{22}$)
CC	charged current ($W^{\pm}$- exchange)
CTF	Counting Test Facility
DMP	dimethylphthalate ($C_{10}H_{10}O_4$)
DSP	Digital Signal Processor
FIFO	First In First Out
FWHM	Full Width Half Maximum
INFN	Istituto Nazionale di Fisica Nucleare
LED	Light Emitting Diode
LHS	Liquid Handling System
LMA	Large Mixing Angle
LNGS	Laboratori Nazionali del Gran Sasso
mwe	meter water equivalent (1 mwe = 100 g/cm^2)
NAA	neutron activation analysis
NC	neutral current (Z^0-exchange)
PC	pseudocumene (1,2,4 trimethylbenzene, C_9H_{12})
PMT	photo multiplier tube
PPO	2,5-diphenyl-oxazole ($C_{15}H_{11}NO$)
PXE	phenyl-o-xylylethane ($C_{16}H_{18}$)
SMA	Small Mixing Angle
SNU	Solar Neutrino Unit
SSM	Standard Solar Model
TDC	Time to Digital Converter
TP	p-terphenyl (p-diphenylbenzene, $C_{18}H_{14}$)
WFD	Wave Form Digitizer

Danksagung

An dieser Stelle möchte ich all denen ganz herzlich danken, die mich während der letzten Jahre begleitet und unterstützt haben:

Zuallererst möchte ich Herrn Prof. von Feilitzsch dafür danken, dass er mir die Möglichkeit gegeben hat, an seinem Lehrstuhl im Rahmen des BOREXINO-Experiments zu promovieren und dabei interessante Erfahrungen auch außerhalb der Physik zu sammeln. Bei der Gestaltung meiner Arbeit ließ er mir große Freiheit, ich konnte aber immer auf seine Unterstützung zählen.

Herzlichen Dank an Lothar Oberauer dafür, dass er mich als Werkstudentin für BOREXINO begeistert hat. Von seinem physikalischen Verständnis und seinen Programmierkünsten habe ich in den letzten Jahren sehr viel profitiert. Nur beim Schafkopfen musste ich dafür Lehrgeld an ihn bezahlen…

Thomas Goldbrunner möchte ich dafür danken, dass er mich nach der Diplomarbeit zum Weitermachen motiviert hat. Leider hat er selbst der Physik inzwischen den Rücken gekehrt und sich ganz aufs Managen verlegt. Dabei wäre die chaotische BOREXINO-Kollaboration doch das ideale Betätigungsfeld für einen Unternehmensberater!

Prof. G. Bellini möchte ich dafür danken, dass er mir über ein INFN-Stipendium einen zweijährigen Aufenthalt an den Laboratori Nazionali del Gran Sasso, am “Puls des Experiments”, ermöglicht hat, bei dem ich nicht nur auf physikalischem Gebiet einiges dazulernen konnte.

Ein Dankeschön an Stefan Schönert dafür, dass er am Gran Sasso sein Büro mit mir geteilt hat, und mir bei so manchem Problem mit seinen Italienischkenntnissen und besten Kontakten in L’Aquilaner Amtsstuben weitergeholfen hat.

Matthias Junker, Michael Kachelrieß und George Korga danke ich für die bestens funktionierende “Nachbarschaftshilfe Assergi”, wertvolle Tipps für das Überleben mit Holzofen im Winter, und für etliche Ausflüge auf die andere Seite des Tunnels, ans Meer.

Vielen Dank auch an Mr. F. X. Hartmann für die Einführung in die Chemie der Säulenreinigung, die Beratung beim Kauf einer Espressomaschine, und das unermüdliche Sammeln von Tannenzapfen zum Anheizen.

Caren Hagner und Karl-Heinz Schuhbeck danke ich für ihre Freundschaft während der gemeinsam verbrachten Zeit am Gran Sasso zum Wiederaufbau der CTF2 und des Module-0. Mit Euch zusammen hat die Arbeit im dunklen Tunnel sehr viel Spaß gemacht, die gemeinsamen Ausflüge und Wanderungen noch mehr!

Michael Altmann danke ich für die Unterstützung bei der Verwaltung der diversen E15-Rechnersysteme, das geduldige Beantworten zahlreicher VMS-Fragen und die zuverlässige Entsorgung (alle Jahre wieder) meiner uralten Schokoladenostereier.

Danke an unsere Sekretärinnen Beatrice van Bellen und Alexandra Füldner, die das Institut E15 und den SFB 375 bestens im Griff haben. Ohne ihre Hilfe wäre ich über so manchem Formular verzweifelt.

Bei den Mitgliedern der Münchner BOREXINO-Gruppe und allen übrigen Institutsangehörigen von E15 möchte ich mich für gelegentliche Hilfe, gemeinsame Freizeitaktivitäten und für die ungezwungene und freundschaftliche Arbeitsatmosphäre bedanken. Einen besonderen Dank an Godehard Angloher für sein Bemühen, die Tradition des Institutskaffeetrinkens aufrechtzuerhalten!

Herzlichen Dank an Ulrich Bauer für die Versorgung mit Eis, Getränken und Neuigkeiten aus dem E11-Kiosk, ohne die ich es abends oft nicht so lange in Garching ausgehalten hätte.

Meiner Familie und meinen Freunden danke ich für ihre Unterstützung, gelegentliche Aufmunterungen und wohltuenden Ausgleich. Besonders meinem Mann Gernot möchte ich für sein Verständnis danken, das er bei all meinen Aktivitäten, die oft mit langen Trennungen verbunden waren, gezeigt hat.